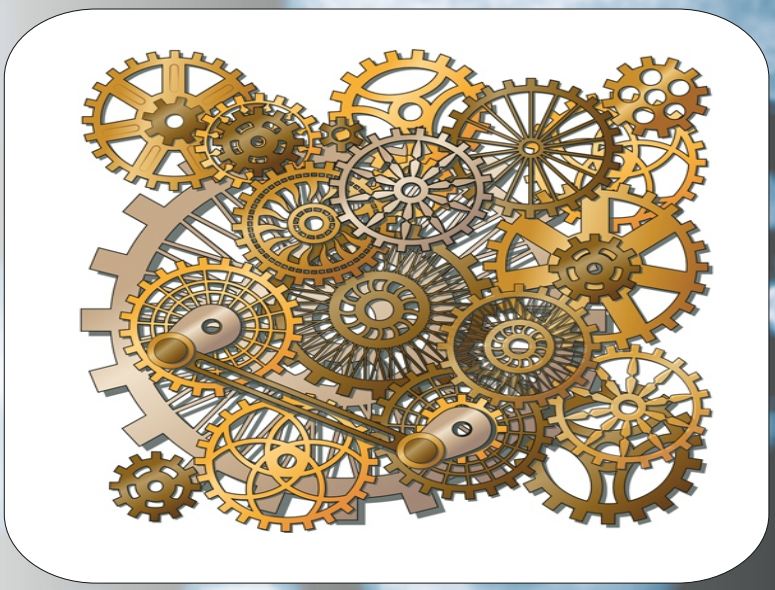
International journal
for science, technics and
innovations for the industry

MACHINES TECHNOLOGIES MATERIALS

ISSN PRINT 1313-0226
ISSN WEB 1314-507X
Issue 2 / 2017
YEAR XI



Published by
Scientific technical
Union of Mechanical Engineering "INDUSTRY 4.0"

MACHINES. TECHNOLOGIES. MATERIALS

INTERNATIONAL SCIENTIFIC JOURNAL

PUBLISHER

SCIENTIFIC TECHNICAL UNION OF MECHANICAL ENGINEERING "INDUSTRY 4.0"

108, Rakovski Str., 1000 Sofia, Bulgaria
tel. (+359 2) 987 72 90,
tel./fax (+359 2) 986 22 40,
office@stumejournals.com
www.stumejournals.com

ISSN PRINT 1313-0226, ISSN WEB 1314-507X, YEAR XI, ISSUE 2 / 2017

EDITOR-IN-CHIEF

Prof. D.Sc. DHC Georgi Popov,
President of Bulgarian Scientific and Technical Union of Mechanical Engineering

EDITORIAL BOARD

MEMBERS	SCIENTIFIC COMPETENCE
Prof. Dimitar Damyanov	Automatisation of production
Prof. Dimitar Karaivanov	Mechanics of machines
Prof. Dimitar Stavrev	Technologies and materials
Prof. Dimitar Yonchev	National and industrial security
Prof. Galina Nikolcheva	Machines tools and technologies
Prof. Hristo Shehtov	Automatisation of production
Prof. Idilija Bachkova	Automatisation of production
Prof. Ivan Kralov	Mechanics of machines
Prof. Ivan Parshorov	Technologies and materials
Prof. Ivan Yanchev	Machines and technologies
Prof. Ivo Malakov	Automatisation of production
Prof. Kiril Angelov	Industrial Management
Prof. Lilo Kunchev	Transport Equipment and Technology
Prof. Lubomir Dimitrov	Machines and technologies
Prof. Miho Mihov	Agricultural machinery
Prof. Miroslav Denchev	Ergonomics and design
Prof. Mladen Velev	Economics and Marketing
Prof. Nikolay Diulgerov	Technologies and materials
Prof. Ognyan Andreev	Production management
Prof. Petar Kolev	Transport Equipment and Technology
Prof. Roman Zahariev	Robotics
Prof. Sasho Guergov	Robotic systems and technology
Prof. Tsanka Dikova	Technologies and materials
Prof. Vitan Galabov	Mechanics of machines

MACHINES. TECHNOLOGIES. MATERIALS

INTERNATIONAL SCIENTIFIC JOURNAL

ISSN PRINT 1313-0226, ISSN WEB 1314-507X, YEAR XI, ISSUE 2 / 2017

EDITORIAL BOARD FOREIGN MEMBERS

Prof. Adel Mahmoud	IQ	Prof. Marian Tolnay	SK
Prof. Ahmet Ertas	TR	Prof. Mark Easton	AU
Prof. Andonaq Londo	AL	Prof. Mart Tamre	EE
Prof. Andrei Firsov	RU	Prof. Maryam Ehteshamzade	IR
Prof. Andrzej Golabczak	PL	Prof. Michael Evan Goodsite	DK
Prof. Anita Jansone	LV	Prof. Movlazade Vagif Zahid	AZ
Prof. Aude Billard	CH	Prof. Natasa Naprstkova	CZ
Prof. Bojan Dolšak	SI	Prof. Oana Dodun	RO
Prof. Christian Marxt	LI	Prof. Oleg Sharkov	RU
Prof. Dale Carnegie	NZ	Prof. Páll Jensson	IS
Prof. Ernest Nazarian	AM	Prof. Patrick Anderson	NL
Prof. Esam Husein	KW	Prof. Paul Heuschling	LU
Prof. Ewa Gunnarsson	SW	Prof. Pavel Kovac	RS
Prof. Filipe Samuel Silva	PT	Prof. Per Skjerpe	NO
Prof. Francisco Martinez Perez	CU	Prof. Péter Korondi	HU
Prof. Franz Haas	AT	Prof. Peter Kostal	SK
Prof. Genadii Bagliuk	UA	Prof. Juan Alberto Montano	MX
Prof. Georg Frey	DE	Prof. Raul Turmanidze	GE
Prof. Gregory Gurevich	IL	Prof. Renato Goulart	BR
Prof. Haydar Odinaev	TJ	Prof. Roumen Petrov	BE
Prof. Hiroyuki Moriyama	JP	Prof. Rubén Darío Vásquez Salazar	CO
Prof. Iryna Charniak	BY	Prof. Safet Isić	BA
Prof. Ivan Svarc	CZ	Prof. Sean Leen	IE
Prof. Ivica Veza	HR	Prof. ShI Xiaowei	CN
Prof. Jae-Young Kim	KR	Prof. Shoirdzan Karimov	UZ
Prof. Jerzy Jedzejewski	PL	Prof. Sreten Savićević	ME
Prof. Jean-Emmanuel Broquin	FR	Prof. Stefan Dimov	UK
Prof. Jordi Romeu Garbi	ES	Prof. Svetlana Gubenko	UA
Prof. Jukka Tuhkuri	FI	Prof. Sveto Cvetkovski	MK
Prof. Kazimieras Juzėnas	LT	Prof. Tamaz Megrelidze	GE
Prof. Krasimir Marchev	USA	Prof. Tashtanbay Sartov	KG
Prof. Krzysztof Rokosz	PL	Prof. Teimuraz Kochadze	GE
Prof. Leon Kukielka	PL	Prof. Thorsten Schmidt	DE
Prof. Mahmoud El Gammal	EG	Prof. Tonci Mikac	HR
Prof. Manolakos Dimitrios	GR	Prof. Vasile Cartofeanu	MD
Prof. Marat Ibatov	KZ	Prof. Yasar Pancar	TR
Prof. Marco Bocciolone	IT	Prof. Yurij Kuznetsov	UA
		Prof. Wei Hua Ho	ZA

C O N T E N T S

MACHINES

ESTIMATION OF ULTIMATE LOADS FOR CLIP CONNECTION WITH PARTIAL SWEEP OF SHAFT
Ass. Prof. PhD Ropyak L., Prof. DSc Shatskyi I., Ass. Prof. PhD Velychkovych A. 39

INVESTIGATION OF HEAT PIPE'S PERFORMANCE PARAMETERS DEPENDING ON DIFFERENT CONDITIONS
Radovan Nosek, Jan Siazik, Michal Holubcik, Jozef Jandacka 43

VIRTUAL MODELING AND SIMULATION OF A CYLINDER BUNDLE VERTICAL AND ROTATIONAL DROP
Ass. Prof. Aleksandar Kostikj PhD, Prof. Milan Kjosevski PhD. 46

TECHNOLOGIES

THE RESEARCH OF NEW TECHNOLOGY OF PLATE ROLLING BY MEANS OF COMPUTER SIMULATION
Prof., d.t.s. Naizabekov A. B., c.t.s. Lezhnev S. N., PhD student Panin E. A., master student Krupenkin I.I. 51

MECHANICAL PROPERTIES AND EDDY CURRENTS IN 20CrMo5 LOW –TEMPERATURE TEMPERING OF VARIOUS DURATIONS
Ivanov J.St., MSc 53

BIOLEACHING OF COPPER SLAGS BY MEANS OF DIFFERENT MICROBIAL CULTURES"
Irena Spasova, Stoyan Groudev, Plamen Georgiev, Marina Nicolova, Albena Lazarova 57

COMPARISON OF NUMERICAL AND EXPERIMENTAL RESULTS OF STRESS-DEFORMATION STATE IN A PIPELINE BRANCH
Prof. dr Bajić D. PhD1, M.Sc. Ćulafić S. 59

ANALYTIC MODEL OF NON AXISSYMMETRIC DRAWING
Doctor of science engineering, professor Nazaryan E.A., PhD physics and mathematics science, assistant professor Arakelyan M.M, PhD student Simonyan A.S. 63

KINETIC DIAGRAMS OF FATIGUE DAMAGE IN FRACTURE MESOMECHANICS
MSc.Eng.GeorgyDobrev,Ass.Prof,PhD.AlexanderPopov 66

URBAN TRANSPORT PLANNING AS A SUPPORT TO AIR POLLUTION CONTROL
assistant professor dr. Angelevska B., full professor dr. Atanasova V. 70

MATERALS

SiC(p) REINFORCED ALUMINUM MATRIX COMPOSITES OBTAINED BY HOT PRESSING AND THEIR MECHANICAL PROPERTIES
Aynur Kazaz, H. Erdem Çamurlu, M. Ayşe Dere, K. Egemen Kuyucu 74

THE USE OF STRUCTURAL ENGINEERING FOR OBTAINING SUPERHARD COATINGS BASED OF NITRIDES TRANSITION METALS
Assoc. Prof. D. Sc. Bochulia T.V., Prof. D. Sc. Sobol O.V. 77

RECEIVING ELECTROLYTIC NICKEL-CONTAINING POWDERS OF THE PREDICTED STRUCTURE AT ANODE DISSOLUTION OF SECONDARY HEAT RESISTING ALLOYS
Baikonurov E.G., MS, doctoral candidate of PhD, Chernyshova O.V., Candidate of Technical Sciences, Ussoltseva G.A., Candidate of Technical Sciences 84

TRIBOLOGICAL STUDY OF COPPER ALLOY-BASED COMPOSITES REINFORCED WITH WC-W POWDERS PREPARED BY THE SPONTANEOUS INFILTRATION PROCESS OF THE LOOSE POWDER.
Daoud I1. Prof. Miroud D. Ph. D. Yamanoglu R. 87

WEAR RESISTANT COATINGS ON BASED BORIDE PHASES FORMED IN THE MAGNETIC FIELD ON ALLOYS
Prof. Dr. Chernega S., Poliakov I., Krasovsky M. 91

ESTIMATION OF ULTIMATE LOADS FOR CLIP CONNECTION WITH PARTIAL SWEEP OF SHAFT

Ass. Prof. PhD Ropyak L.[1], Prof. DSc Shatskyi I.[2], Ass. Prof. PhD Velychkovych A.[1]
Ivano-Frankivsk National Technical University of Oil and Gas[1], Ukraine,
Ivano-Frankivsk branch of Pidstryhach Institute for Applied Problems of Mechanics and Mathematics, NAS of Ukraine[2], Ukraine
E-mail: l_ropjak@ukr.net, ipshatsky@gmail.com, velja2@mail.ru

Abstract: *The paper describes promising structures of clip (friction-screw) connections with incomplete sweep of shaft used in the axial fans of pressurization of gas pumping units. The contact problems of interaction between semi-hubs and shaft for the generally asymmetric relatively the joint bolt connections are formulated. Two types of interaction are investigated: with and without lateral displacement. Based on a priori assumption about the distribution laws of contact pressure accepted in traditional courses of "Machine Details" an engineering method for calculating of clip connections is developed. Herewith different types of details coupling (with a gap, matched, with tightness) correspond to concentrated, cosine and sustainable (linear) distributions of contact stresses. There are determined an analytical dependences of limited moments and breakloose forces on spanning angles, bolt tightening force and tribological properties of joined parts of subassembly. The examples of comparative calculation for the variants of clip connection have been presented.*

Keywords: CLIP CONNECTION, PARTIAL SWEEP OF SHAFT, CALCULATION

1. Introduction

Clip (screw and friction) connections belong to the class of nominally fixed friction joints, in which required normal pressure is created by tightening bolts. There are designs with split and one-piece hub. Traditionally units with complete sweep of shaft are commonly used. But sometimes in structural considerations applicable are coupling in which semi-clips cling the part of cylindrical surface of shaft. Such a situation arises from the need to regulate the angle of parts fixing. An example of such a unit is combination of blades with hub in the axial fans of pressurization of gas pumping units. In Fig. 1 typical construction of such a pinch is shown. Necessity in regulation of fan blades impinging angle depending on season temperature in room has resulted to using of split joints and become key motivation for our research.

The methods of typical calculations of most commonly used clip connections with complete sweep of shaft are worked out in details today [1…4]. Instead, the quality issues of gathering of clip connections with partial sweep of shaft are in fact unexplored. Especially it concerns the units, that are asymmetric relatively the joint bolt.

In the article the theoretical aspects of modeling the interaction of elements of detachable clip connections with incomplete sweep of shaft are considered. Aim of the research is to develop methods of engineering evaluation of bearing capacity of structures for different types of details coupling. The declared simplicity of calculations is that they are held not on the basis of rigorous solutions of contact problems, but on the basis of intuitive a priori assumptions about the contact pressure distribution law as it is done in traditional courses of "Machine Details" while calculation the detachable clips with complete sweep of shaft. Here we also develop and specify some results [5].

2. Formulation of problem

We consider split clip connections (Fig. 2). They consist of semi-hubs sweeping the shaft with diameter $D = 2R$ in areas with angles of inclination 2β and $\alpha + \beta$ respectively in symmetric and asymmetric versions. Suppose angles α and β are acute, so every single arc of contact is no longer than semicircle: $0 \le 2\beta \le \pi$, $0 \le \alpha + \beta \le \pi$. Connection is tightened with through-bolt so that the main vector of bolt tightening forces is P and passes through the axis of the shaft. Let's find the dependency of friction torque form tightening force.

Symmetric and asymmetric connections including the different character of parts coupling (with a gap, adjusted and with tightness) let's consider separately. Let's start with the simplest situations.

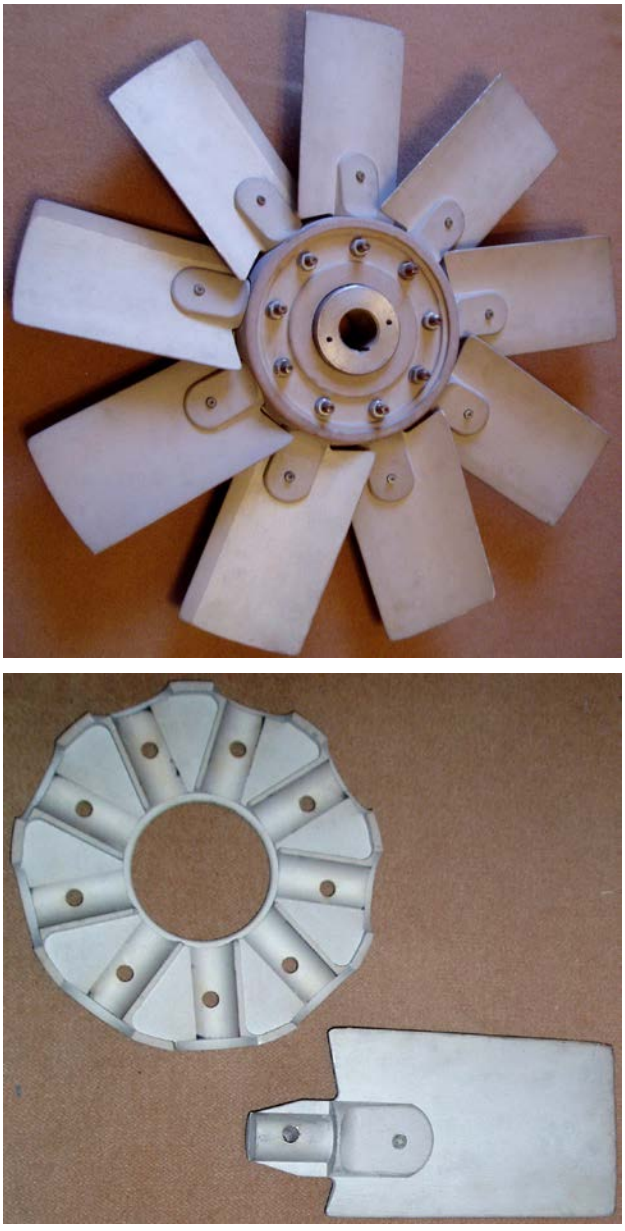


Fig. 1 *The design of the axial fans of pressurization: built-up (at the top) and laid-up (at the foot)*

3. Calculation of symmetric connection

Running polar angle ϑ is measured from the vertical axis of symmetry clockwise (Fig. 2, *a*). So for the upper semi-hub the dense clinging of shaft is possible on area $\vartheta \in (-\beta, \beta)$.

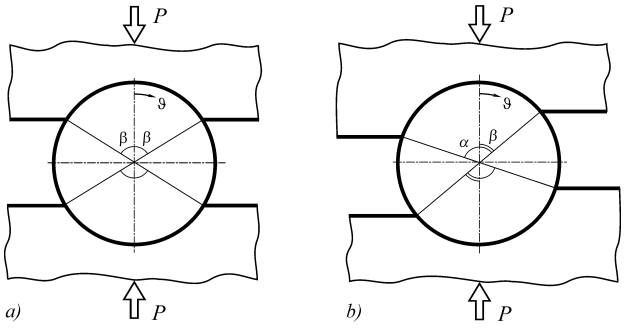


Fig. 1 *Scheme of clip connection with split hub that partially sweep the shaft: symmetric (a) and asymmetric (b) versions*

Let $q(\vartheta)$ is contact pressure that in this case is π-periodic even function. The main vector of contact stresses applied to, for example, upper semi-hub has to be balanced by tightening force is

$$\sum Y_i = R\int_{-\beta}^{\beta} q(\vartheta)\cos\vartheta\, d\vartheta - P = 0 .$$

Hence

$$P = 2R\int_{0}^{\beta} q(\vartheta)\cos\vartheta\, d\vartheta . \tag{1}$$

Let's find the moment of friction forces M acting on the shaft while attempting to turn it at two semi-hubs:

$$M = 2R\int_{-\beta}^{\beta} fq(\vartheta)Rd\vartheta = fD\cdot 2R\int_{0}^{\beta} q(\vartheta)d\vartheta , \tag{2}$$

f is dry friction coefficient.

Comparing (1) and (2), we find

$$M = fPD\frac{\int_{0}^{\beta} q(\vartheta)\,d\vartheta}{\int_{0}^{\beta} q(\vartheta)\cos\vartheta\, d\vartheta} . \tag{3}$$

Postulating in (3) contact pressure distribution laws for a particular character of coupling, we obtain the dependences of moment from the force P and the angle β.

When planting clip with large clearance ($R_{cl} > R$), when contact of semi-hub with the shaft passes through the generating line $\vartheta = 0$ and after tightening of bolts – a narrow strip, the contact pressure was approximated by concentrated force per unit length

$$q(\vartheta) = p\delta(\vartheta)/R ,$$

where $\delta(\vartheta)$ is Dirac function, $p = P/L$, L is strip contact length (deep into Fig. 2).

Then the numerator and denominator in (3) are the same constants, and

$$M = fPD . \tag{4}$$

When adjusted (agreed) planting in conditions of equality of radii of the shaft circles and semi-hub the contact pressure distribution is taken close to the cosine: $q(\vartheta) = q_{\max}\cos\vartheta$, $\vartheta \in (-\beta, \beta)$. By calculating the integrals in (3)

$$M = fPD\frac{4\sin\beta}{2\beta + \sin 2\beta} . \tag{5}$$

The presence of tightness ($R_{cl} < R$) in untensioned condition in fact means the presence of gap at small ϑ and the point of contact at $\vartheta \approx \pm\beta$. When tightening the bolt the contact pressure localizes at the edges around of angles: $\vartheta = \pm\beta$, but after tightening mentioned gap is eliminated and further growth of P leads probably to equalization of contact pressure. So in this case let be $q(\vartheta) = q = const$ and after calculating integrals in (3)

$$M = fPD\frac{\beta}{\sin\beta} . \tag{6}$$

4. Calculation of asymmetric connection

Let $\vartheta \in (-\alpha, \beta)$ be the arc of probable contact and $q(\vartheta)$ be the contact pressure that in this case is π -periodic function (Fig. 2, *b*).

Calculating the vertical component of vector of contact stresses and the main moment of friction forces instead of (1) and (2) we obtain respectively

$$P = R\int_{-\alpha}^{\beta} q(\vartheta)\cos\vartheta d\vartheta , \tag{7}$$

$$M = fDR\int_{-\alpha}^{\beta} q(\vartheta)\, d\vartheta . \tag{8}$$

From (7) and (8) it is easy to find out the dependence between the friction torque and the total strength of bolt tightening

$$M = fPD\frac{\int_{-\alpha}^{\beta} q(\vartheta)\,d\vartheta}{\int_{-\alpha}^{\beta} q(\vartheta)\cos\vartheta\, d\vartheta} . \tag{9}$$

The feature of asymmetric connection is that depending on the way the semi-hubs are mounted by bolt there are two possible situations: 1) fixed connection without mutual horizontal displacement of semi-hubs; 2) free connection with the possibility of mutual lateral displacement of parts.

In first case the relative horizontal displacement equals zero and horizontal component of the contact stresses vector is unknown. And vice versa in second case the relative horizontal displacement is unknown and the projection of the main contact stresses vector on horizontal axis is zeroed:

$$\sum X_i = R\int_{-\alpha}^{\beta} q(\vartheta)\sin\vartheta\, d\vartheta = 0 . \tag{10}$$

The last condition is used to establish the degree of asymmetry of contact pressure distribution.

Depending on the character of semi-hub coupling with the shaft let's obtain the different expressions for the friction torque in asymmetric clip connection.

When planting the clip with a gap regardless of presence or absence of lateral displacement the contact pressure is concentrated in $\vartheta = 0$. Then from (9) also can be obtained (4).

In case of agreed contact for the task without lateral displacement we postulate the law: $q(\vartheta) = q_{\max}\cos\vartheta$. Calculating integrals in (9)

$$M = fPD\frac{4(\sin\alpha + \sin\beta)}{2(\alpha + \beta) + \sin 2\alpha + \sin 2\beta} . \tag{11}$$

In case of presence of lateral displacement we accept cosine distribution of contact pressure with displaced maximum

$$q(\theta) = q_{\max}\cos(\vartheta - \vartheta_0) , \tag{12}$$

where the angle ϑ_0 can be calculated from (10).

Calculating quadratures in (9) and (10) after simple transformations

$$M = fPD \cdot 4 \frac{(\sin\alpha + \sin\beta)\cos\vartheta_0 - (\cos\beta - \cos\alpha)\sin\vartheta_0}{(2(\alpha+\beta) + \sin 2\alpha + \sin 2\beta)\cos\vartheta_0 - (\cos 2\beta - \cos 2\alpha)\sin\vartheta_0},$$

$$\operatorname{tg}\vartheta_0 = \frac{\cos 2\beta - \cos 2\alpha}{2(\alpha+\beta) - \sin 2\alpha - \sin 2\beta}.$$

It is easy to ensure that $\vartheta_0 > 0$ if $\alpha > \beta$.

Excluding ϑ_0 finally we get

$$(13)\quad M = fPD \frac{2(\sin\alpha + \sin\beta) - (\alpha + \beta - \sin(\alpha+\beta))}{(\alpha+\beta)^2 - (\alpha+\beta)(\sin 2\alpha + \sin 2\beta) - \sin^2(\alpha+\beta)}.$$

In order to guarantee the correctness of obtained result the inequality performing should be provided in (12)

$$q(\vartheta) \ge 0, \quad \vartheta \in (-\alpha, \beta).$$

This inequality is performed if $\cos(-\alpha - \vartheta_0) \ge 0$. Hence

$$\alpha \ge \frac{\pi}{2} - \vartheta_0,$$

or

$$(14)\qquad \operatorname{tg}\alpha \ge \operatorname{ctg}\vartheta_0 = \frac{2(\alpha+\beta) - \sin 2\alpha - \sin 2\beta}{\cos 2\beta - \cos 2\alpha}$$

are the conditions under which it is possible to use of formula (13) when $\alpha > \beta$. In other words β does not have to be less than α, then the area of contact covers the entire range $(-\alpha, \beta)$. In violated inequality (14) in some areas $(-\alpha, -\alpha_1)$ the contact is broken, then instead α in (13) it should be taken $\alpha = \alpha_1(\beta)$, where α_1 is the root of the transcendental equation

$$\operatorname{tg}\alpha_1 = \frac{2(\alpha_1+\beta) - \sin 2\alpha_1 - \sin 2\beta}{\cos 2\beta - \cos 2\alpha_1}.$$

Let's finally consider the asymmetrical coupling with tightness. In the absence of lateral displacements we accept: $q(\vartheta) = const$, $\vartheta \in (-\alpha, \beta)$. Then from (9)

$$(15)\qquad M = fPD \frac{\alpha+\beta}{\sin\alpha + \sin\beta}.$$

To connect with an additional degree of freedom in the horizontal direction let's assume that the contact pressure is distributed linearly

$$(16)\qquad q(\vartheta) = A + B\vartheta, \quad \vartheta \in (-\alpha, \beta).$$

Then

$$M = fPD \frac{A(\alpha+\beta) + B(\beta^2 - \alpha^2)/2}{A(\sin\alpha + \sin\beta) - B(\alpha\sin\alpha + \cos\beta)},$$

where from (10)

$$\frac{A}{B} = \frac{\sin\alpha + \sin\beta - \alpha\cos\alpha - \beta\cos\beta}{\cos\beta - \cos\alpha} > 0.$$

Excluding the value A/B finally we get

$$(17)\quad M = fPD \frac{\alpha+\beta}{2} \frac{2(\sin\alpha + \sin\beta) - (\alpha+\beta)(\cos\alpha + \cos\beta)}{2 - 2\cos(\alpha+\beta) - (\alpha+\beta)\sin(\alpha+\beta)}.$$

Checking in (16) inequality $q > 0$ we find the condition of result (17) applicability

$$A - B\alpha \ge 0,$$

$$(18)\qquad \alpha \le \frac{\sin\alpha + \sin\beta - \alpha\cos\alpha - \beta\cos\beta}{\cos\beta - \cos\alpha}.$$

If α is too high and (18) is violated, then again in (17) it should be taken $\alpha = \alpha_1(\beta)$ where α_1 is the root of the transcendental equation that depends from β

$$\alpha_1 \le \frac{\sin\alpha_1 + \sin\beta - \alpha\cos\alpha_1 - \beta\cos\beta}{\cos\beta - \cos\alpha_1}.$$

In this case the contact happens only on the area: $\vartheta \in (-\alpha_1, \beta)$.

5. Analysis of results

The final formulas for the calculation of limit values of moments that can be transmitted by connections with incomplete sweep of shaft are consolidated in Table.

The ultimate loads for the symmetric clip connection calculated using formulae (4)–(6) are given in the Fig. 3. The similar results for asymmetric connection without lateral displacement of semi-hubs obtained using formulae (4), (11) and (15) are exhibited in the Fig. 4–6.

In the case of mutual displacement of components additionally by axial force Q (perpendicular to the plane of Fig. 2) in the last column of the table and on the diagrams M should be replaced by $\sqrt{M^2 + (QR)^2}$.

Table 1: *Summary table*

Type of connection	Character of coupling	Contact pressure distribution	Friction torque
Symmetric	with a gap	concentrated force	$M = fPD$
	adjusted	cosine	$M = fPD\frac{4\sin\beta}{2\beta + \sin 2\beta}$
	with tightness	uniform	$M = fPD\frac{\beta}{\sin\beta}$
Asymmetric without lateral displacement of semi-hubs	with a gap	concentrated force	$M = fPD$
	adjusted	cosine	$M = fPD\frac{4(\sin\alpha + \sin\beta)}{2(\alpha+\beta) + \sin 2\alpha + \sin 2\beta}$
	with tightness	uniform	$M = fPD\frac{\alpha+\beta}{\sin\alpha + \sin\beta}$
Asymmetric with lateral displacement of semi-hubs	with a gap	concentrated force	$M = fPD$
	adjusted	cosine with displaced maximum	$M = fPD\frac{2(\sin\alpha + \sin\beta) - (\alpha+\beta-\sin(\alpha+\beta))}{(\alpha+\beta)^2 - (\alpha+\beta)(\sin 2\alpha + \sin 2\beta) - \sin^2(\alpha+\beta)}$
	with tightness	linear	$M = fPD\frac{\alpha+\beta}{2}\frac{2(\sin\alpha + \sin\beta) - (\alpha+\beta)(\cos\alpha + \cos\beta)}{2 - 2\cos(\alpha+\beta) - (\alpha+\beta)\sin(\alpha+\beta)}$

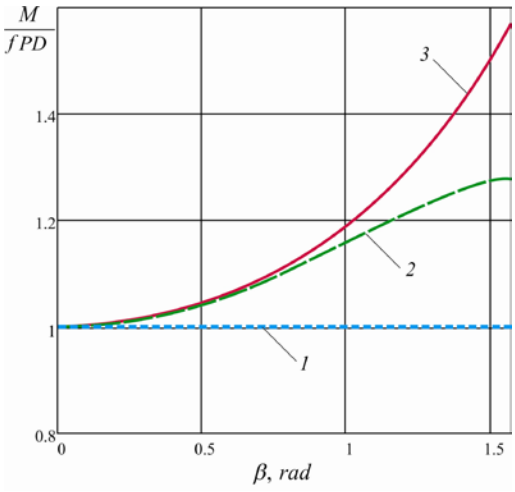


Fig. 3 *The ultimate loads for the symmetric clip connection: lines 1, 2 and 3 correspond to couplings with a gap, matched and with tightness respectively*

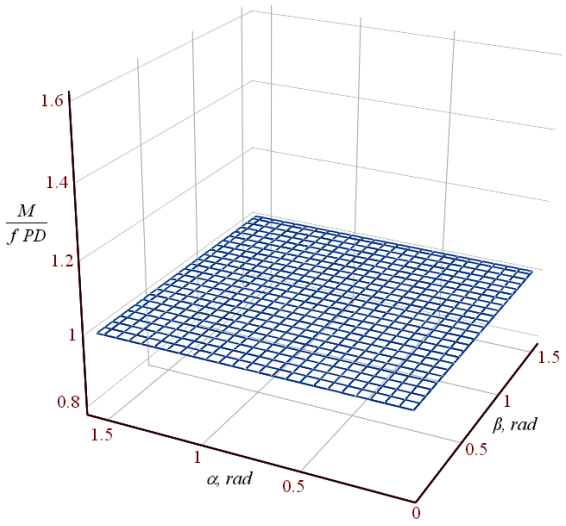


Fig 4 *The ultimate load for asymmetric clip connection without lateral displacement of semi-hub and with a gap coupling*

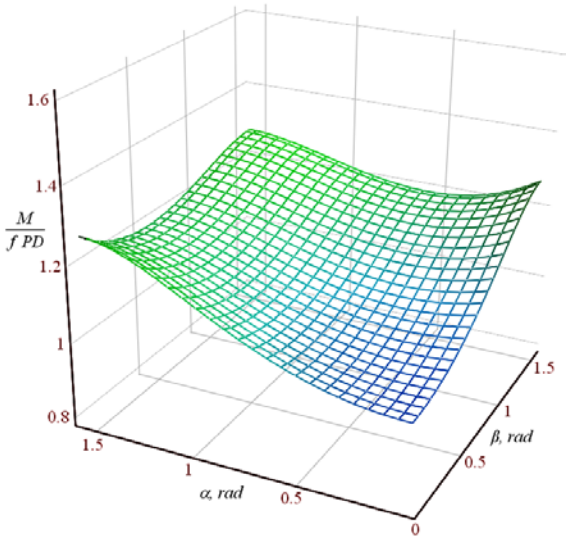


Fig 5 *The ultimate load for asymmetric clip connection without lateral displacement of semi-hub and with matched coupling*

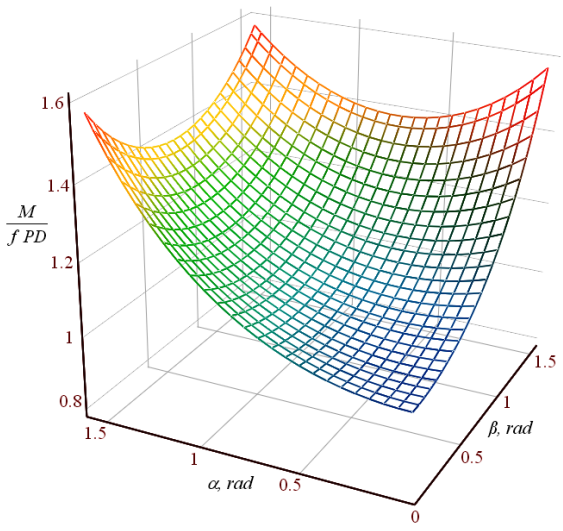


Fig 6 *The ultimate load for asymmetric clip connection without lateral displacement of semi-hub and with tightness coupling*

6. Conclusions

On the basis of a priori assumptions about the distribution of contact stresses analytical dependences of ultimate moment and breakloose forces in detachable clip connection on spanning angles, bolt tightening force and tribological properties of details surfaces are determined.

The coupling with tightness and with big angle of sweep of shaft has proved to be the most effective. Some asymmetry in the contact increases the ultimate load too.

The degree of adequacy of the results is advisable to find out using numerical analysis of contact problems of elasticity theory.

7. References

1. Blake A. Design of mechanical joints. – New York: M. Dekker, 1985. – 553 p.

2. Korovin Yu. V., Shamsutdinov I. R. Connections shaft-hub. Calculations and projecting. – Moscow: Mashynostroienie, 2000. – 55 p. (in Russian).

3. Springer Handbook of Mechanical Engineering / ed. by K.-H. Grote, E. K. Antonsson. – New York: Springer Science-+Business Media, 2009. – 1580 p.

4. Contact problems between the hub and the shaft with a three-angular shape of cross-section for different angular positions / M. Dudziak, G. Domek, A. Kołodziej, K. Talaśka // Procedia Engineering. – 2014. – Vol. 96. – Pp. 50–58.

5. Shatsky I. P., Ropyak L. Ya. Elementary calculation of clip connections with incomplete sweep of shaft // Odes'kyi Politechnichnyi Universytet. Pratsi. – 2015. – Issue 2(46). – Pp. 51–56.

INVESTIGATION OF HEAT PIPE'S PERFORMANCE PARAMETERS DEPENDING ON DIFFERENT CONDITIONS

Radovan Nosek[1], Jan Siazik[1], Michal Holubcik[1],
Jozef Jandacka[1]
Department of Power Engineering, Faculty of Mechanical Engineering, University of Zilina[1]

radovan.nosek@fstroj.uniza.sk

Abstract: *The article deals with effect of the nano-fluids on the performance parameters of heat pipes. Stainless steel heat pipe was filled with a nano-fluid, a solution of copper sulphate and ferric chloride, up to 20% of the total volume of the heat pipe. Solutions of the nano-fluids were produced in the following concentrations: 1%, 2%, 3%, 4% and 5%. The performance parameters were measured on the experimental setup. The experimental measurements were carried out for different operating temperature and measured results show that the concentration of working fluid has effect on performance of the heat pipe..*

Keywords: NANO-FLUID, COPPER SULPHATE, FERRIC CHLORIDE, PERFORMANCE PARAMETERS

1. Introduction

Rising energy costs and tightening the standards for reducing CO_2 emissions requires more particularly in areas of high energy efficient solutions. Effective option is energy recovery of waste heat [1]. Waste heat is produced by various technological processes in industrial and energy production. To recover waste heat is necessary to choose the right type of technology, which mainly depends on the type of uses and applications of such a device. For efficient use of waste heat are also used heat pipes [2]. Heat pipes are used for efficient transfer of heat while maintaining low temperature differences. Therefore, the development and optimization of the key to greater efficiency and broader application of heat pipes. The advantage of the heat pipe is that even with small dimensions can transfer high thermal performance while its construction is simple with a long life, reliability and durability [3]. Different types and quantities of substances affect labor transfer characteristics of the heat pipe. It is therefore important that a well working medium and the type of material used, in view of the used application. In this so that we can re-use the waste heat, are usually used heat exchangers of gravity or capillary heat pipes [4].

2. Theoretical analysis of gravitational heat pipes

The heat pipe is a device that is widely used as a heat exchanger. It has several advantages such as simple structure, long life, high efficiency and easy maintenance. Its performance parameters affect various factors, but in particular the working fluid, amount of the workload and filling process. The heat pipe comprises a closed outer shell and a working fluid provided within the pipe. The pipe operates in a vertical or slightly sloping position of each coupling portion located above the evaporation portion. In the vapour of the working fluid evaporates and condenses the condensation part. [4] The condensate then flows into the evaporator section by the action of gravity along the smooth inner wall. (Fig.1)

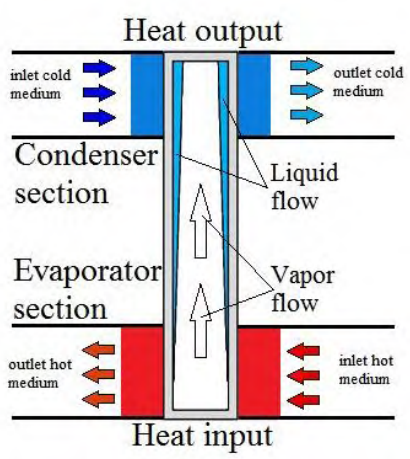


Fig. 1 Function of gravitation heat pipe

The transferred heat flow depends on the thermal resistance of the liquid film on the wall of the condensation part. Correct operation of the tube is conditioned in such a dosing quantity of working fluid, in the range of operating parameters to avoid insufficient wetting of the surface evaporation and thus decreased performance [5]. Conversely, too much excess liquid in the vapour of boiling over leads to the release of large steam bubbles when surging phenomena. Heat transfer between the vapour phase of the working fluid and the inner wall of the tube is mainly influenced by the character of the flow of the falling film of liquid.

3. Production gravitational heat pipes

The heat pipe was made of several parts. All the parts were made of stainless material. Casing pipe forms a hollow round bar stainless steel AISI 304, cut to a length of 500 mm with an inner diameter of 10 mm and a wall thickness of 1 mm (Fig 2). The bottom of the pipes (plugs) were turned off round bar of stainless material (304) to the required size (Fig. 2). Into the centre of the end caps were drilled holes with a diameter of 1.4 mm, where was subsequently placed a needle designed for filling process. All these parts were bonded by soldering (Fig. 2). By this process was made stainless gravitational heat pipe before filling the working substance.



Fig. 2 Stainless steel pipe, cap, closed end of the tube (respectively from left to right side)

In this research are presented experiments with heat pipe filled by the working substance to 20%. The amount of working fluid was determined based on previous research. These results shows, that optimal amount of working medium is 20-25% of the total heat pipe volume.

The heat pipes were weighed before and after filling the working substance at 22% of its capacity. The evaporation of the working medium was carried out by fast heating of the jacket pipe. The evaporation of the working fluid took place up to 20% filling, the filling needle was then closed with metal tongs and end of the needle has entered into a joint using a silver solder and flame.

Working medium – nano-fluid

As a working medium were chosen following nano-fluids: solution of distilled water with ferric chloride and solution of distilled water with cooper sulphate. These solutions should provide higher heat transfer of the heat pipe in comparison with distilled water.

In order to determine the optimum performance, the solutions were prepared in concentrations from 1% to 5%. Ferric chloride ($FeCl_3$) is a yellow-brown but the transmitted light as a purple red hygroscopic inorganic compound (darkness of the colour depends on the degree of oxidation by oxygen), which is under the action of atmospheric moisture flow able self. Copper sulphate ($CuSO_4$) is is an inorganic compound that combines sulfur with copper (anhydride), which turns blue water intake.



Fig. 3 Five percent solution of $FeCl_3$ (left) and $CuSO_4$ (right)

4. Experimental setup

The measurement was carried out on an experimental setup (Fig. 4), where the gravitational heat pipe was placed. Evaporating part of the heat pipe was heated with water in the range from 40 °C to 90 °C and the condensation part was cooled with water at 20 °C. In total were done six measurements and the temperature difference between the tests was 10°C.

For a correct analysis of the performance parameters of the heat pipe was needed precisely defined following values:

- Water temperature at the inlet and outlet of cooling (°C)

- Flow rate of the refrigerant circuit (l/ min).

In order decrease heat loses, the evaporation part of the pipe was insulated with glass wool into the environment. The measured values were recorded at 5 second intervals for one hour by means of sensors. Data from the sensors were transmitted through the measuring panel to the software AMR WinControl from AHLBORN installed in the notebook. The measured values were out of the program AMR WinControl from AHLBORN exported to Microsoft Excel, where the values were then processed and analyzed. The actual determination of the performance of the heat pipe is based on the difference of input and output temperatures of the cooling water passing through the cooling device positioned on the condensing section of the heat pipe.

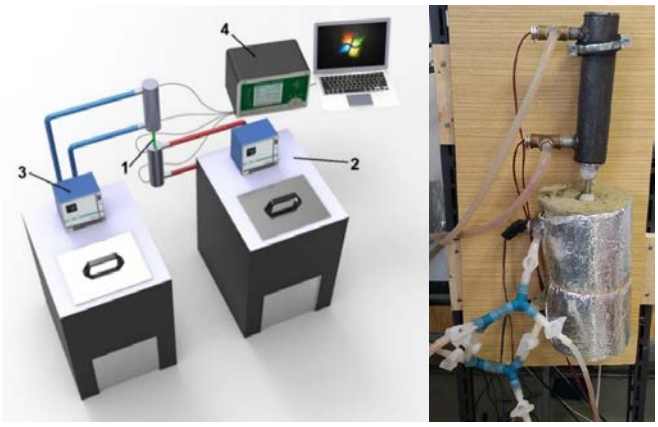


Fig. 4 The scheme of experimental setup (1-Heat pipe, 2-Heating circulators, 3- Refrigerated circulator, 4-Data logger)

5. Results and discussion

Inlet temperature in the heated part of the heat pipe device greatly impacts the performance. The value of power was growing with increasing value of the operating temperature. The performance data of individual samples heat pipes were highest at a temperature gradient 90/20 °C. In general, the tested heat pipes began to work effectively in different temperature. This is due to the pressure difference inside the pipes.

The results in Tab. 1 and 2 show that using $FeCl_3$ and $CuSO_4$ nano-fluids reaching peak output of pipe with a 1% concentration. Its output grew approximately linearly with increasing temperature. The heat pipes work effectively at lower temperatures. In the case of samples with other concentrations, the heat pipes started to work effectively between 70 and 80 ° C. The lowest performance was measured for 3% concentration of the nano-fluid. This could be due not only to different strengths, but also a way of filling and sealing of heat pipe in which may have been deflated respectively aspiration of air.

Table 1: *Power dependence on temperature and the concentration of the $FeCl_3$ nano-fluid*

$FeCl_3$	40°C	50°C	60°C	70°C	80°C	90°C
1%	46 W	59 W	180 W	250 W	326 W	382 W
2%	14 W	41 W	148 W	213 W	285 W	359 W
3%	9 W	12 W	42 W	96 W	187 W	240 W
4%	20 W	95 W	147 W	198 W	260 W	315 W
5%	25 W	94 W	155 W	221 W	288 W	351 W

Table 2: *Power dependence on temperature and the concentration of the $CuSO_4$ nano-fluid*

$CuSO_4$	40°C	50°C	60°C	70°C	80°C	90°C
1%	15 W	37 W	53 W	201 W	342 W	431 W
2%	5 W	1 W	10 W	39 W	164 W	246 W
3%	20 W	22 W	22 W	39 W	261 W	368 W
4%	14 W	34 W	125 W	255 W	313 W	376 W
5%	34 W	62 W	101 W	182 W	300 W	405 W

6. Conclusions

Currently, only a few publications present nano-fluids and this research topic has considerable potential. Nano-fluid seems to be as interesting alternative working substance that can easily and efficiently achieve performance increase heat pipe. The article deals with nano-fluids ferric chloride and cooper sulphate at concentrations of from 1% to 5% and describes the method for producing stainless steel gravitational heat pipes that have been made for this test. The achieved results show the increase of heat pipe performance by about 5% in comparison to other working fluid (water, ethanol). In order to observe more accurate results it is necessary to improve the filling process and insure uniform pressure and the same amount of working medium in all samples.

Acknowledgement

This article is supported by the financial assistance of the project KEGA No. 042ŽU-4/2016 ”Chladenie na základe fyzikálnych a chemických procesov”.

References

[1] REAY,D. A., KEW, P. A. Heatpipes, Theory, Design and Applications, FifthEdition,USA,2006

[2] NEMEC, P., ČAJA, A., MALCHO, M. Mathematical model for heat transfer limitations of heat pipe, Mathematical and computer modeling Volume: 57 Issue: 1-2 Pages: 126-136, 2013

[3] LENHARD, R., KADUCHOVÁ, K. and PAPUČÍK, Š., Analysis of the fill amount influence on the heat performance of heat pipe. IN: International Conference on Application of Experimental and Numerical Methods in Fluid Mechanics and Energetics 2014, XIX.AEaNMiFMaE 2014; Liptovsky Jan; Slovakia; 9 April 2014 through 11 April 2014; Code 107300, ISBN: 978-073541244-6, DOI: 10.1063/1.4892724

[4] VANTÚCH, M., HUŽVÁR, J. and KAPJOR, A., Heat transfer from oriented heat exchange areas [Prenos tepla z orientovaných teplovýmenných plôch] In: EPJ Web of Conference [elektronický zdroj]. - ISSN 2100-014X. - Vol. 67, art. no. 02122 (2014)

[5] FAGHRI, A. Heat Pipe Science and Technology. Washington DC. Taylor & Francis, 1995.

VIRTUAL MODELING AND SIMULATION OF A CYLINDER BUNDLE VERTICAL AND ROTATIONAL DROP

Ass. Prof. Aleksandar Kostikj PhD, Prof. Milan Kjosevski PhD
Faculty of Mechanical Engineering, Ss. Cyril and Methodius University in Skopje, Republic of Macedonia

aleksandar.kostikj@mf.edu.mk

Abstract: *A cylinder bundle is a portable assembly which consists of a frame and two or more cylinders, each of a capacity up to 150 l and with a combined capacity of not more than 3000 l, or 1000 l in the case of toxic gases, connected to a manifold by cylinder valves or fittings such that the cylinders are filled, transported and emptied without disassembly. The type approval of the cylinder bundle covers series of tests regarding its structure and its behavior during and after the tests. The research, presented in this paper, is focused on virtual testing, i.e. modeling and simulation of a cylinder bundle drop tests. First, a CAD model of a cylinder bundle which contains five cylinders is built, and then a vertical and rotational drop tests are simulated in virtual environment. The obtained results are analyzed in line with the demands defined in the international standard ISO 10961:2010(E).They could serve as a base for further improvement of the model and point out the possibility for validation of the virtual testing.*

Keywords: CYLINDER BUNDLE, VIRTUAL MODEL, VIRTUAL TESTING, DROP TESTS

1. Introduction

Cylinder bundles are portable assemblies which are widely used for transport and storage of gases on sites, where the gases are further used. According to the international standard ISO 10961:2010(E), a cylinder bundle is a portable assembly which consists of a frame and two or more cylinders, each of a capacity up to 150 l and with a combined capacity of not more than 3000 l, or 1000 l in the case of toxic gases, connected to a manifold by cylinder valves or fittings such that the cylinders are filled, transported and emptied without disassembly. The exploitation of a cylinder bundle is preconditioned with its type approval. The type approval itself covers series of tests regarding the structure of the cylinder bundle and its behavior during and after the tests. The most demanding tests are the vertical drop test and the rotational drop test as defined in the international standard ISO 10961:2010(E) [7]. These tests have the following pass criteria: the primary frame structure shall not fail such that subsequent movement by fork-lift truck or slinging is not possible; the cylinders and manifolds shall remain constrained in the frame, though deformation of components is acceptable; the bundle shall not leak.

The research, presented in this paper, is focused on virtual testing [1, 2, 4, 5, 7] regarding the above mentioned tests. They are conducted on a model of a cylinder bundle which was already produced. The bundle contained five Vitkovice cylinders 690/150, intended for carriage of high pressurized gas (over 200 bar). The produced cylinder bundle is presented on fig. 1.



Fig. 1 *Produced cylinder bundle*

The model of the bundle is built in a CAD software package [6]. It is a relevant representative of the real bundle. The virtual model is presented on fig. 2.



Fig. 2 *Virtual model of the cylinder bundle*

The remainder of the paper is organized as follows: The virtual modeling and simulation of the cylinder bundle vertical drop test are presented in section 2. Section 3 presents the virtual modeling and simulation of the cylinder bundle rotational drop test. Finally the conclusions are laid down in section 4.

2. Virtual modeling and simulation of the cylinder bundle vertical drop test

The procedure of the vertical drop test prescribes that the bundle is dropped at a height of 100mm on a concrete surface. Also, the initial inclination of the bundle towards the surface should be at last 5˚.

The initial setup of the virtual testing is in line with the requirements defined in point 7.2.2.3.4 of the international standard ISO 10961:2010(E) [7]. The model is set on a height of 100mm from concrete surface and the initial inclination of the bundle towards the surface is set on 10˚ (fig. 3.).

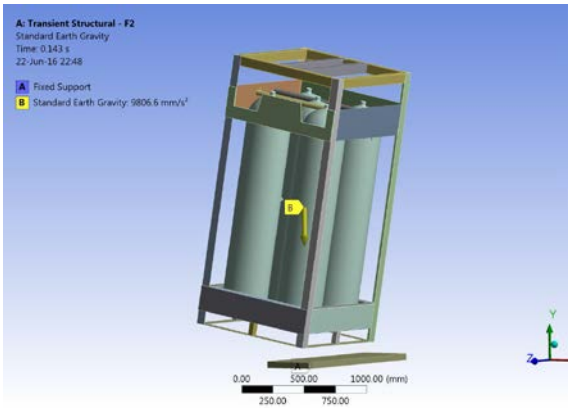


Fig. 3 *Initial setup of the vertical drop test simulation*

The virtual vertical drop test is conducted with two consecutive and connected simulations-analyses [3]. The first one is a transient structural analysis. It treats the free fall of the bundle till the impact with the concrete surface. The free fall lasts for 0.143s. The position of the bundle at different time moments is presented on fig. 4, fig. 5 and fig. 6. The second simulation is an explicit dynamics analysis. This simulation treats the impact of the bundle with the concrete surface and lasts for 30ms. The stress condition of the bundle is stable after this time period. The equivalent stresses which appear in the bundle at different time moments of the explicit dynamics analysis are presented on fig. 7, fig. 8 and fig. 9.

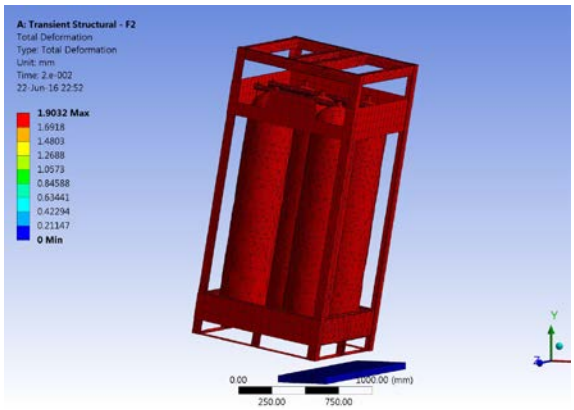


Fig. 4 *Position of the bundle at time t=0.02s*

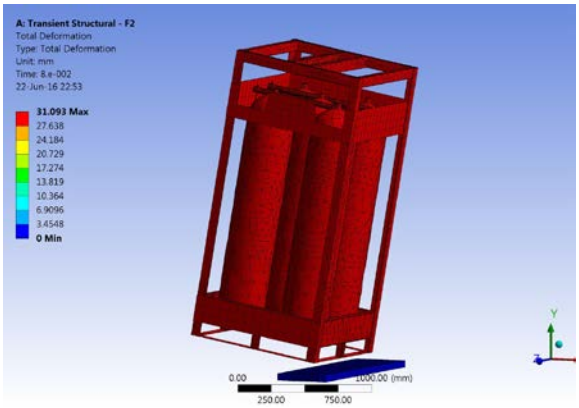


Fig. 5 *Position of the bundle at time t=0.08s*

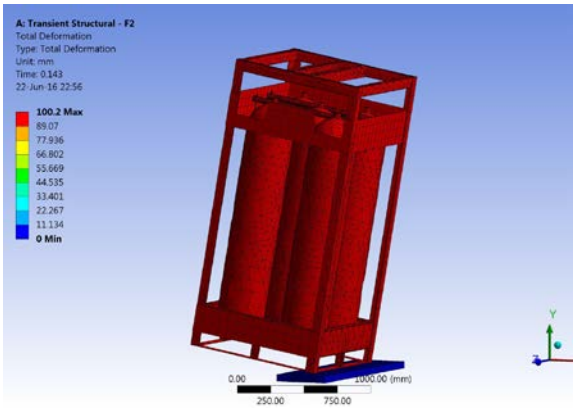


Fig. 6 *Position of the bundle at time t=0.143s*

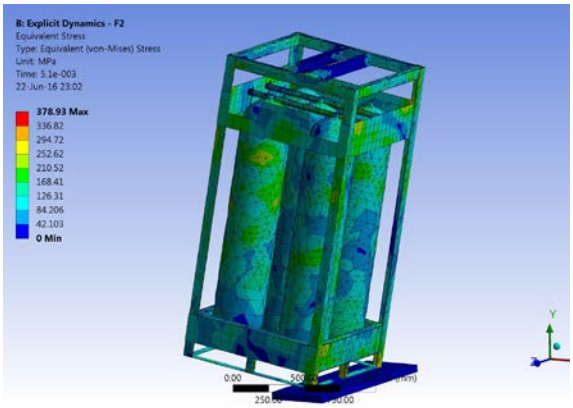


Fig. 7 *Equivalent stresses in the bundle at time t=0.0051s*

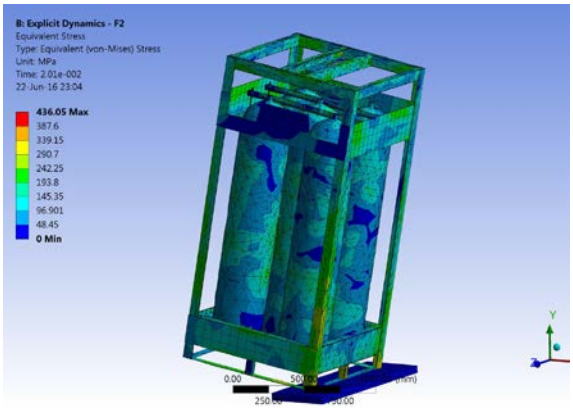


Fig. 8 *Equivalent stresses in the bundle at time t=0.0201s*

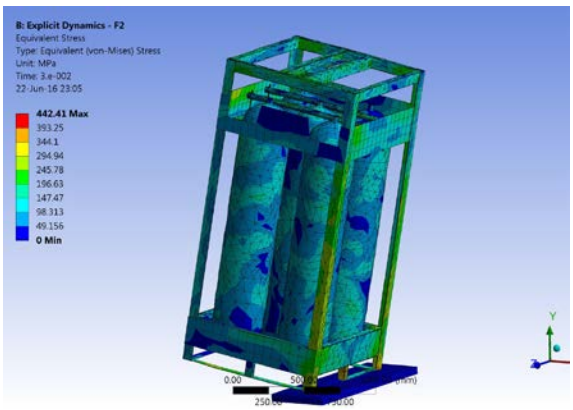


Fig. 9 *Equivalent stresses in the bundle at time t=0.0051s*

The explicit dynamics analysis shows that the stresses in the bundle, which appear during the impact, are below the ultimate stress of the material. The maximum stress appears in the vertical beams of the bundle, in the impact zone. Its range is about 440N/mm^2. The plastic deformations of the bundle during the impact are below 8.1% of the size of the model's final elements.

Based on the results of the performed combined analyses it can be concluded that the bundle satisfies the requirements as defined in point 7.2.2.3.4 of the international standard ISO 10961:2010(E)[7], regarding the vertical drop test.

3. Virtual modeling and simulation of the cylinder bundle rotational drop test

The procedure of the rotational drop test prescribes that the bundle falls from a platform on a concrete surface. The platform has a minimal height of 1200mm. During the fall, the bundle rotates about point 2 (fig. 10).

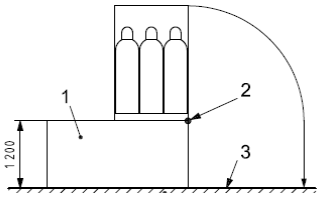


Fig. 10 *Rotation drop test – procedure (1 – platform, 2 – rotational point of the bundle, 3 – concrete surface)*

The initial setup of the model, regarding the rotational drop virtual testing, is in line with the requirements defined in point 7.2.2.3.4 of the international standard ISO 10961:2010(E)[7]. The model is set on a height of 1200mm from concrete surface and the initial inclination of the bundle towards the surface is set on 35˚ (fig. 11.). This inclination is defined according to the bundle's center of gravity and ensures rotational free fall of the bundle.

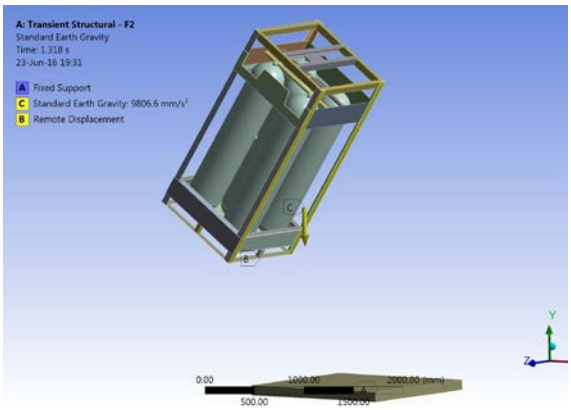


Fig. 11 *Initial setup of the rotational drop test simulation*

The rotational drop test alike the vertical drop test is conducted with two consecutive and connected simulations-analyses [3]. The first one is a transient structural analysis. It treats the rotational free fall of the bundle till the impact with the concrete surface. This free fall lasts for 1.318s. The position of the bundle at different time moments is presented on fig. 12, fig. 13 and fig. 14. The second simulation is an explicit dynamics analysis. This simulation treats the impact of the bundle with the concrete surface and lasts for 175ms. Within this time interval, the bundle has complete translational and rotational freedom. The time span of explicit dynamics analysis is sufficient to cover the dominant dynamics of the impact. The equivalent stresses which appear in the bundle at different time moments of the explicit dynamics analysis are presented on fig. 15, fig. 16 and fig. 17.

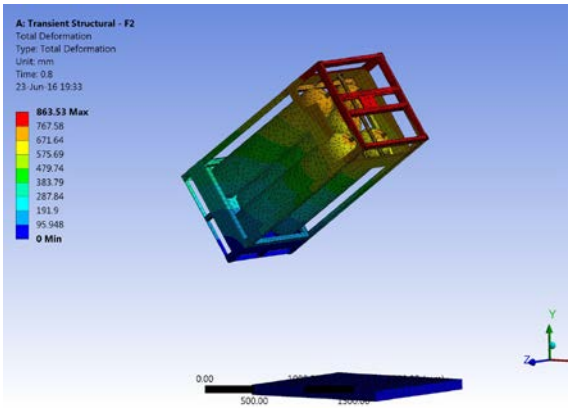


Fig. 12 *Position of the bundle at time t=0.8s*

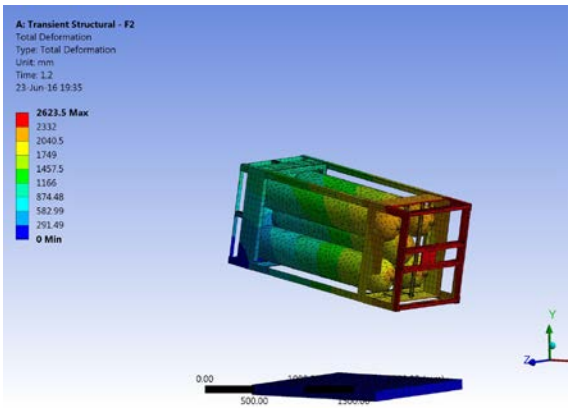


Fig. 13 *Position of the bundle at time t=1.2s*

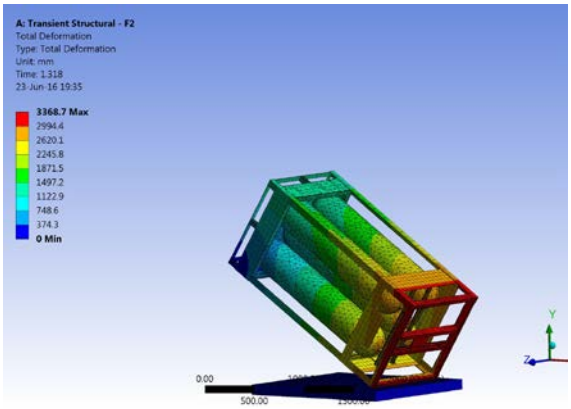


Fig.14 *Position of the bundle at time t=1.318s*

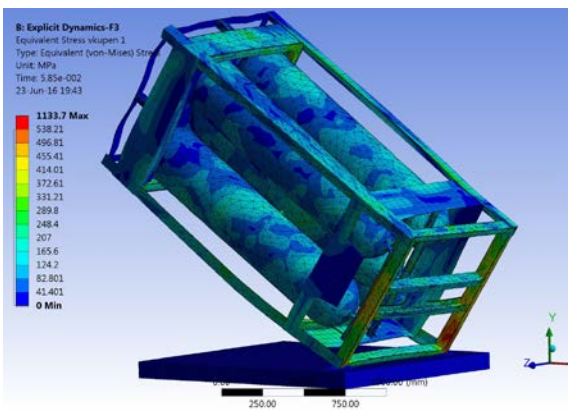


Fig. 15 *Equivalent stresses in the bundle at time t=0.0585s*

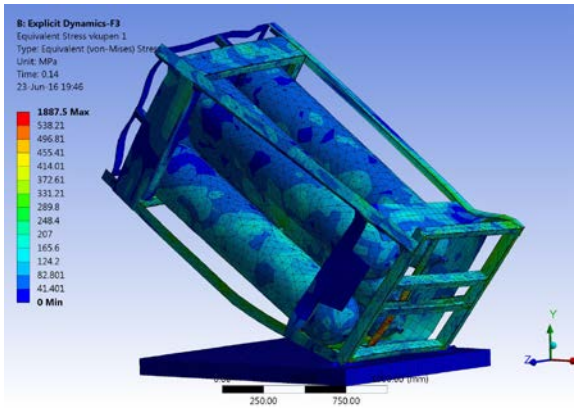


Fig. 16 *Equivalent stresses in the bundle at time t=0.14s*

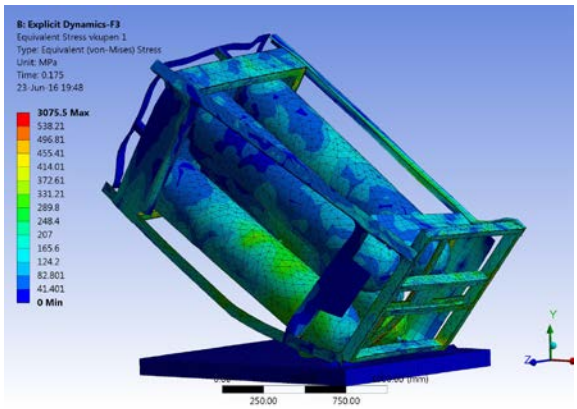


Fig. 17 *Equivalent stresses in the bundle at time t=0.175s*

The explicit dynamics analysis points out that the total deformations during the impact jeopardize the space where the cylinder valves and the manifold are mounted (fig. 18). As a result, the valves and the manifold could be damaged and a gas leakage could appear.

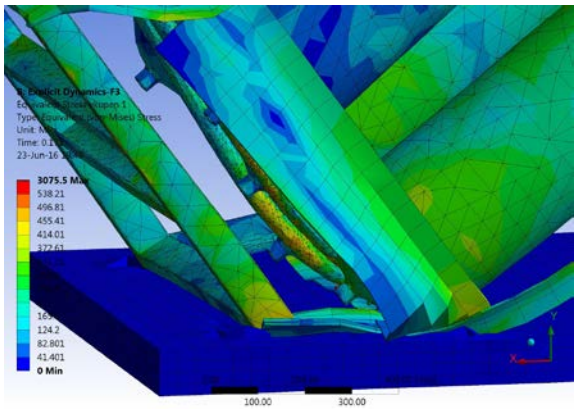


Fig. 18 *Space where the cylinder valves and the manifold are mounted at time t=0.175s of the explicit dynamics analysis*

The equivalent stresses which appear in some segments of the bundle are over the ultimate stress of the material. The range of the maximal stresses at the end of the analysis is about 3000 N/mm^2.

The maximal stresses, which appear in the vertical beams of the bundle, range between 417.34 N/mm^2 and 614.46 N/mm^2. Despite these high values, the maximal plastic deformations range between 10.27% and 20.989% of the size of the part's final elements. These results show that during the impact there is no failure in the vertical beams structure, but on the other hand there is a failure in the connections between the front left beam, the upper rectangular frame and the middle side plate (fig. 19). This could lead to significant cylinder movement, gas leakage and exclusion of the possibility for subsequent movement of the bundle by fork-lift truck or slinging.

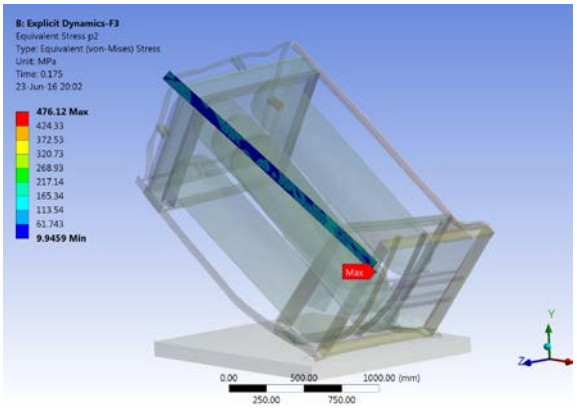


Fig. 19 *Failure of the front left beam connections*

The impact of the bundle brings up to tearing of the pre-tensioning bolts or failure of the connection between the bolts and the pipes that secure the cylinders (fig. 20). The equivalent stresses in the bolts range up to 700 N/mm^2 and the plastic deformations range up to 57% of the size of the part's final elements.

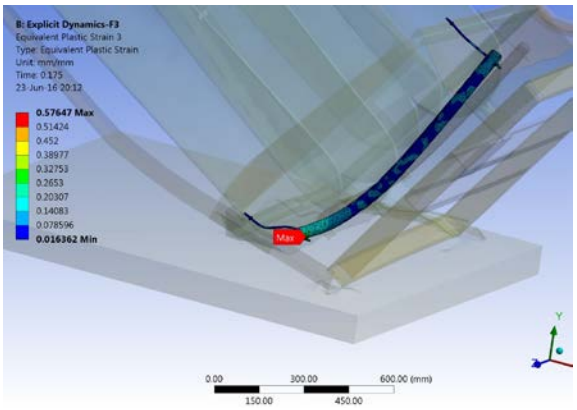


Fig. 20 *Plastic deformations of the front bolts and pipe*

The highest equivalent stresses appear in the middle frame of the bundle in the areas where the cylinders lean on the frame. Their range in these areas is between 700 N/mm^2 and 1100 N/mm^2. The maximal equivalent stress is 3075.5 N/mm^2. The range of the plastic deformations is between 50% and 82% of the size of the appropriate final elements. The maximal plastic deformation is 195.27% of the size of the appropriate final element. These results imply on crush of the middle frame in the areas where the cylinders lean on (fig. 21).

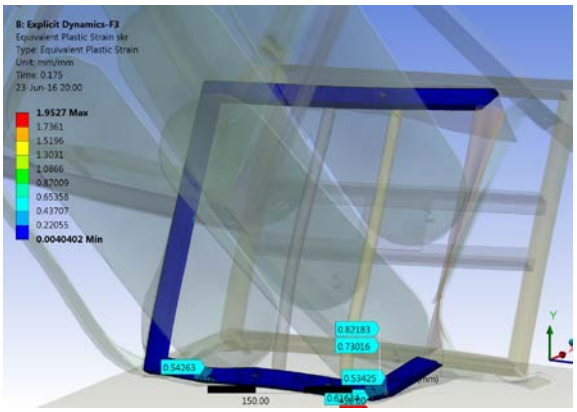


Fig. 21 *Plastic deformations of the middle frame of the bundle*

The results of the performed analyses point out that the bundle does not satisfy the requirements as defined in point 7.2.2.3.4 of the international standard ISO 10961:2010(E), regarding the rotational drop test.

4. Conclusion

The research presented in this paper produced numerous results which serve as a base for the following conclusions. At this stage, without validation, the developed virtual model of the cylinder bundle can be used only in preliminary structural and dynamics simulations. The real cylinder bundle would satisfy the requirements as defined in point 7.2.2.3.4 of the international standard ISO 10961:2010(E), regarding the vertical drop test. Despite this, the real cylinder bundle would not satisfy the requirements as defined in point 7.2.2.3.4 of the international standard ISO 10961:2010(E), regarding the rotational drop test. Also, the results of the virtual testing pointed out the possible weaknesses of the structure of the bundle. They can serve as a base for further improvement of the model and ultimately of the real bundle too. The experimental tests of the real bundle should be conducted only after the model passes the virtual testing. This methodology saves time and resources. The results of the experimental tests could be further used in the validation process of the model and most important in the validation process of the virtual testing.

5. References

[1] American Society of Mechanical Engineers (2006). “Guide for Verification and Validation in Computational Solid Mechanics”, 2006. Standards Committee on Verification and Validation in Computational Solid Mechanics (PTC 60/V&10).

[2] Andre Eggers, Holger Schwedhelm, Oliver Zander, Roberto Cordero Izquierdo, Jesus Angel Garcia Polanco, John Paralikas, Konstantinos Georgoulias, George Chryssolouris, Dominic Seibert, Christophe Jacob, “Virtual Testing based Type Approval Procedures for the Assessment of Pedestrian Protection developed within the EU-Project IMVITER”, The 23rd International Technical Conference on the Enhanced Safety of Vehicles (ESV) Seoul, Republic of Korea, May 27-30, 2013.

[3] ANSYS Inc., Release 15.0, “ANSYS Mechanical User's Guide”, Southpointe 275 Technology Drive Canonsburg, USA, 2013.

[4] COMMISSION REGULATION (EU) No 371/2010 of 16 April 2010, replacing Annexes V, X, XV and XVI to Directive 2007/46/EC (Framework Directive).

[5] COMMISSION REGULATION (EC) No 631/2009 of 22 July 2009 laying down detailed rules for the implementation of Annex I to Regulation (EC) No 78/2009 of the European Parliament and of the Council on the type-approval of motor vehicles with regard to the protection of pedestrians and other vulnerable road users, amending Directive 2007/46/EC and repealing Directives 2003/102/EC and 2005/66/EC.

[6] Curtis Waguespack, “Mastering Autodesk Inventor 2014 and Autodesk Inventor LT 2014”, John Wiley & Sons, Inc., 2013.

[7] International standard ISO 10961:2010(E), Gas cylinders - Cylinder bundles - Design, manufacture, testing and inspection, Second edition, 2010-10-15.

THE RESEARCH OF NEW TECHNOLOGY OF PLATE ROLLING BY MEANS OF COMPUTER SIMULATION

ИССЛЕДОВАНИЕ НОВОЙ ТЕХНОЛОГИИ ТОЛСТОЛИСТОВОЙ ПРОКАТКИ СРЕДСТВАМИ КОМПЬЮТЕРНОГО МОДЕЛИРОВАНИЯ

Prof., d.t.s. Naizabekov A. B. [1], c.t.s. Lezhnev S. N.[1], PhD student Panin E. A. [2], master student Krupenkin I.I. [3]
[1] Rudny Industrial Institute, Rudny, Kazakhstan
[2] University of Chemical Technology and Metallurgy, Sofia, Bulgaria
[3] Karaganda State Industrial University, Temirtau, Kazakhstan
sergey_legnev@mail.ru, cooper802@mail.ru, volkodav-007@mail.ru

Abstract:
The development of new and modernization of existing methods of plate-rolling in order to obtain high-quality and competitive products is a promising task. This paper presents the results of a comparative analysis of the classical plate rolling technology and new technology, including rolling in relief rolls and workpiece alignment on a smooth barrel followed by rolling to the desired size. Comparison of these technologies was carried out with the help of computer simulation methods in finite element software package SIMUFACT FORMING together with a database of materials properties MATILDA. The analysis was conducted by parameters such as: the degree of elaboration of the workpiece, deformation scheme, the evolution of the microstructure. For comparison, the values of the stresses and deformations of the workpieces to be processed on existing and proposed technologies, studied the stress-strain state using the coefficient Lode-Nadai. Analysis results obtained in the course of the simulation allows to predict better quality plate production with the use of the proposed technology plate rolling.
KEY WORDS: *PLATE ROLLING; COMPUTER SIMULATION; ALTERNATING DEFORMATION.*

1. Introduction

High quality and competitive products is the main objective of any production, including plate rolling. However, the characteristic feature for the modern technology of plate rolling are monotonic deformation of compression, which poorly penetrates into the middle layers of the metal, which leads to anisotropy of mechanical properties in volume of the workpiece and reduce the quality of the finished product. A promising direction for improving the quality of hot-rolled sheet, and accordingly further cold-rolled, is the development of new schemes of the deformation in the rolling process, allowing to improve the strength characteristics together with good ductility through grain refinement of the source metal during the implementation of the deformation diagram realizing the intense alternating deformation in the whole volume of deformable metal.

2. Problem discussion

It is known that one of the main ways of achievement of sign-variable deformation in case of various processing of metals pressure is increase shift components of deformation (macroshift). Therefore an important condition of increase in production efficiency of plate hire is use of the local deformations providing creation in peals great importance of the cumulative deformation having sign-variable nature, and also its not monotony [1].To implement these conditions (impossible in classical longitudinal rolling) in practice is required to change the form of rolls or blanks. So one of the main ways of forming is the application of alternating projections and depressions on the surface of the wide faces of the rolls or to the workpiece [2]. Such a change in the form of rolls (or blank) will allow you to create additional streams of metal flow not only in longitudinal but also transverse direction (to the axis of rolling), which consequently will lead to the intensification of shear deformation in the whole volume of deformable metal, as well as the decrease of the anisotropy of the mechanical properties of the metal. However, most often, in practice, this method is associated with a significant change in the original dimensions of the workpiece, which is undesirable and even negative, since in some cases a significant change in the cross-sectional size (usually decrease) leads to a drastic reduction of the possible range obtainable from a given workpiece. Also a significant change in the original dimensions of the workpiece leads to higher energy consumption, which is not desirable.

In this regard, the development of new or improvement of existing technologies with the aim of creating the most favorable conditions for obtaining high-quality thick plate metal without appreciably changing the original dimensions of the workpiece is an urgent task.

To solve this problem a new rolling technology has been developed, which allows to achieve increase of the quality of the metal plate with small changes in the initial cross-sectional dimensions of the workpiece [3]. Offered plate rolling technology includes rolling mill rolls with relief, executed in the form of trapezoidal protrusions and depressions along the entire length of the roll barrel [3], and the alignment of rolling billets at a smooth barrel to the desired size. This development will allow to intensify the shear deformation, which will ensure the emergence of additional streams of metal flow and, consequently, a better elaboration of the workpiece over the entire volume.

The aim of this work is to conduct a comparative analysis to identify characteristic differences, advantages and disadvantages between the proposed and the existing technology of plate rolling.

3. Objective and research methodologies

To achieve this goal with the help of software package Simufact forming, together with a database of materials properties MATILDA two models of plate rolling were created. Model existing plate rolling technology includes 6 stands with a smooth barrel in series (Figure 1.A). The proposed technique involves the cage with embossed rollers as annular grooves over the entire length and the roll stands 5 mounted in series with smooth barrels (Figure 1.B).

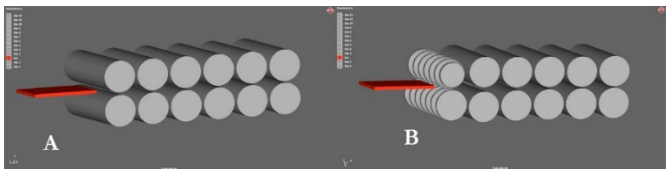


Figure 1 *- The appearance of the constructed models*
A - existing technology; B - the proposed technology

To compare the effectiveness of the models, it was decided to analyze the results on the rolling key stages, namely, after the first, the third and the last stand.

To determine the degree of elaboration of the workpiece at each stage of rolling in each model analyzed the effective plastic strain. The results obtained in the analysis of the results showed that even at the first stand in the rolling degree of elaboration and workpiece quantity of accumulated strain in the preform rolled on the proposed technology (preparation B) is greater than in the existing rolling (preparation A). The difference value reaches 0,087. This

phenomenon can be explained by the fact that the blank B occurs extra metal flow flows in the direction of least resistance.
After the third passage of the effective strain in the workpiece B starts to get uniformity across the section. After rolling in the sixth stand two blanks have a uniform distribution pattern of the accumulated strain. The difference values of the effective plastic strain between the proposed and existing technology reaches 0.45. This difference indicates a more effective elaboration billet rolled on the proposed technology, including rolling in the relief rolls.
In order to evaluate the stresses and strains in the values of the workpiece, as well as the discovery of a common type of deformation at a particular point of rolling a study of stress-strain state using the coefficient Lode-Nadai [4]. To calculate the maximum values have been taken, average and minimum principal stress in points 70 throughout the length of the cross section of the preform. The values of the coefficient Lode-Nadai are in the range from 1 to -1. The values of the coefficient, tending to 1 indicate the nature of the compressive deformation, to 0 to shift the character to -1 on the tensile nature. For a visual representation of the results of the analysis of the Lode-Nadai coefficient are presented in graphs (Figure 2).

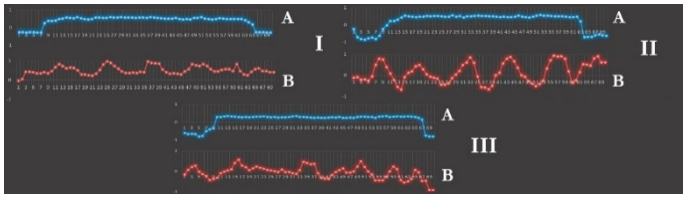


***Figure 2** - The results of the analysis of the Lode-Nadai coefficient A - existing technology; B - the proposed technology; I - first pass; II - the third passage, III- sixth pass.*

Deformation during rolling under the existing technology at all stages of rolling is monotone compressing character except the marginal portions where tensile stresses arise due to band broadening and a front tension band arising due to the difference of rolling speeds. Unlike existing technologies deformation has an alternating character with a large amplitude, dominated by shear deformation when rolling on the proposed technology that is beneficial to the grinding fraction harvesting grain throughout.
From the results of the analysis of the microstructure (Figure 3) that after the first and the third stand more even distribution of the blank has a structure A, but after the third stand in the blank B is equalized grain fractions in the cross section. After rolling the blank in the sixth stand B structure has a uniform distribution of grain size in the range 15 ÷ 20 microns. A grain fraction in the workpiece A in the range 20 ÷ 25 mm, the microstructure is non-uniform structure, which leads to anisotropy properties.

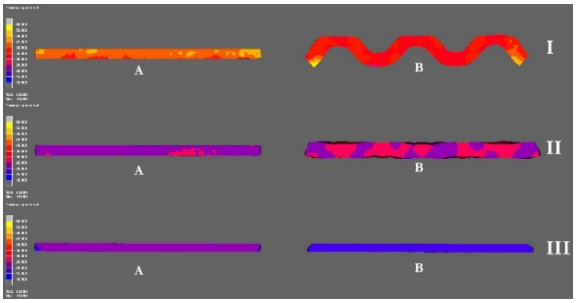


***Figure 3** - Results of the analysis of the microstructure A - existing technology; B - the proposed technology; I - first pass; II - the third passage, III- sixth pass.*

4. Conclusions

A comparative analysis of the proposed and existing technology plate rolling. Compared subjected to parameters such as: the effective plastic strain ratio Lode-Nadai, calculated according to the values of the principal stresses, as well as the evolution of the microstructure. Results of the analysis can be predictive of better quality plate production with the use of the proposed technology.

5. Literature

1. The use of rolling-shift traditional drawing for forming the structure and properties of low carbon steels. / Pashinskaya E., Zavdoveev A. // High Pressure Physics and machinery 2012, Volume 22, № 3. - p. 113-123.
2. Production of sheet metal using a local deformation. / Traino A., Poluhin V. // Rolled products, 2011. №1. - p. 25-31.
3. Patent of the Republic of Kazakhstan № 14791 Rolls for rolling plates. / Naizabekov A., Lezhnev S. 2007. Bull. 11.
4. Processes of metal plastic structure. / Segal V., Reznikov V., Kopylov V. etc. // - Minsk: Science and technology, 1994. – 232p.

MECHANICAL PROPERTIES AND EDDY CURRENTS IN 20CrMo5 LOW – TEMPERATURE TEMPERING OF VARIOUS DURATIONS

МЕХАНИЧНИ СВОЙСТВА И ВИХРОВИ ТОКОВЕ ПРИ НИСКОТЕМПЕРАТУРНО ОТВРЪЩАНЕ НА СТОМАНА 20CrMo5 С РАЗЛИЧНА ПРОДЪЛЖИТЕЛНОСТ

Ivanov J.St., MSc

"M+S Hydraulic"AD Kazanlak, Bulgaria
jeanivanov@yahoo.de

Abstract: *The subject of our study is the effect of the tempering duration /for up to 7 hours, at 180°C/ on the mechanical properties of 20CrMo5 quenched steel samples. Possibilities were studied, including through eddy currents, to control the final tempering of parts which have gone through carburizing, double-quenching and interim high-temperature tempering. The parts were 20CrMo5 steel shafts, which had their carburized layer removed in certain zones before the thread was made.*

It has been established that a strong correlation exists between the HV50 quality indices and the eddy currents characteristic Z.

KEYWORDS: LOW-TEMPERATURE TEMPERING /LTT/, CARBURIZING, QUENCHING, THREADS, EDDY CURRENTS, HOLLOMON-JAFFE

1. Introduction

A number of carburized parts have sections which do not need to be quenched to a maximum hardness. Such areas have a specific function or they are located outside the main performance characteristics range [4]. For instance, in the hydraulic motor structure such examples are the external threads of output shafts with a conical coupling section. The threaded area is the object of special attention during carburizing due to the possible concentration of all kinds of defects resulting from this thermochemical processing: high levels of residual austenite, emergence of free carbides and a carbide network, deeper decarburized layers [1, 2]. On the other hand, the formation of threads through grinding or plastic deformation /rolling/, further deteriorates the negative consequences of carburizing.

With thread made with a cutting tool, we can observe that the metal texture banding gets interrupted, while with parts with different texture and hardness, and with progressing tool wear, defect zones are formed at the base of the thread.

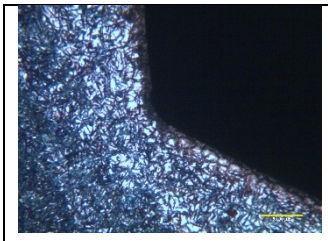


Fig.1. *Microstructure at the root between 2 thread crests, Scale 50µm.*

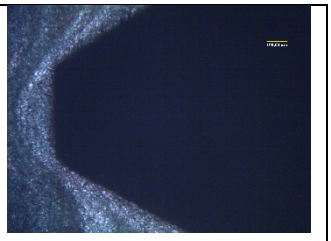


Fig.2*. Microstructure at the root between 2 thread crests, Scale 100µm.*

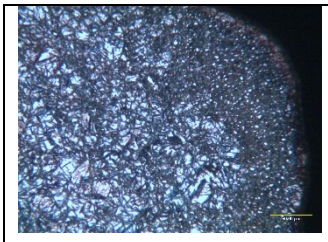


Fig.3 *Microstructure at the thread crests, Scale 50µm.*

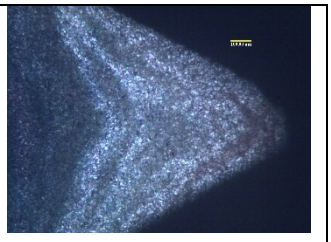


Fig.4. *Microstructure at the thread crests, Scale 100µm*

Another technological option is thread formation through plastic deformation [13]. The characteristic structure of such threads after thread-rolling and after carburizing is illustrated in Fig.1, 2, 3, 4. Depending on the steel properties, a zone of excessive density is formed in the area of maximum plastic deformation, Fig.2. When the material "flows out" towards the external diameter of the thread, two layers meet, which in certain circumstances do not weld together, and when the material is insufficient, the profile is not filled, Fig.4.The thread crest is saturated with carbide phases, and the residual austenite quantity is considerable, and unevenly distributed depending to the microstructure banding, Fig.3. A narrow oxidized layer can be observed on the surface. The microstructural banding in the excessive density area results in significantly decreased distances between the separate bands, Fig.2. Consequently, the chemical inhomogeneity effect is stronger, too. Apart from everything mentioned above, it should be taken into consideration that the degree of plastic deformation is different at the root and at the entry/exit point of the thread.

With respect to carburizing, quenching and tempering, the threaded zone is especially sensitive to the processing mode. The smaller forms, in comparison with the shaft body, are heated up quickly, and take in carbon, which spreads and equalizes its concentration across the whole cross section. During cooling, prior to quenching, conditions develop in the profile for the release of carbon which exceeds the equilibrium quantity in the form of carbides and considerable amounts of austenite do not turn into martensite, Fig.3. If these peculiarities describe the microstructure, the inhomogeneity on a macrostructural level related to the outcomes of thermochemical processing increases due to the furnace unit specifics, the batch quantity, the fluctuations in the chemical composition within the same grade, etc.

Regarding exploitation, the thread is under tensile stress, and when there is residual tensile stress [2, 5], the risk of premature and unpredictable destruction is increased.

Taking these peculiarities into account, there are many possible technological measures for preventing premature destruction in the area of the thread, but some of them could be the following:

1. Careful investigation of the effect of LTT technological factors, temperature and time, both for carburized and protected thread, as well as for the cases when the carburized layer has been removed.
2. Protection of the threaded zones from carburizing [4].
3. Removal of the carburized layers, thread cutting and final quenching of parts [4].
4. Manufacture of the threaded part from a different material.

The need for strict measures like those mentioned above lies in the fact that the early destruction in the area of the thread leads to the end of life of the engine as a whole, and on the other hand, it puts the safety of the personnel operating it, and others surrounding them, at risk.

Just like all other threaded connections, this type, does not guarantee any tensile strength either, nor the plastic or performance properties after carburizing, quenching and tempering [6]. That is why, the determination of the mechanical properties of the base material throughout the technological process is of primary importance for the reliability of the hydraulic motor.

2. Object of research

Samples of 20CrMo5, WN 1.7264 steel were made for mechanical trials and hardness measurements.

Steel is the main material for the manufacture of hydromotor shafts and has the following chemical composition, Table 1.

Table 1. *Chemical composition of steel 20CrMo5*

	%C	%Si	%Mn	%P	%S	%Cr	%Mo
Min.	0.18	0.15	0.90			1.10	0.20
Max.	0.23	0.35	1.20	0.035	0.035	1.40	0.30

The trials carried out involved the following sequence of stages:

1. Mechanical processing and first quenching from 860 °C.
2. High-temperature tempering - 695 °C/4 h.
3. Final quenching from 860 °C.
4. Tempering at 180 °C for 30, 60, 120, 240, 420 min.

The given sequence aims to study the changes in the carburized steel core. The difference from real parts lies in the lack of carburizing.

3. Objectives of research

The research aims to determine the mechanical properties of steel in the area of the thread after going through the described modes of thermochemical and mechanical processing. Also, it aims to draw up a control plan, to determine the area for quality control of every shaft and draw up a control plan, and to determine the tensile strength class of the thread according to ISO 898-1:2009 [12].

4. Methodology of research

Measurements were made of Vickers hardness - HV50, БДС EN ISO 6507-1[10] and the eddy current characteristic, ***Z*** [7, 8, 9]. Mechanical trials were conducted in accordance with BDS EN 10002-1[11] and the tensile strength R_m was established, as well as the conditional yield strength $R_{p0,2}$. The results were presented graphically and correlations were analysed. The results were evaluated in the light of the Hollomon-Jaffe correlation [3, 4], i.e. considering the joint effect of the two technological factors of LTT: temperature and time.

(1) $P_a = T^*(C+\log \tau)$

where: C is a constant value, in this case equal to 20; T - temperature [°K]; τ - time [min].

5. Test results

The test results are presented in Table 1.

Table 1. *Mechanical properties and the eddy current characteristic depending on LTT duration*

TAUan [min]	P_a (HJ)	HV50	Z	R_m [MPa]	$R_{p0,2}$ [MPa]	$R_{p0,2}$*100/ R_m [%]
0	9060	438	4,4	1467	1129	76.9
30	9729	434	5	1457	1160	79.6
60	9866	456	2,25	1456	1166	80
120	10002	424	5,25	1439	1160	80.6
240	10138	424	4,7	1433	1171	81.7
420	10248	394	6,25	1435	1182	82.4

Fig. 5, 6, 7, 8 are the graphical representation of the correlations of hardness, the eddy current characteristic and the conditional tensile strength and yield strength values.

The eddy current characteristic, ***Z*** is recorded at different operating frequencies. With operating frequency of 5 KHz, Fig.5., the test measured the highest correlation coefficient with hardness HV50 .

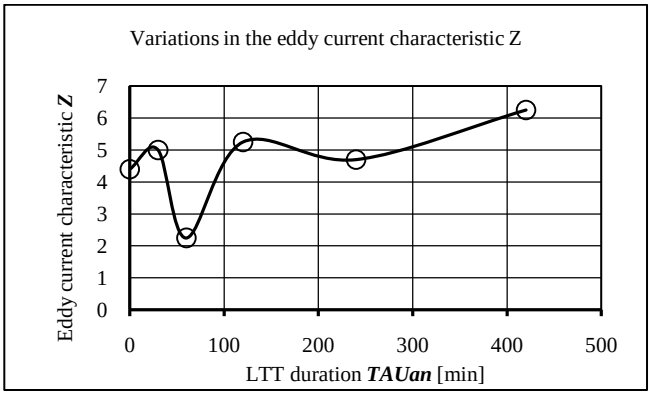


Fig.5. *Variations in the eddy current characteristic Z depending on the LTT duration*

It was established that the HV50 hardness smoothly changes with the increased LTT duration. The "jumps" in the variation of hardness for ***TAUan*** = 60 min were confirmed by means of the eddy current testing and they need to be further investigated through additional experiments. A significant change in the hardness occurred after 240 min.

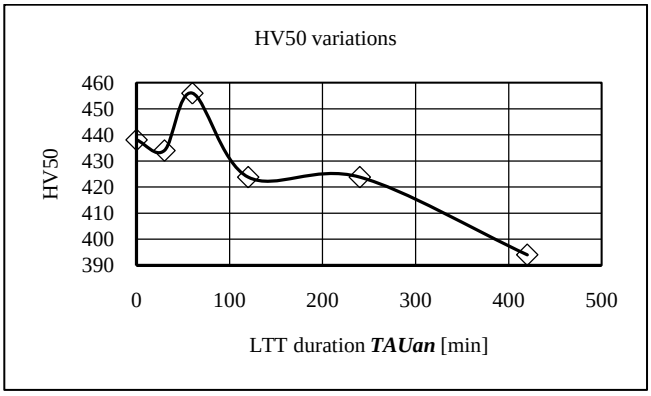


Fig.6. *Variations in the HV50 hardness depending on LTT duration*

A correlation analysis was used to examine the HV50 hardness and the eddy current characteristic, ***Z***. The analysis defined a strong negative correlation with a correlation coefficient R= -0,911, while the correlation analysis of ***Z*** and the conditional tensile strength and yield strength defined a weak and a missing correlation, respectively.

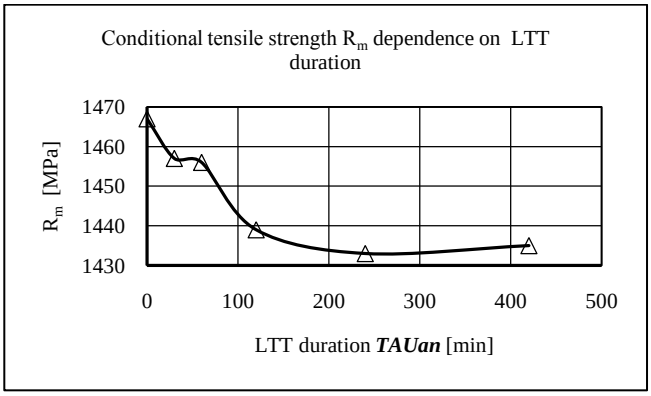


Fig.7. *Variations in the conditional tensile strength depending on LTT duration*

The conditional tensile strength R_m diminishes smoothly for the duration of 240 min, after which it remains almost constant, Fig.7.

If we ignore the intermittent "jumps" in yield strength for 60 min of LTT, Fig.8, we can accept that there is a rising tendency in the studied mechanical property. The absolute values of the two maximum variations of the tensile strength and the yield strength, at the start and the end of the process are approximately the same: 30-50 MPa.

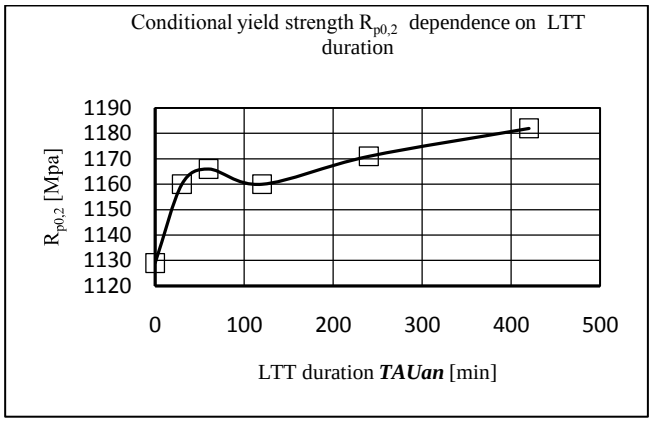


Fig.8. *Variations in the conditional yield strength $R_{p0,2}$ depending on LTT duration*

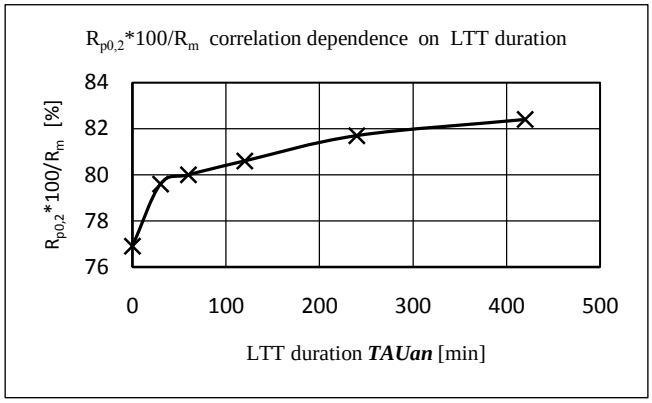


Fig.9. *Variation in the correlation $R_{p0,2}$/ R_m depending on the LTT duration.*

The variation in the $R_{p0,2}/R_m$ correlation is important for defining the thread strength property class. According to ISO 898-1:2009, class 12.9 R_m requires a minimum of 1220 MPa, the yield strength – a minimum of 1100 MPa, and the ratio between the two properties must be 90%. These values are purely conditional as the requirement for minimum 380°C temperature of tempering has not been met. The two strength characteristics have values which considerably exceed the required minimum. Their setting to lower levels would require tempering temperatures, which would lower the hardness below 59 HRC as well as other properties in the carburized and quenched zones of parts. With such limitations the thread quality is mainly dependent on the relative elongation A%.

The results obtained, Fig.9; 10, show that with 180°C LTT and an increasing duration, there is a tendency of rising and approximating the 90% ratio. After 240 min of tempering this tendency is mainly maintained by the increased yield strength.

Considered in the light of the Hollomon-Jaffe dependence, the variation in the ratio between the two strengths gives the possibility to complement the existing data with such for LTT temperatures, which are different from the studied one here - Fig.10.

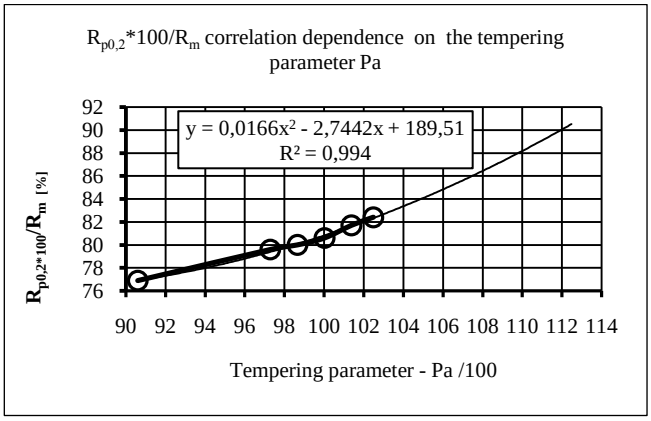


Fig.10. *Variation in the $R_{p0,2}$/ R_m correlation depending on the tempering parameter Pa.*

The polynomial interpolation of the data shown in Fig.10 is with a high coefficient of determination R^2=0.994 and it enables us to calculate the tempering parameter forecast value which will ensure a 90% ratio between the two strengths. With a temperature of LTT ***Tan***=180°C, this result will take 40000 min to achieve, or more than 670 h, i.e. $\boldsymbol{P_a}$=11160. If we accept that the Hollomon-Jaffe correlation is fully valid for LTT, the same value for $\boldsymbol{P_a}$ is possible to achieve at ***Tan***=200°C and ***TAUan***= 3870 min, or at ***Tan***=220 °C and ***TAUan***= 425 min.

6. Conclusions

Predictably, the existence of at least 2 zones of different surface hardness after carburizing, quenching, and LTT on the same workpiece presupposes an automatic increase in the number of control points. The differentiation of a control point in the area with removed carburizing is related to the formation of a special surface area for hardness measurements and eddy current testing. This must feature in the control plan as well as the respectively prescribed requirements. The periodical mechanical testing for defining the tensile strength class can be carried out much less frequently if there is accumulated data of parts from a number of batches/lots. The non-destructive eddy current testing allows checking all parts within a short time. The results make it clear, that although conditionally, the requirement for the relation between the tensile strength and the yield strength can be met if the LTT duration is long enough, which, however, is not cost-effective and would be a great obstacle for the production rhythm. That is why, in view of the primary effect of temperature as a technological index, it would be appropriate to carry out LTT at higher temperatures, e.g. 220 °C. The results obtained can also lead to defining the sensitivity of the eddy current testing to the LTT technological factors. The search for optimal operating frequencies can be assisted by a correlation analysis. There is evidence which confirms the joint influence of the two technological LTT factors, temperature and time, on the mechanical properties of parts.

7. Literature

1. Lahtin U. M. , B. N. Arzamasov, Thermochemical processing of metals, Moscow, Metallurgy, 1985, p.60-70 .
2. Quality control in the heat treatment of steel parts and semi-finished goods, Reference book, Moscow, machine building, 1984, p.196-222 .
3. Berns H., Stahlkunde für Ingenieeure, Springer Verlag, 1993, S.48.
4. Liedtke D., R.Jönsson, Wärmebehandlung, Expert Verlag, 1998, Renningen-Malmsheim , S.43;169.
5. Bacher-Höchst M., O. Vöhringer, Kenntnisstand zum Verformungs-und Bruchverhalten, einsatzgehärteter Stähle, HTM44(1989), S. 240.

6. Wiegand H., K.-H. Kloos, Thomala W., Schrauben-verbindungen: Grundlagen, Berechnung, Eigenschaften, Handhabung,SpringerVerlag, Berlin Heidelberg GmbH, 1988, S.144
7. Tsvetkov D., P. Kostadinov, B. Vasilev , St. Staykov, St. Guninski, Electromagnetic defectometrix, "Technology" 1981, p.190-211
8. BDS EN ISO 15549 General Principles.
9. Popov Al., Eddy current testing, Training tool, Sofia, 2015
10. BDS EN ISO 6507-1 Metallic materials-Vickers hardness test- Part1: Test method
11. BDS EN 10002-1, Metallic materials- Tensile test – Part1: Method of test(at ambient temperature)
12. ISO 898-1:2009 Mechanical properties of fasteners made of carbon steel and alloy steel – Part 1: Bolts, screws and studs with specified property classes – Coarse thread and fine pitch thread
13. Tschätsch H., J. Dietrich, Praxis der Umformtechnik, Vieweg+Teubner Verlag/Springer Fachmedien Wiesbaden GmbH 2010, S. 58

BIOLEACHING OF COPPER SLAGS BY MEANS OF DIFFERENT MICROBIAL CULTURES[*]

Irena Spasova, Stoyan Groudev, Plamen Georgiev, Marina Nicolova, Albena Lazarova

University of Mining and Geology, Sofia 1700, Bulgaria

spasova@mgu.bg

Abstract: *Copper final slags containing 0.62 % Cu, 1.07 % Zn, 0.08 % Co and 32.5 % Fe as the most essential components were subjected to chemical (by means of sulphuric acid and ferric ions) and biological leaching by means of chemolithotrophic microorganisms of three different types: mesophilic and moderate thermophilic bacteria and extreme thermophilic archaea, with temperature optimum at 37, 55 and 75 degrees Celsius, respectively. The leaching was carried out by the shake-flask technique and in agitated bioreactors. The highest rates of extraction of the non-ferrous metals and iron were achieved by means of some archaea but at relatively low pulp densities (5 – 10 %). The moderate thermophilic bacteria were the most efficient for the leaching at a higher pulp density (within 15 – 20 %).*

Keywords: COPPER SLAGS, CHEMICAL AND BIOLOGICAL LEACHING, NON-FERROUS METALS

1. Introduction

The pyrometallurgical slags, mainly from the copper recovery, are wastes containing significant quantities of valuable components (mainly non-ferrous metals such as copper, zinc, cobalt and nickel but also iron and silicon). At present, the slags are used mainly in the construction of roads and for preparation of cements of different types. In some cases old slags rich-in-valuable metals are mixed with some other rich-in-metals raw materials and wastes and are subjected again to pyrometallurgical treatment for an economically attractive recovery of different valuable components. At the same time, a large number of investigations are connected with the chemical and/or the biological leaching of slags for extraction of some of their residual valuable components (Genchev and Groudev, 1981; Arslan C. and Arslan F., 2002; Banza et al., 2002; Kaksonen et al., 2011). It must be noted that the industrial processing of the slags is directly connected with the protection of environment due to the removal of different toxic components which during their storage as wastes are subjected to the natural processes of solubilization and migration. Some data about the possibility to leach some valuable and, at the same time, toxic metals from final copper slags by means of different microorganisms are shown in this paper.

2. Materials and Methods

The slag sample used in this study contained 0.62 % Cu, 1.07 % Zn, 0.08 % Co, 1.90 % S, 32.5 % Fe and 16.3 % Si as the most essential components of its chemical composition. The fayalite (Fe_2SiO_4) and diopside ($CaMgSi_2O_6$) were the main mineral phases in the slags but some oxides, mainly of iron, such as hematite (Fe_2O_3) and magnetite (Fe_3O_4) were also present, as well as some plagioclases, quartz and calcite. The content of pyrite (FeS_2) was relatively low but considerable portions of the non-ferrous metals were present as the relevant sulphides. Copper was present mainly in bornite, covellite and chalcopyrite but also in oxides. Zinc was present mainly as the relevant oxide but also in its own elemental form (Zn^o) and as the sphalerite (ZnS).

A large number of microorganisms were tested in the experiments for microbial leaching of the non-ferrous metals from the slag. Most of these microorganisms were acidophilic chemolithotrophs possessing the ability to oxidize the ferrous iron and/or the low-valence form of sulphur (the sulphidic) and its zero-valence elemental form. These microorganisms were related to three different groups on the basis of the optimum temperature for their growth and activity: mesophilic bacteria, mainly of the species *Acidithiobacillus ferrooxidans*, *Leptospirillum ferrooxdians* and *Acidithiobacillus thiooxidans*, with a temperature optimum at 32 – 37 ^oC; moderate thermophilic bacteria, mainly of the species *Sulfobacillus thermosulphidooxidans* and *Acidithiobacillus caldus*, with a temperature optimum at 50 – 60 ^oC, and extremely thermophilic archaea, mainly of the species *Sulfobacillus metallicus* and some strains related to the genera *Acidianus* and *Metalosphaera* with a temperature optimum within the range of 65 – 86^oC. In these comparative experiments each of the different microbial species mentioned above was presented by 5 – 7 different strains, at least. The experiments of this type initially were performed by the shake-flask technique using Erlenmeyer flasks of 500 ml volume containing 100 ml of 9K nutrient medium with 10 g slag with a particle size minus 100 microns. The cultivation was carried out at 35, 55 or 70^oC for the mesophilic, moderate thermophilic and extreme thermophilic species, respectively. The effect of the most essential environmental factors, apart from the temperature, was studied with the more active strains as follows: pH within the values from 1.0 to 3.7, pulp density – from 5 to 20%, aeration by air enriched with CO_2 to 0.10 – 0.20%.

The activity of some of the most active strains from the different taxonomic species was increased to different extents by means of consecutive cultivations in the medium 9K supplied by slags with a step-by-step increasing of the relevant pulp density.

In some experiments the combined chemico-biological leaching of the slags was performed in agitated bioreactors with a volume of 1 l each. Apart from the batch leaching, such bioreactors were used also for performing the continuous-flow leaching. Such leaching was performed not only in a single bioreactor but also in a two-step system consisting of two connected reactors. In the first reactor the initial acidification of the slags was performed by adding sulphuric acid to the relevant pH levels which was the optimal for the growth and activity of the microorganisms acting in the second (bio)reactor.

Elemental analysis of the liquid samples was performed by atomic absorption spectrometry and inductively coupled plasma spectrometry. The isolation, identification and enumeration of microorganisms were carried out by the classical physiological and biochemical tests (Karavaiko et al., 1988) and by the molecular PCR methods (Sanz and Köchling, 2007; Escobar et al., 2008).

3. Results and Discussion

It was found that some of the microbial strains used in this study, even some related to one and the same taxonomic species, differed considerably from each other with respect to their ability to leach the heavy metals from the slags (Table 1 and 2).

Very active strains from the three temperature groups mentioned above were established. The highest rates of extraction of the non-ferrous metals and iron were achieved by means of some archaea but at relatively low pulp densities (5 – 10%). It must be noted that the preliminary adaptation of most strains to the slags used in this study increased to some extend the rates and efficiency of leaching. However, in most cases the increase was different at the different strains, even at such related to one and the same taxonomic species.

Table 1. *Leaching of non-ferrous metals from the slags by means of mesophilic bacteria*

Leaching agents	Cu	Zn	Co
	Extraction, %		
Acidithiobacillus ferrooxidans	71 – 88	75 – 90	70 – 92
Leptospirillum ferrooxidans	55 – 69	60 – 75	64 – 80
Acidithiobacillus thiooxidans	32 – 35	29 – 37	35 - 41
At. ferrooxidans + At. thiooxidans	73 – 92	77 – 91	73 - 95
L. ferrooxidans + At. Thiooxidans	68 - 84	64 - 80	68 - 88
Chemical leaching:			
H_2SO_4 (pH 2.0)	35	37	44
$H_2SO_4 + Fe^{3+}$ (10 g/l at pH 2.0)	51	59	62

The biological and chemical leaching were carried out in agitated reactors at 37°C and pH 2.0 maintained by addition of sulphuric acid. Pulp density 10% in 9K nutrient medium with slags with a particle size minus 100 microns. Duration of leaching 72 hours.

Table 2. *Leaching of non-ferrous metals from the slags by means of moderate thermopilic bacteria and extreme thermophilic arhaea*

Leaching agents	Cu	Zn	Co
	Extraction, %		
Sulfobacillus thermosulphidooxidans	75 - 91	79 – 93	71 – 95
Acidithiobacillus caldus	39 – 47	37 – 49	41 – 50
S.thermosulphidooxidans + At. caldus	77 – 91	76 – 95	73 – 95
Sulfobacillus metallicus	77 – 93	78 – 93	73 – 95
Acidianus sp.	71 - 91	75 - 88	70 - 91
Chemical leaching:			
H_2SO_4 (pH 2.0)	41	46	48
$H_2SO_4 + Fe^{3+}$ (10 g/l at pH 2.0)	57	62	66

The biological and chemical leaching were carried out in agitated reactors at 37°C and pH 2.0 with the moderate thermophilic bacteria (Sulfobacillus thermosulphidooxidans and At. caldus) and 75°C and pH 2.0 with the extreme thermophilic archaea Sulfobacillus metallicus and Acidianus sp.). Pulp density 10% in 9K nutrient medium with slags with a particle size minus 100 microns. Duration of leaching 48 hours.

The addition of yeast extract to the nutrient medium 9K used for the cultivation of archaea usually increased the growth rate, and to some extent, their oxidation rates but in most cases the level of the increase was different. A positive effect of this type was observed also with some strains of the moderate thermophilic bacteria. Some strains of these bacteria were the most efficient for the leaching of slags at higher pulp density (especially of 15 – 20%). However, leaching by some mesophiles at pH 3.0 – 3.5 was very attractive since it was connected with high extractions of the non-ferrous heavy metals, much lower acid consumption and low solubilization of fayalite which resulted in the production of pregnant solutions suitable for the recovery of the dissolved non-ferrous metals.

In any case, the efficient bioleaching of slags was possible only by microorganism possessing ferrous iron oxidizing ability. These microorganisms, such as *Acidithiobacillus ferrooxidans*, *Sulfobacillus thermosulphidooxidans* and *Sulfolobus metallicus*, oxidized the ferrous ions solubilized from the slags during the leaching to the ferric ions. The ferric ions are efficient oxidizers of the most sulphide minerals, including of these present in the slags. However, it is essential to be noted that the role of these microorganisms in the leaching of these slags is not connected only with the generation of ferric ions *in situ*. Some of these microorganisms, such as the three species mentioned above, possessed also sulphur-oxidizing ability and were able to oxidize the sulphide minerals in the slags directly, i.e. without the presence of soluble iron ions. This was demonstrated by the fact that strains of *At. ferrooxidans* possessing both ferrous and sulphur oxidizing abilities were able to leach the slags in the absence of iron ions introduced to the system from outside at much higher rate than strains of *Leptospirillum ferrooxidans* possessing higher ferrous oxidizing ability but not able to oxidize sulphur in different forms (elemental or sulphidic in some iron-free sulphides such as covellite and chalcocite). This was also demonstrated by the fact that strains of *At. ferrooxidans* possessing both ferrous and sulphur oxidizing abilities oxidized the slags at higher rates than strains of *L. ferrooxidans* which were able to oxidize the Fe^{2+} but not only any form of the sulphur in the absence of iron.

References

Arslan, C. and Arslan, F. 2002. Recovery of copper, cobalt and zinc from copper smelter and converter slags. Hydrometallurgy 67, 1-7.

Banza, A.N., Gock, E., Kongolo, K. 2002. Base metals recovery from copper smelter slag by oxidising leaching and solvent extraction. Hydrometallurgy 94, 18–22.

Escobar, B., Bustos, K., Morales, G. and Salazar, O., 2008. Rapid and specific detection of Acidithiobacillus ferrooxidans and Leptospirillum ferrooxidans by PCR, Hydrometallurgy, 92, 102 – 106.

Genchev, F.N. and Groudev, S.N., 1981. Utilization of copper slags by using combined bacterial and conventional methods, in: XV Scientific Conference on Mineral Processing, Krakow, Poland, October 24, 1981.

Kaksonen, A.H., Lavonen, L., Kuusenaho, M., Kolli, A., Närhi, H., Vestola, E., Puhakka, J.A., Tuovinen, O.H. 2011. Bioleaching and recovery of metals from final slag waste of the copper smelting industry. Miner. Eng. 24, 1113–1121.

Karavaiko, G.I. , Rossi, G., Agate, A.D., Groudev, S.N. and Avakyan, Z.A. (Eds.), 1988. Biogeotechnology of Metals. Mannual, Center for International Projects GKNT, Moskow.

Sanz, J.I. and Köchling, T., 2007. Molecular biology techniques used in wastewater treatment: an Overview, Process Biochem., 42, 119 – 133.

COMPARISON OF NUMERICAL AND EXPERIMENTAL RESULTS OF STRESS-DEFORMATION STATE IN A PIPELINE BRANCH

Prof. dr Bajić D. PhD[1], M.Sc. Ćulafić S.[1]
Faculty of Mechanical Engineering – University of Montenegro, Montenegro [1]
stefanc@ac.me

Abstract: *The subject of this paper is the analysis of stress distribution of the pipeline branch in hydropower. Pipe branches are widely used and very in complexity of the shape. Behaviour of the pipe branch subjected to the internal pressure was analyzed both numerically and experimentally. Analytical stress calculations are limited on the simpler forms of branches, so numerical calculations had to be used. Focus of numerical analysis was on determining critical locations and its values. Strain gauge method was used to measure greatest stress concentrations on the defined locations. Experimental results were very close to numerical calculations. Material used for manufacture of the pipeline branch is NIOVAL 47. This paper can be used as the base for the future researches concerning stress distribution in other branches among the pipeline both numerically and experimentally.*

Keywords: strain gauges, pipeline branch, stress concentration factor, finite element method, numerical calculation

1. Introduction

Reason for the detailed research of the A6 (Figure 1.) branch on the C3 pipeline in the HP Perucica lies in the necesity of adding one generator and thus to increase the production capabilities of HP. It is necessary, among other, to perform detailed stress analysis, so the further activities can be planed. Installation of the generator would increase dynamic loads of the branch. This is why it is useful to have real image of the branch loads in static conditions, so it could be verified through the detailed calculation of dynamic loads if there is space for generator implementation.



Fig. 1 *Branch A6 after reconstruction*

Pipeline branch geometry is basically very complex as seen in Figure 2. This means that on the local level, on the some places of the branch, big geometric irregularities can be noticed. In places of branch geometric irregularities, when certain geometric values, which define branch geometry, suddenly change, also the values of the stress in the branch material changes.

Changing the internal pressure of the pipeline and branch, on the places of geometric irregularities stress values can't be controlled with known theoretical processes of the stress analysis. So, it is very important to try to define stress concentration factor.

Topic of this paper is the analysis of stress distribution of pipeline branch subjected to internal pressure.

Various analysis have to be performed in order to validate the integrity of real structures. These analysis depend on the criticality, loads, and geometry. In the case of branch designing many factors such as: branch shape, manufacturing materials, stress calculation etc., have to be considered. Stress calculation is possible only in the domain of the regular geometric shapes, and is defined by standards for pressure vessels.

Many engineers use various software packages for calculations based on finite element method. Paper [2] showed it was possible to easily implement elastic compensation method to any Finite Element Code in order to enable simpler determination of limit loads in complex structures. In papers [3] and [4], the authors studied limit load solutions for branch connections (with straight branch to run angles) under different loads. In paper [5], static finite element method is performed for analysis of piping system and the pipe branch in order to determine extreme stress values. The most loaded parts of the pipe branch were analyzed by experimental tensometric method. This way, by combining numerical and experimental analysis, it was possible to obtain stress distribution of the whole pipeline. By analyzing obtained stress values, it was possible to evaluate stress concentration factor for the pipe branch model, which can be applied on the structures with similar geometry[1].

2. Finite element method

Special attention during the preparation of this paper was devoted to the analysis of branch with finite element method. From the accuracy of obtained data depends whether it can be expected that the real branch can be credibly displayed in the commercial software. This question has been raised because of the complexity of the geometry, irregularities and stress concentration, incomplete technical documentation, etc. If the comparative analysis of the obtained data show that the geometric model of real branch is acceptable, then it can be an important incentive for further research, because it does not have to be conducted on a real branch but can be used for the geometric model. Due to the size and inaccessible terrain on which branch is this may represent a significant contribution in the future. Branch A6 is made of a material Nioval 47. Basic dimensions of the branch at the entrance is D1 = 2500 mm, while the diameter of the branches at the exit: D2 = 2250 mm. Branch length L = 4300 mm, while the thickness is s = 36 mm. There are segments of the branch with thickness of 50mm, and for these segments are welded so called branch collars.

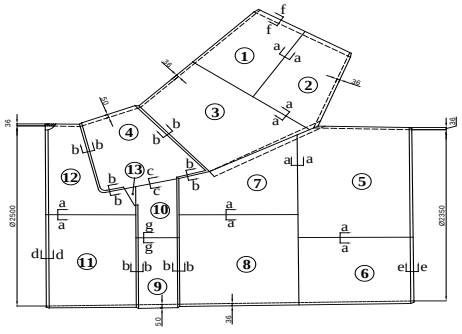


Fig. 2 *Branch A6 tecnical documentation*

Based on earlier researches [1] critical spots on the branch model are defined and experimental and numerical calculation of stresses in critical points (measured points) are conducted. Using the similarity, applied to pipelines under pressure when bending stresses are considered small, thus losing the non-linearity of the problem, it is possible to assume that the stresses at critical points are to be about the same on a real branch and branch model, if the

conditions of boiler formula are satisfied when creating branch model.

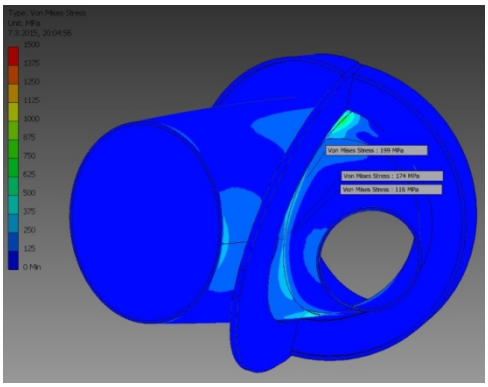


Fig. 3 *FEM model of the branch*

Geometrical modeling and stress deformation analysis is preformed using AUTODESK INVENTOR 2012 as FEM software.

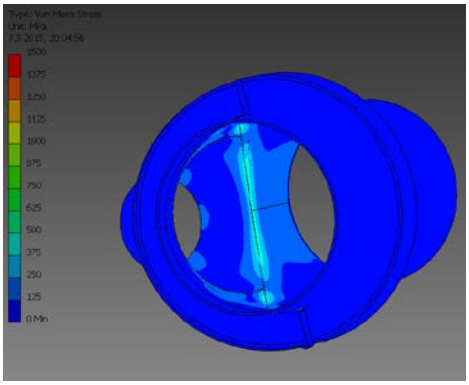


Fig. 4 *Critical strip of FEM branch model pressure 20 bars*

Reviewing results of the analysis preented in the Figures 4, 5, 7, 8, it can be concluded that the biggest Von Misses stresses of branch apears in the area next to branch collar. Von Misses stresses are given in the table 1.

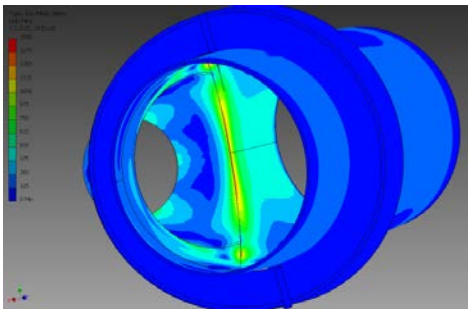


Fig. 5 *Critical strip of FEM branch model pressure 50 bars*

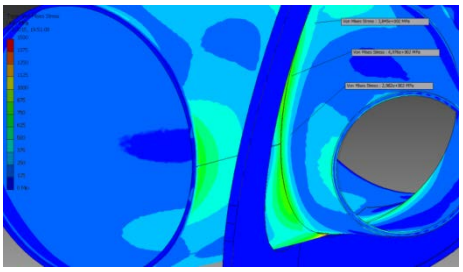


Fig. 6 *Anchor of FEM branch model*

Table 1: *VonMisses stresses values for MP1*

Pressure values [bar]	Maximum stress values for MP1 [MPa]
20	111
50	234
84	458

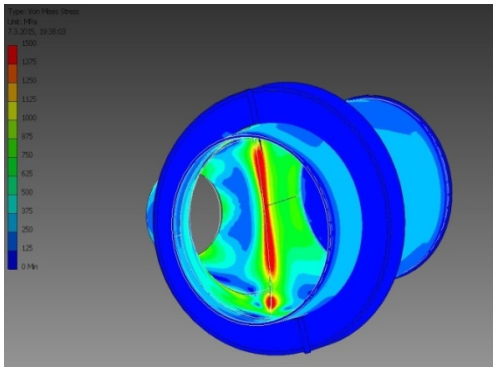


Fig. 7 *Critical strip of FEM branch model pressure 84 bars*

The results of numerical analysis of real branches shows that critical zones, when stress value is concerned, are exactly as the points obtained by branch model analysis [1] (with smaller geometry) both experimental and numerical method. This leads to the conclusion that the tests can be based on numerical methods and analysis models, without the necessary tests of the branch in real conditions. Dominant loads in all the tests that were performed figure as loads of stretching the material, which leads to the appearance of cracks in critical areas. This is also confirmed by the linear dependence of the critical stress loads, which means that bending loads of branch are not dominant.

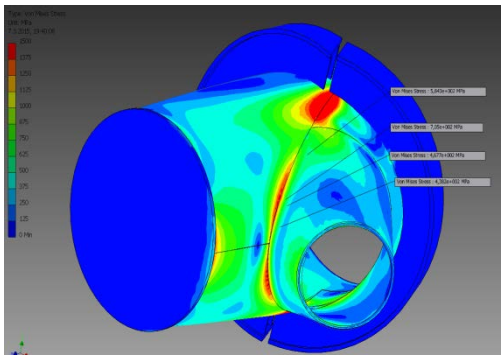


Fig. 8 *Critical strip of FEM branch model pressure 84 bars*

3. Experimental measuring

Experimental research on the branch model (Figures 9, 10, 11) were conducted in order to verify the assumption that the real branch is possible to replace in analasys with the branch model. This can be carried out in strict compliance with the conditions defined by the boiler formula. Calculation of stresses in the branch structure analytically is possible and correct only on the cylindrical part of branch excluding stiffeners, ribs and holes. This calculation is defined also with the standards for pressure vessels. The formula by which calculationes of the stress is carried out in this case is called the boiler formula.

Boiler formula for calculating stresses on the cilinder loaded with internal pressure without ribs and holes is:

- cilinder circumferential direction $\sigma^o = \frac{p \cdot R}{t}$

- cilinder longitudinal direction $\sigma^p = \frac{p \cdot R}{2 \cdot t}$

where: p [bar]- fluid internal pressure,

R [mm]- cilinder radius,

t [mm]- cilinder thickness.

From previous equations it can be seen that values of stress in circumferential direction twice bigger from the values in the longitudinal direction - $\sigma^o = 2\sigma^p$.

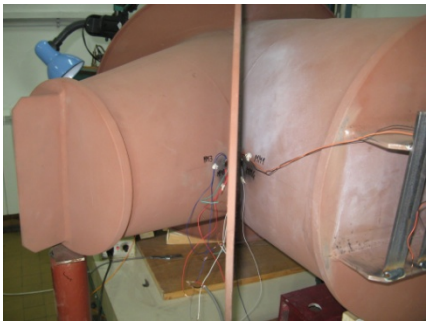


Fig. 9 *Branch model with strain gauges*

Branch model should give same stress as real branch. This is secured with the similarity method as follows:

$$\sigma^o = \frac{p \cdot R}{t} \left(= \frac{\frac{p}{2} \cdot \frac{R}{5}}{\frac{t}{10}} \right) = \frac{p_{mod\,ela} \cdot R_{mod\,ela}}{t_{mod\,ela}}$$

Obtaining the values of the same stress is secured as follows:

$$p_{mod\,ela} = \frac{p}{2} \qquad R_{mod\,ela} = \frac{R}{5} \qquad t_{mod\,ela} = \frac{t}{10}$$

Real branch: p = 50 bar, R = 1250 mm, t = 36 mm, σ^o = 174 MPa.

Branch model: p = 25 bar, R = 250 mm, t = 4 mm, σ^o = 156 MPa.



Fig. 10 *Branch model in laboratory*

This means that the branch modelfor twice the value of the pressure has twice the value of circumferential stress, or that branch model should be loaded with twice as less pressure to be correlated with the real branch. For creation and load of the model following relations are adopted. Since there was no sheet thickness of 3.6 mm, it was necessary to apply a sheet thickness of 4 mm. In this way, a smaller stress is obtained in the sheets of the newly selected thickness by about 10%. The stress on the anchor (ellipse) is same in the model and the real branch since the thickness are of 8 mm and 80 mm. Similarities method we could apply to this branch model, because in its structure there is very little presence of bending stresses which depend on the square of the material thickness (t^2). Based on the reading of all the diagrams stress value is defined at all measurement locations for the pressure of 10 bar and they are given in table 2:

Table 2: *Measuring results*

Pressure [bars]	Stress[kN/cm^2] - Measuring point							
	MP1	MP2	MP3	MP4	MP5	MP6	MP7	MP8
10	11	7.5	5	-	1	0.5	4	3.3

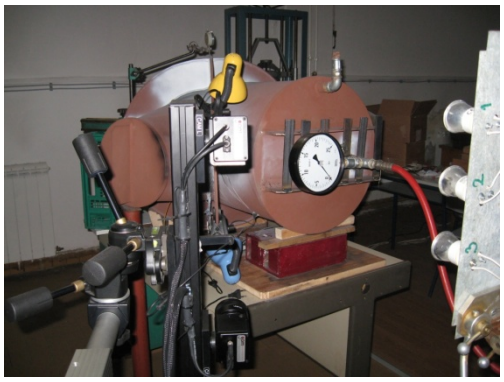


Fig. 11 *Measuring equipment*

Stress values at any pressure until the limit of the strength of material is obtained in the way that values from the table are multiplied with the ratio of the desireable pressure and pressure of 10 bars. Research pressure is adopted as twice smaller than real branch exploatation pressure and limit of the materials strenght of branch model is S355J2+N (Č.0563) 36 KN/cm^2 (KN/cm^2=10MPa).

4. Discussion of the results

Based on the previously presented data in the previous sections of this paper, it is possible to reach the following conclusions:

Table 3: *Comparison of obtained values*

Measuring point No:	MP1	MP2	MP3	MP4	MP5	MP6	MP7	MP8
Experimental [MPa]	110	75	50	-	10	-	40	33
FEM branch model [MPa]	107	84	63	-	11	-	45	31
FEM real branch [MPA]	111	86	73	-	13	-	47	31

Places that includes a narrow strip at the junction of the anchor and pipe are recognized as places with a maximum intensity of stresses. This is confirmed by numerical analysis of branch model, and the real branch, and also at experimental measurments on the branch model which can be seen in the fugures.

Comparative results of all three studies are given in Table 3. The coincidence of the critical stress intensity in numerical analysis on the real branch A6 with the results obtained at experimental branch model analysis thus justifying the application of the boiler formula, based on which is shown geometrical similarity between the model and the real branch. As stated before, this similarity enables proper application of the proportionality of pressure to form the corresponding stresses, which are confirmed by numerical analysis of the branch model.

Analysis of the results presented in Table 3 leads to the conclusion that the results obtained by numerical methods correspond to the experimental measurements that were performed on the branch model.

5. Conclusions

Following conclusions can be given:

- 3D model of the pipe branch was analyzed with finite element method. This allowed locating critical spots on the branch from the stress concentration point of view.

- Experimental measurements, conducted by the strain gauges, were compared to the numerical calculations. Locations with the greatest stress concentrations were determined. Numerical and experimental methods confirmed that plastic deformation would not occur on the pipe branch in the maximum regime of the hydropower's work.

- Numerical calculations of the branch can be compared with the numerical calculations of the branch model, and experimental results that were performed on the branch model.

The results presented in this paper could form the basis for future research. The fact that all tests on the branch can be replaced by tests on a branch model greatly facilitate future research and testing in the field of stress concentration, strains and deformations. Also, one of the aspects on which future research is based on that and all the other branches and critical points on the pipeline C3 in HP "Perucica" can be simulated in a similar manner. Through this work, among other things it is shown that whenever possible, especially in structures whose dimensions are large, the output should be sought in designing the model, which will faithfully reflect the behavior of the real object of research. Such a model, even analyzed through numerical methods, can be enough to pinpoint critical bands on which to focus in the research of the real object.

6. Literature

[1] Bajic, D.; Momcilovic, N.; Maneski, T.; Balac, M.; Kozak, D.; Culafic, S.: Numerical and Experimental Determination of Stress Concetration Factor for a Pipe Branch Model

[2] Plancq, D; Berton, M.N. Limit Analysis Based on Elastic Compensation Method of Branch Pipe Tee Connection Under Internal Pressure and Out - of - Plane Moment Loading. // International Journal of Pressure Vessels and Piping, 75(1998), pp. 819- 825.

[3] Kim, Y.J; Lee, K.H.; Park, C.Y. Limit Load for Piping Branch Junctions Under Internal Pressure and In - Plane Bending - Extended Solutions. // International Journal of Pressure Vessels and Piping, 85(2008), pp. 360- 367.

[4] Mkrtchyan, L. Scha, H. Hofer, D. Stress Indices for Branch Connections with Arbitrary Branch -To-Run Angles,// Transactions, SmiRT/ New Delhi, India, 21. November 2011, pp. 1-8.

[5] Jovanovic, M.; Milenkovic, D.; Petrovic, G.; Milic, P.; Milanovic, S. Theoretical and Experimental Analysis of Dynamic Processes of Pipe Branch for Supply Water to the Pelton Turbine. // Thermal Science, vol. 16, (2012), pp. S617-S629.

ANALYTIC MODEL OF NON AXISSYMMETRIC DRAWING

Doctor of science engineering, professor Nazaryan E.A., PhD physics and mathematics science, assistant professor Arakelyan M.M, PhD student Simonyan A.S. – Yerevan State University, Armenia, enazaryan@ysu.am

АНАЛИТИЧЕСКАЯ МОДЕЛЬ ПРОЦЕССА НЕОСЕСИММЕТРИЧНОЙ ВЫТЯЖКИ

Доктор техн. наук, профессор Назарян Э.А., канд. физмат. наук, доцент Аракелян М.М., аспирант Симонян А.С. – Ереванский государственный университет, Армения, enazaryan@ysu.am

Abstract: *The analysis of stress-strain state non axis symmetric drawing process, which was developed based on an analytical model of the process. Obtained the dependencies for the components of the stress in the plastic region. The relationship between changes in the district velocity compressive stress on the peripheral area of the amount of shear stress. On this basis, it is given a numerical grade to increase the limit drawing ratio slightly different from equivalent value determined by the equality of the greatest meridional stress to the yield strength of the material at dangerous section of the blank.*

KEYWORDS: BOX-SHAPED PARTS; DRAWING; BISECTOR; LIMIT DRAWING RATIO.

1. Introduction

Among the processes of sheet metal forming nonaxisymmetric drawing it is one of the least studied that to some extent makes it difficult the development of science-based technology of manufacturing products such as thin-walled shells of various configurations. The main focus of researchers has been directed to solve the particular problem in order to explain the experimentally established fact increase the limit drawing ratio is 1.5-2 times at low single-purpose boxes drawn with relatively large corner rounding radii, compared with the drawing of cylindrical parts [1,2 and etc.].

Difficulties developing an analytical model non axis symmetric drawing process due to the fact that the corner of the blank along with the normal stresses acting with respect to the deforming tool in the meridional and circumferential directions, and shearing stresses occur, significantly complicating the process analysis.

In [3]offered one of the possible explanation for the increase limiting coefficient at drawing box shaped parts, based on the assumption that the growth of the absolute value of circumferential of compressive stresses acting on the bisector of the corner portion at the periphery of the blank. On the basis of this assumption is established, it is theoretically possible coefficient of the drawing box-shaped parts can not exceed the amount $K = R/r \Rightarrow \exp\left(1+1/\sqrt{3}\right) \approx 4{,}84$, where r - rounding radius in the mates of plane wall box parts, R -distance from the center of rounding to the blank edge along the bisector of the angle.

In this paper, which is a continuation of [3], the task of developing an analytical model of non axis symmetric drawing process and on this basis to establish the relationship between the value and the nature of the distribution of shear and normal stresses, which will justify an increase in the limiting coefficient, as a result of growth in absolute value circumferential compressive stresses on the peripheral part the blank.

2. Formulation of problem

Consider deformation of the flange elements at blank in non axis symmetric drawing. We select the median surface of the blank in a system of rectangular coordinates having an axis z extending in the thickness direction, the axis ρ extending in the meridional direction and an axis θ extending in the circumferential direction and perpendicular to the axes ρ and z .

As a origin of the coordinate ρ will take center the radius of rounding r , and the coordinates θ - the direction of the bisector.

It is believed that the original sheet blank with constant thickness is deformed in a plane stress [1]. In this case, stress $\sigma_z, \tau_{\rho z}, \tau_{\theta z}$ on the system selected coordinates are zero, and the components $\sigma_\rho, \sigma_\theta, \tau_{\rho\theta}$ are independent of the coordinates z .It is assumed that sheet blank thickness S is small compared with the transverse dimensions, whereby $\sigma_\rho, \sigma_\theta, \tau_{\rho\theta}$ is meant a value averaged over the thickness of the respective stress components.

Under these conditions, the differential equilibrium equations of the blank element of constant thickness and condition of Mises' yield (energy condition of plasticity) for plane stress are the form (Kachanov L. M. “Fundamentals of the Theory of Plasticity”. M. 1969, 420 p.)

$$\left.\begin{aligned} &\frac{\partial \sigma_\rho}{\partial \rho} + \frac{1}{\rho}\frac{\partial \tau_{\rho\theta}}{\partial \theta} + \frac{\sigma_\rho - \sigma_\theta}{\rho} = 0; \\ &\frac{\partial \tau_{\rho\theta}}{\partial \rho} + \frac{1}{\rho}\frac{\partial \sigma_\theta}{\partial \theta} + \frac{2\tau_{\rho\theta}}{\rho} = 0, \end{aligned}\right\} \qquad (1)$$

$$\sigma_\rho^2 - \sigma_\rho\sigma_\theta + \sigma_\theta^2 + 3\tau_{\rho\theta}^2 = \sigma_s^2 \ . \qquad (2)$$

The absence in scientific and technical literature of correct analytical solutions of the equations (1) and (2) allows certain schematization of forming process under non-axis symmetric drawing and use a number of assumptions.

As the basic assumptions, we assume that in the plastic region with dimensions $r \le \rho \le R; 0 \le \theta \le \pi/2$ increasing coordinates θ of the normal stresses are reduced and straight delimiting plastic and rigid (elastic) region at $\theta = \pi/2$ become equal to zero, and shear stresses are rising and, according to (2) on the border tightly - plastic areas receive the greatest possible value for plane stress $\tau_{\rho\theta} = \tau_{\max} = \pm\sigma_s/\sqrt{3}$.

In plane stress is realized three-dimensional strain state $\varepsilon_z \neq 0$ whereby the thickness of the sheet metal in the plastic region becomes a variable $s = s(\rho;\theta)$ .In the direction of the bisector of the corner region of symmetry condition follows that for $\theta = 0$; $\tau_{\rho\theta} = 0$ and the first equation (1) and the plasticity condition (2) are converted to the well-known equation in the case of a variable thickness of blank and take the form of:

$$\left.\begin{aligned} &\rho\frac{d\sigma_\rho}{d\rho} + \sigma_\rho\left(1 + \frac{\rho ds}{s d\rho}\right) - \sigma_\theta = 0; \\ &\sigma_\rho^2 - \sigma_\rho\sigma_\theta + \sigma_\theta^2 = \sigma_s^2. \end{aligned}\right\} . \qquad (3)$$

It should be noted that σ_ρ and σ_θ in (1),(2) are the current normal stresses, and in (3) – are the major.

From (3) it follows that the problem is statically indeterminate (there are two of the equation, but it is necessary to determine the three unknown functions- $\sigma_\rho, \sigma_\theta, s$), so for the analysis of stress-strain state becomes necessary to use constraint equations between stress and strain increments, as well as acceptable to use the results of analytical solutions obtained for axis symmetric drawing.

3. The analytical solution

In [4] the original equations of plastic flow theory in axial symmetry of deformation, namely the system of equations (3), the condition of constant volume and the constraint equation between stress and strain increments are given to a single structure and are presented in the deviatory plasticity cylinder plane Mises as a simple proportional relationship increments between meridional stress and equivalent strain $d\sigma_\rho = \sigma_s d\varepsilon_i$. This meridional and circumferential stresses acting along the main direction (along the bisector of the corner region), and satisfying the second equation (3), have the form [4]:

$$\left.\begin{aligned}\sigma_\rho &= \sigma_s \frac{2}{\sqrt{3}}\cos\left(\varphi+\frac{\pi}{6}\right);\\ \sigma_\theta &= -\sigma_s \frac{2}{\sqrt{3}}\sin\varphi\end{aligned}\right\}, \quad (4)$$

where φ - the angle strain state, changing in this issue within the limits $0 \le \varphi \le \pi/2$.

In [5] established the relationship between the angle of the type strain state and the relative coordinate in the main meridional direction $\rho/r = \exp\left[1-2/\sqrt{3}\times\cos\left(\varphi+\pi/6\right)\right]$ - (along the bisector of the corner zone). Because of this relationship for non-axis symmetric drawing shows that at $1 \le \rho/r \le 2{,}718$ implemented oppositely biaxial stress state $\left(\sigma_\rho\sigma_\theta \le 0;\ \sigma_\rho \ge 0;\ \sigma_\theta \le 0\right)$, and when $2{,}718 \le \rho/r \le 4{,}84$ the state of stress changes sign and becomes biaxial same name $\left(\sigma_\rho\sigma_\theta \ge 0;\ \sigma_\rho \le 0;\ \sigma_\theta \le 0\right)$ (Figure 1).

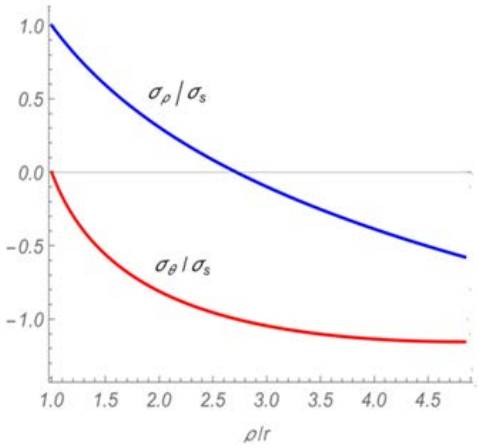


Figure 1. *The distribution of the main normal stresses along the bisector corner region at drawing of rectangular boxes*

According to the basic assumptions of the earlier represent the current value of the normal stress in the form of two factors

$$\left.\begin{aligned}\sigma_\rho &= \sigma_s \frac{2}{\sqrt{3}}\cos\left(\varphi+\frac{\pi}{6}\right)\times F(\theta);\\ \sigma_\theta &= -\sigma_s \frac{2}{\sqrt{3}}\sin\varphi\times F(\theta).\end{aligned}\right\} \quad (5)$$

The first factor in (5), according to (4), characterized by the distribution of the principal normal stresses along the bisector of the corner zone of blank, and the second - determines the nature of the reduction of the stress by increasing the polar angle within the limits $0 \le \theta \le \pi/2$.

It is obvious that in this problem should occur the following boundary conditions: in $\theta = 0;\ F(\theta) = 1$ and in $\theta = \pi/2;\ F(\theta) = 0$.

Under these boundary conditions of plasticity equation (2), taking into account (5)

$$\tau_{\rho\theta} = \pm\frac{\sigma_s}{\sqrt{3}}\left[1-F^2(\theta)\right]^{1/2}. \quad (6)$$

Adopted the basic allowance equivalent to the assumption of independence of the shear stress on the coordinate ρ, $\left(\partial\tau_{\rho\theta}/\partial\rho = 0\right)$, on the basis of which the second equation of equilibrium (1) takes the form:

$$\frac{d\sigma_\theta}{d\theta} + 2\tau_{\rho\theta} = 0. \quad (7)$$

From joint consideration of dependencies (6), (7) and (5) following the variation of the second factor in (5), $F(\theta) = \cos\theta$ on the basis of which the character tangential stress distribution in the plastic region, according to (6) is installed under the assumed boundary conditions, becomes $\tau_{\rho\theta} = \pm\sigma_s \cdot \sin\theta/\sqrt{3}$.

Thus, the stress component distribution in the plastic region have the form:

$$\left.\begin{aligned}\sigma_\rho &= \sigma_s \frac{2}{\sqrt{3}}\cos\left(\varphi+\frac{\pi}{6}\right)\times\cos\theta;\\ \sigma_\theta &= -\sigma_s \frac{2}{\sqrt{3}}\sin\varphi\times\cos\theta;\\ \tau_{\rho\theta} &= \pm\sigma_s \frac{1}{\sqrt{3}}\sin\theta.\end{aligned}\right\} \quad (8)$$

Obviously, according to (8), satisfying the condition of plasticity (2) taking into account accepted assumptions, and satisfy the system of differential equilibrium equations (1).

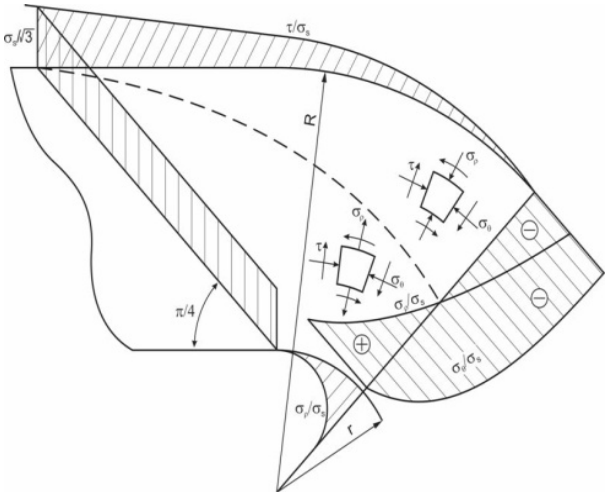


Figure 2. *The distribution of normal and shear stresses at the corner of non axis symmetric drawing (---- stress state type section line)*

On the basis of the established relationship between the value and nature of the distribution of tangential stresses and circuit (7) it is possible to study growth in absolute value circumferential compressive stress on the periphery of the blank. From this differential relationship it implies that the rate of change of circumferential stress on the corner is proportional to shear stress, according to which justified the increase in the limit of the coefficient of non-axis symmetric drawing compared with an drawing of cylindrical parts. To integrate this (7) in the appropriate range. From Figure 1, and the second relationship (4) shows that while changing the type of angle φ strain state within the limits $\pi/3 \le \varphi \le \pi/2$ growth circumferential compressive stress, the

relative coordinate ρ/r $(r=1)$ varies $e(2,72) \le \rho \le R$, and shear stress, respectively - $0 \le \theta \le \pi/2$.

Integrating (7) with (8) within the specified limits and making some transformations, we find that $R \approx 4,72$, slightly differs from the previously set value [3]. When receiving the said values further assumed that the resultant stressis applied to a circumferential center of the gap $R-e$, and this gap circumferential stresses are distributed evenly.

4. Conclusions

1. The analysis of stress-strain state of the corner of the blank in the absence of axial symmetry of the deformation, on the basis it is developed analytical model of non axis symmetric drawing.
2. The relationship between the rate of change of circumferential compressive stresses and the value of the shear stress at the periphery of the blank.
3. On the basis of this relationship, a numerical score to increase the limiting coefficient at drawing a rectangular box, which is equal to $R \approx 4,72$, only slightly different from a similar value set on an equal basis most of the meridional stress to the yield strength of the material in a dangerous section of the blank. [3].

5.Reference

1. **Popov E.A., Kovalev V.G., Shubin I.N.** Technology and automation of stamping. M .: Publishing House of the Bauman MSTU, 2000, 480 p.
2. **Forging and Stamping:** A Handbook in 4 volumes / ed. E.I.Semenova, Volume 4, Stamping. M .: Engineering, 2010, 544 p.
3. **Nazaryan E.A., Arakelyan M.M., Simonyan A.S.,** Analysis of the drawing process box parts // Blank production in mechanical engineering.2016, N 3. pp.18-21.
4. **Nazaryan E.A, Arakelyan M.M.,** The mechanics of forming the thin circular plates // Izv.NAN RA, Mechanics, 2009, v.65, N 4, pp.80-88.
5. **Nazaryan E.A, Arakelyan M.M., Simonyan A.S.,** Theoretical study of the quality parameters in the process of drawing cylindrical parts // Blank production in mechanical engineering, 2015, N 5. pp.24-30.

KINETIC DIAGRAMS OF FATIGUE DAMAGE IN FRACTURE MESOMECHANICS

MSc.Eng.GeorgyDobrev[1],Ass.Prof,PhD.AlexanderPopov[2]
[1]Institute of Metal Science - BAS, Sofia, Bulgaria,
[2]Institute of Mechanics - BAS, Sofia, Bulgaria
E-mail: dobrevbg@mail.bg, alpopov@abv.bg

Abstract : *The fatigue of metals is a relatively new part of mechanics of destruction. In modern theories to explain the destruction of a material of fatigue is considered that the process begins and flow the basis of generation and accumulation of micro-cracking in the material. To describe this process is by using kinetic diagrams of fatigue. The interest to the theory is a discussion of the process of fatigue of middle level. This article examined the kinetic diagrams of fatigue of middle level and evaluate their parameters by ultrasound measurements.*

KEY WORDS: *KINETIC DIAGRAMS, FRACTURE MESOMECHANICS, GRAIN SIZE), ULTRASONIC.*

Introduction

The fatigue of metals is a major cause of destruction of the parts and components of structures working under conditions of cyclic loading [1,2,3].
The destruction is related to the rise of the workpiece surface and distribution of one or more micro-cracks to total destruction.
The essential tool for studying the phenomenon of fatigue curves was introduced in 1870 by August Wöhler [1]. In the middle 1960-ies, it was found that these curves cannot explain the origin and development of micro-cracks in the process of fatigue. To solve this problem it is necessary to establish kinetic diagrams of fatigue fracture (KDFF), Figure 1 [1,2,3].

In this article is examined the dependence of the kinetics of micro-cracks of an average level of the average grain size. The article submit questions to obtain non-destructive evaluation in kinetic diagrams of fatigue.

1.Kinetic Diagrams in Fracture Mechanics

Kinetic diagram fatigue in the classical mechanics of destruction is given in Figure 1.

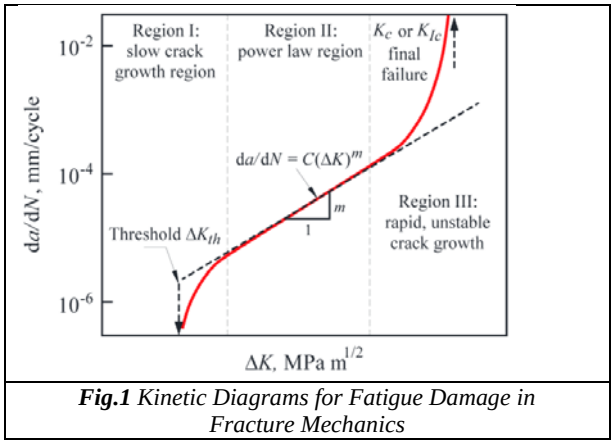


Fig.1 *Kinetic Diagrams for Fatigue Damage in Fracture Mechanics*

In [2] is offered a common form of kinetic diagram of fatigue.

$$(1) \quad \frac{da}{dN} = f[X,Y,Z]$$

where indications were introduced: - a length of micro-cracking, N - the number of cycles until the length of the micro-cracking - a, $X = X(\Delta K, K_{MAX}, K_{IC}, K_C, \Delta K_{th})$- afunction of variations of the stress intensity factor (ΔK)- interval, (K_{MAX})-maximum, (K_{IC}, K_C)- critical values of the coefficients of intensity of flat strain state and flat stressed state, (ΔK_{th})-threshold stress intensity factor, $Y = Y(E, \nu, \sigma_S, \sigma_B, \varepsilon_P, m)$- function of the modules of elasticity-(E, ν), mechanical properties-(σ_S, σ_B)- yeld strength and breaking strength, (ε_P)- plasticity of deformation , plasticity degree of hardening-(m), $Z = Z(\overline{D}, r_P^*, ...)$- function of structural parameters: $\overline{D}$- the average value of the grain size, r_P^* - size of the plastic zone at the crack. For design, the most commonly used of the simplified (1) according to (2): [2],

$$(2) \quad \frac{da}{dN} = A_0.[\Delta K]^{m_0}$$

where constants: (A_0, m_0) is determined experimentally.

2.Kinetic Diagrams in Fracture Mezomechanics

The literature reveals a number of patterns, particular cases of (1). Here are considered the following models:

A/ Matvienko's model [3]

$$(3) \quad \frac{da}{dN} = C_M [r_P^*]^{m_M}$$

where for flat strain state r_P^*- size of plastic zone in front of cracks, Fig.2., constants C_M, m_M is determined experimentally.

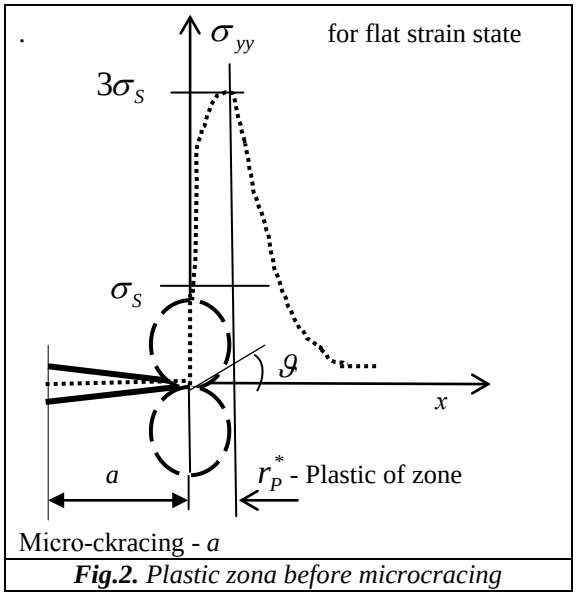


Fig.2. *Plastic zona before microcracing*

For plastic zone at the tip of the crack were obtained relations [3] at the flat strain state - r_P^* and in flat stressed state - r_P^{**}

$$(4)\quad r_P^* = \frac{(1-2\nu)^2}{\pi}\left(\frac{K_{IC}}{\sigma_S}\right)^2;\ r_P^{**} = \frac{1}{2.\pi}\left(\frac{K_C}{\sigma_S}\right)^2;$$

B) Paris's model [2], for flat strain state

$$(5)\quad \frac{da}{dN} = C_H\left[K_{IC}\right]^{m_H}$$

Constants C_H, m_H is determined experimentally. In the fracture mechanics was received that [2]

$$(6)\quad K_I(a) = Y(h;b)\sigma\sqrt{\pi.a};$$

for flat strain state, if $\sigma \to \max$, then
$K_I(a) \to K_{\max}(a) \equiv K_{\max} \sim K_{IC}$.
The relationship $K_{IC} = K_{IC}\left(\overline{D};\tau_S;E;\nu;\psi\right)$ is determined by [4]

$$(7)\quad \left(K_{IC}^T\right)^2 = \rho\left(\overline{D};...\right)\tau_S\frac{E}{1-\nu^2}\ln\left(\frac{1}{1-\psi}\right)$$

where $\rho\left(\overline{D};...\right)$ is a function of structural parameter $\overline{D}$ (average grain size) , τ_S - tangential component of the limit of plasticity (E,ν) are modulus of elasticity, ψ - relatively contraction. Simplification of dependence (7):

A/ As $\psi < 1$ then $\ln\left(\frac{1}{1-\psi}\right) \approx \psi + \frac{1}{2}\psi^2 + ... \approx \psi$

B/ The condition of Misses's plasticity $\tau_S = \frac{1}{\sqrt{3}}\sigma_S$

consequently

$$(8)\quad \left(K_{IC}\right)^2 \approx \rho\left(\overline{D};...\right)\frac{\sqrt{3}}{3}\sigma_S\frac{E}{1-\nu^2}\psi$$

C/ Equation for ψ in (8) . In [5] given that steel brands 45,40X.. in order equation may be considered:

$$(9)\quad \left[\frac{\psi}{0.002+\frac{\sigma_S}{E}}\right]^{\frac{1}{5}} = \left[\left(\frac{\sigma_B}{\sigma_S}\right)\left(1+\frac{7}{5}\psi\right)\right]^{\frac{3}{4}}$$

After the improvements needed transformations is obtained the simplified form of an equation ψ .

$$(10)\quad A.\psi^n - B.\psi - C \approx 0$$

where $n = 4/15$,

$$A = \left(\frac{2}{1000}+\frac{\sigma_S}{E}\right)^{-4/15},\ C = \left(\frac{\sigma_B}{\sigma_S}\right),\ B = \frac{7}{5}\left(\frac{\sigma_B}{\sigma_S}\right),$$

$$\sigma_S = \sigma_S(V_L;V_T),\ \sigma_B = \sigma_B(V_L;V_T),\ E = E(V_L;V_T)$$

Equation (10) is non-linear and are decide to method of bisection /Newton's method/ by means algorithm ZEROIN. This algorithm, ranging in 2-3 iterations is sustainable and rapidly converging.

C/ Disable of $\rho\left(\overline{D};...\right)$ from (8) . By way of example , for examine of dependence (8) by references, etc. $(.)^{REF}$, of participating in it values

$$(11)\quad \left(K_{IC}^{REF}\right)^2 \approx \rho\ \sigma_S^{REF}\frac{E^{REF}}{1-\left(\nu^{REF}\right)^2}\psi^{REF}\ ;$$

If it are divide (9) of (11), then

$$(12)\quad \left(\frac{K_{IC}\left(\overline{D}\right)}{K_{IC}^{REF}}\right)^2 \approx \frac{\sigma_S\left(\overline{D}\right)}{\sigma_S^{REF}}.\xi\left(V_L;V_T\right);$$

where it is assumed that $\rho = \rho\left(\overline{D}\right) = Const$,
$\xi\left(V_L;V_T\right) \equiv \xi\left(E;\nu;\psi\right)$,

$$\xi(E;\nu;\psi)=\frac{E}{E^{REF}}\cdot\left(\frac{1-\nu^2}{1-\left(\nu^{REF}\right)^2}\right)^{-1}\cdot\frac{\psi}{\psi^{REF}}\cdot$$

After taking into account the dependence of the Hall-Peth [6]

$\sigma_S\left(\overline{D}\right)=\sigma_0+K_y.\left(\overline{D}\right)^{-1/2}$, then

$$(13)\quad K_{IC}^{*}\approx b_0^{K_{IC}}+K_y^{K_{IC}}.\left(\overline{D}\right)^{-1/2}$$

where $\left[\frac{4.\pi^2}{1125}\frac{V_T^4}{V_L^3}\left(\frac{2}{V_L^5}+\frac{3}{V_T^5}\right).f^4\right]\left(\overline{D}\right)^3$ -α_L =0; $K_{IC}^{*}=\left(\frac{K_{IC}\left(\overline{D}\right)}{K_{IC}^{REF}}\right)^2=K_{IC}^{*}\left(\overline{D}\right)=K_{IC}^{*}\left(V_L;V_T;\alpha_L\right)$, [7]

$\left(V_L;V_T;\alpha_L\right)$ are velocities of longitudinal and transverse waves and attenuation propagation of ultrasound. Methods for measuring the acoustic properties $\left(V_L;V_T;\alpha_L\right)$ are given in ASTM E 494:2010,

$$b_0^{K_{IC}}=b_0^{K_{IC}}\left(V_L;V_T\right)=\frac{\sigma_0}{\sigma_S^{REF}}.\xi\left(V_L;V_T\right),$$

$$K_y^{K_{IC}}=K_y^{K_{IC}}\left(V_L;V_T\right)=\frac{K_y}{\sigma_S^{REF}}.\xi\left(V_L;V_T\right).$$

It is seen that (13), with all its conventions, is an analogue of the dependence of the Hall-Petch.

Clearly, implicitly dependence (13) may be written as where $\left(K_{IC}^{REF};\sigma_S^{REF};\sigma_0;K_y\right)$ - is a vector with known constants.

The relationship $r_P^{*}\left(\overline{D}\right)$ according to (4) is for flat strain state

$$(14)\quad r_P^{*}\left(\overline{D}\right)\approx\frac{(1-2\nu)^2}{\pi}\left(\frac{K_{IC}\left(\overline{D},V_L,V_T,\sigma_S\left(\overline{D}\right)\right)}{\sigma_S\left(\overline{D}\right)}\right)^2$$

3. Models of Kinetic Diagrams for Fatigue Damage in Fracture Mesomechanics

a/ In mesomechanics the Matvienko's model is

$$(15)\quad \frac{da}{dN}=C_M\left[r_P^{*}\left(\overline{D};V_L;V_T\right)\right]^{m_M}$$

The relationship $r_P^{*}\left(\overline{D}\right)$, taking into account the dependence of the Hall-Petch is determined it for flat strain state by dependence (14).

b/ In mesomechanics the Paris's model is

$$(16)\quad \frac{da}{dN}\approx C_M\left[K_{IC}\left(\overline{D};V_L;V_T\right)\right]^{m_M}$$

The value of K_{IC} is defined by (13), i.e., from

$K_{IC}=K_{IC}\left(\overline{D};V_L;V_T\right)$

4. Inverse Problem of Kinetic Diagrams for Fatigue Damage in Fracture Mesomechanics

The follow problems are fomulate:

A / Direct problem: If constants $\left(C_M;m_M\right)$ are known, then the function $a=a(N_1)$ is calculate.

B / Inverse Problem: If the values $\left(a;N_1;\overline{D}\right)$ are known, then the constants $\left(C_M;m_M\right)$ are evaluation. The solution of (2) is

$$(17)\quad N_1\approx\int_{a_{j-1}}^{a_j}\frac{da}{C_M\left[r_p^{*}\left(\overline{D}\right)\right]^{m_M}};\ j=1,2,3,...,a/\overline{D}$$

The equation (17) can write as Fredholm's integral equation firs kind

$$(18)\quad N_1\approx\int_{a_{j-1}}^{a_j}1.\xi(a).da\ ;\ j=1,2,3,...,a/\overline{D}$$

where $\xi(a)=\left\{C_M\left[r_P^{*}\left(\overline{D}\right)\right]^{m_M}\right\}^{-1}$; $a=a\left(\overline{D}\right)$. There for the equation for the parameter m_M is

$$(19)\quad \left[r_P^{*}\left(V_L;V_T;\alpha_L\right)\right]^{m_M}-\left[C_0.\zeta\left(N_1\right)\right]^{-1}=0$$

where $\zeta(N_1)\equiv\xi(a)$- unknown function, compute by means (18), $C_0=C_M\big|_{a\to 0}$.

5. Conclusion

a/ In the terms of mesomechanics the KDFF for Matvienko's model and Paris's model are obtain

$$(20)\quad \frac{da}{dN}\approx C_M\left[r_P^{*}\left(\overline{D}\right)\right]^{m_M};$$

$$(21)\quad \frac{da}{dN}\approx A_V.\left[K_{IC}\left(\overline{D}\right)\right]^{m_V};$$

where $r_P^{*}\left(\overline{D}\right)\approx r_P^{*}\left(\overline{D};V_L;V_T\right)$, $K_{IC}=K_{IC}\left(\overline{D};V_L;V_T\right)$ and $\overline{D}=\overline{D}\left(V_L;V_T;\alpha_L\right)$.

b/ The inverse problem for Matvienko's model is formulated. The equation for parameter m_M (19) is obtained. If $\left(V_L;V_T;\overline{D};N_1\right)$ are known, then m_M is calculate i.e.

$$(22)\quad \left\{\left(V_L;V_T;\alpha_L\right),N_1\right\}\Rightarrow m_M.$$

Reference

1. Terentev B.F., Fatigue of metallic materials, Nauka, Moscow, 2003.
2. Hellan K., Introduction to Fracture Mechanics, Mir, Moscow, 1988.
3. Matvienko Yu. G., Models and criteria in fracture mechanics, Fizmatlit, Moscow, 2006.
4. Andreykiv A.E., Theory of Cracks Problems in 3D, Naukova Dumka, Kiev, 1982.
5. Morozov & , Fracture Mechanics, Mir, Moscow, 1988.
6. Trefilov V.I Hardening and damage polycristalline metals, Edd by. Naukova Dumka, Kiev, 1987.
7. Popov A.P., NDE of mechanical properties of Fe-C alloys, No3, Institute of Mechanics – BAS, 2013.

URBAN TRANSPORT PLANNING AS A SUPPORT TO AIR POLLUTION CONTROL

assistant professor dr. Angelevska B., full professor dr. Atanasova V.
Faculty of Technical Sciences, University "St. Kliment Ohridski" Bitola, Macedonia
beti.angelevska@tfb.uklo.edu.mk, vaska.atanasova@tfb.uklo.edu.mk

Abstract: *A significant part of air pollution control strategy can be achieved through measures in urban transport planning. The need for this analysis is based on the fact that transport planning decisions are often made without proper consideration of their air pollution consequences [1]. This inevitably deteriorates air quality in urban areas, particularly in those areas which already have problem with urban air pollution. The paper deals with transport planning approach towards reducing air pollution and this approach is analyzed through short-term and long-term measures, recommended for Bitola. Implementation of these measures has a potential to contribute for improvement of the current problem with air pollution.*
***KEYWORDS**: TRANSPORT PLANNING, MEASURES, AIR POLLUTION, BITOLA*

1. Introduction

Urban transport is a source of wide range of environmental issues like air pollution, noise, acidification and global warming. Air pollutant concentrations caused by urban transport, accumulated along high-volume freeways and arterials are widely recognized as severe health hazards [1].

Under circumstances where the effective control of vehicle air pollution immediately at the source is not technologically or economically feasible, the emphasis should be placed on an improved traffic management program and better transport planning and design. It is important that a transport decision be made not only on the basis of cost savings, increased safety, and improved traffic performance, but also on such aspects as reduced energy requirements and improved quality of environment [2].

The role of transport planner should be concerned that the transport plan, design and operational alternatives selected are sensitive to air quality criteria [1].

Among all the measures available to the transport planner, several of them which offer a number of possibilities, individually or in a combination, are included in this analysis for Bitola. Depending on how it is applied, transport planning can improve air quality in the short and long run by strategic measures, encouraging minimization of pollution emissions. Activities in these short- and long- term measures are further sub-categorized as follows: planned unit development, regulation & pricing policy, planning of urban journeys and monitoring and forecasting. Presented in this way, they offer a significant direction towards the surpassing the current air pollution problem in Bitola.

2. Transport and environmental impacts

Transport plays a key role in affecting air quality and environmental degradation. The delays and frustrations caused by urban traffic congestion can reduce human productivity and quality of life, thus possibly reducing the potential gross domestic product. The noise produced by various types of vehicles raises the level of ambient noise, increases stress and reduces the quality of life. Transport can also contribute to the physical and social isolation of certain vulnerable segments of society, such as the poor, children and the elderly [3]. Both short- and long- term exposure to air pollutants can affect people's health. Hence, air pollution causes significant harm to health and the environment and, as a result, has an adverse impact on the economy [4].

Air pollution control should not be the only important and current priority in the local context, having also a significant potential to control greenhouse gas emissions [5]. Climate change is one of the most important issues on the world agenda; while national governments reached an agreement in Paris in December 2015 on limiting climate change, regional and local government – along with a wide range of public and private sector organizations – have a responsibility to tackle carbon emissions [4].

The contribution from motor vehicles in urban air pollution in Bitola is significant. The economic situation in the town of Bitola and in the country in general defines the average age of the urban vehicle fleet. Therefore, the biggest part of the vehicles - around 47% (approximately 10.000 vehicles) are older, ranging from 14-20 years and above 20 years [6]. At the same time, exhaust emissions from these vehicles are higher, caused by obsolete technical characteristic and out-of date equipment for exhaust gasses treatment (or its total absence). Being frequently used on everyday level, these vehicles realize significant part of passenger kilometers in the town [6].

The amount of air pollution generated by urban transport depends not only on the type of vehicles, but also on the length, speed and number of motorized trips [7]. Hence this effort to emphasize the importance of transport planning contributing in that way for the direct control of urban air pollution.

3. Transport planning and air quality

In dealing with air pollution at both local and regional level, it is important to recognize the significance of transport in urban planning [1].

Transport planning should be considered in conjunction with urban planning, since each of them have a significant contribution in reducing air pollution and its harmful effects.

The role of urban planning is to manage the spatial organization for efficient allocation of urban infrastructure and land use [7]. Urban plans that locate jobs, housing, and recreation in close proximity increase the use of alternative forms of travel, such as walking, biking and mass transit. Alternative forms of travel reduce the number of vehicles on the road, reduce the amount of pollution emitted by vehicles, and improve air quality [7].

This means that air pollution consideration should be incorporated and evaluated in the process of developing land use and transport plans [1]. When needed, research should be conducted and supported in order to better understand current ambient air quality and pollution sources. Also, encouragement should be given for new legislation which would allow urban planning programs and pollution control programs to better meet air pollution abatement goals [1].

The treatment of the air pollution problem through urban and transport planning is a complex process, as illustrated in figure 1 below.

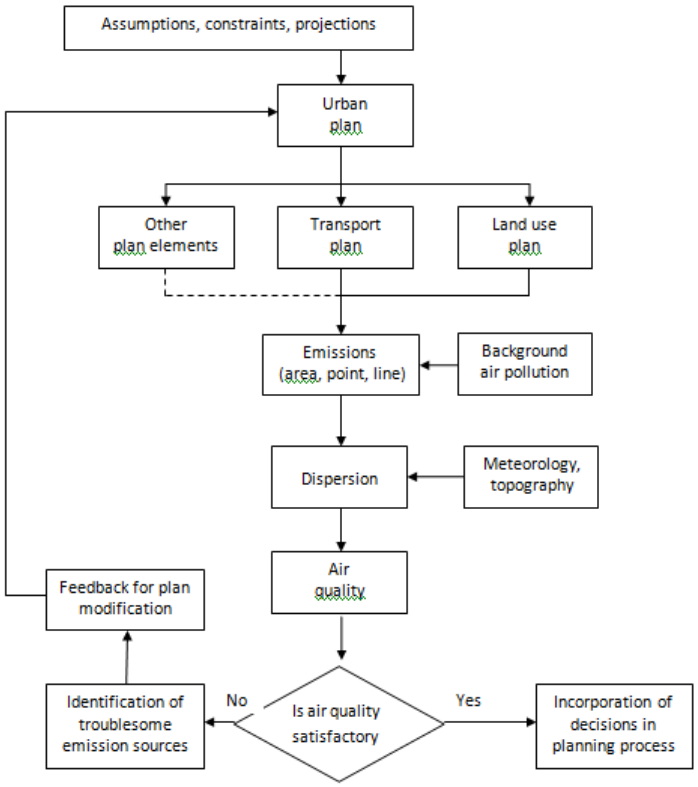


Fig. 1: *Air quality considerations in the planning process*
Source: [1]

However, there aren't easy answers for the urban and transport planners: many actions that will be beneficial will also have harmful effects [1]. For example, increasing the average speed of traffic will reduce the concentrations of hydrocarbons and carbon monoxide, but probably increase the concentration of nitrogen oxides. Increased travel speed also tends to lengthen trips; thus resulting in increased use of vehicles. Decreasing the density of land development reduces concentrations of air pollution but increases dependence of the vehicle as a transportation mode. Such trade-offs require close study in light of each urban area's unique conditions and priorities [1].

3.1. Strategic approach in transport planning for emission reduction

The development of a strategy involves the selection and categorization of a coherent set of measures which, taken together, will reduce the emissions of transport pollutants [3].

There are a number of feasible transport measures which may have varying levels of environmental impact [1].

Both long-range and short-term measures can be undertaken to improve the air quality in urban areas [2]. Long-range planning actions involving proper arrangement of land uses will ensure desirable allocation of urban activities. Within the framework of area wide land-use planning, effective measures can be taken in laying out streets and buildings properly so that the air pollution effects can be minimized. Long-range, land-use-transport planning will also make it possible to develop transport systems in which the amount of vehicular travel as well as the lengths of trips can be reduced considerably and thus limit air pollution effects [2].

In addition to long-range measures, which can be applied only in case of new developments and in case of implemented air quality management system, several short-term measures can be undertaken in existing urban areas in order to improve the air quality [2]. These short-term measures can be undertaken to reduce the amount of traffic in an urban street network, in addition to the measures directed to improving the quality of traffic flow.

In table 1 is listed a series of measures that can be undertaken in order to minimize the effect of traffic-generated emissions [2], [8]. As measures for both short- and long-term transport planning, design and operation for the purpose of air pollution control, the following measures can be included:

Table 1: Long- and short- term measures in transport planning

		Outcome					
Long-term measures	**Type of measure**	reducing need to make trip	reducing length trip	promote non-motorized transport	promoting public transport	shift trips from congested locations	reduce traffic/ traveler delays
	1. Urban and development planning.	✓	✓	✓	✓		
	2. Advice and warnings for the public and people at particular risk.	✓		✓	✓	✓	
Short-term measures	3. Traffic management and enforcement, and financial incentives and disincentives.	✓	✓	✓	✓	✓	✓
	4. Initiatives providing information, advice and education.	✓		✓	✓	✓	

It may be noted that, in general, that measures which are associated with effective regulation are more likely to accomplish the desired results than the changes in urban transport pricing policy or other measures [2].

3.2. Measures and their activities: summary tables

All these long- and short- term measures are further sub-categorized in additional 4 categories:

1. planned unit development,
2. regulation & pricing policy
3. planning of urban journeys
4. monitoring, information and forecasting.

This sub-categorization is given in summary tables (2-5), where every measure is presented with several activities defining that measure [8].

Hence, a brief explanation of every of the measure from the table 1 together with its activities is given in the following summary tables.

Table 2: Planned unit development

Urban and development planning
- Land use planning, development control and planning decisions, urban space and building design, improved network configuration.
- Incorporation of sustainable transport principles into the urban design of new settlements.
- Developing multimodal transport infrastructure to support low emission modes of transport: o public transport routes and services, including developing bus lanes, improving service quality and cost reduction o cycle routes and pedestrian areas o park & ride facilities**.**
- Reducing travel demand.

Table 3: Regulation/pricing policy

Traffic management and enforcement, and financial incentives and disincentives
- Traffic management systems and signal coordination: o road signs, traffic signals and road markings o lane control o traffic calming measures o vehicle bans or restrictions o elements of routes (such as positioning of traffic lights) o roadside emission testing.
- Zoning, including low emission zones: o congestion charging o cordons or zones o distance-based charging o speed management zones o clear zones (vehicle free zones) o time-based charging o toll road charging.
- Parking restrictions and charges: o restricted parking zones (including low emission vehicles and electric vehicle recharging points) o higher parking charges.
- Vehicle 'idling' restriction and charges including waiting and loading restrictions.
- Charges of fuel, engine size, vehicle registration, emission taxes.
- Taxi licensing – standardization of the minimum emission requirements for taxis.

Table 4: Planning of urban journeys

Initiatives providing information, advice, education or to develop skills for:
- Travel planning (awareness raising and education to encourage people to use alternatives to a car).
- Settings-based travel planning (such as in workplaces, new residential developments or schools): o traffic-free routes and route design to reduce exposure o improved facilities to **encourage cycling or other non-**motorized travel o cycle-to-work schemes o policies relating to b**usiness travel, including using** public transport rather than driving, or incentives for businesses to promote cycling at work o management of deliveries and products to minimize air pollution o signage and cycle parking o lighting and planting.
- Personalized travel planning to provide individuals with information, education, incentives and motivation to support low emission travel choices.
- Information, education and training on driving styles, including the need to avoid heavy acceleration and minimize braking and excessive speed.

Table 5: Monitoring, information and forecasting

Advice and warnings for the public and people at particular risk:
- Air pollution forecasts and real time data.
- Air quality monitoring database.
- Air pollution early warning alerts via text or email.
- Air pollution early warning or monitoring information via web- or app- based geographical systems.

Implementation of these measures is often difficult. Yet, the difficulty barriers should be considered as motivation for their choice and support.

4. Conclusion

Transport planning should be used as a support for the development of urban pollution control programs. Its major contribution lies in evaluating, proposing and implementing measures which help disperse pollutant concentrations, reduce exposure to pollutants and improve efficiency of urban travel [1]. Decisions from transport planners can limit negative impacts from transport upon the environment and contribute for better life quality.

The quality of urban air can be improved through implementation of short- and long-term measures for transport planning [2]. Short-term measures have potential not only to minimize traffic congestion and delays and thus reduce stop-and-go operation which is responsible for a large part of vehicle emissions; at the same time, these measures reduce the traffic volume on the network, inducing less usage of the vehicles through effective traffic regulation, efficient pricing policy, and improved planning of urban journeys. This is further supported by initiatives providing information, advice and education. On the other side, long-range measures related to area wide population, as public warnings and also careful planning of building arrangements and street layout will add to the overall reduction of the adverse effects of vehicle-related air pollution in urban areas [2].

The effective implementation of these recommended measures for Bitola can be of significant benefit in terms of improved traffic flow, support of non-motorized travel and thus reduced air pollution from vehicle emissions. For their success, cooperation is needed between transport and urban planners, supported by local authorities and by the public. Although the rate of the changes could be slow, the most important is that this analysis gives the starting point in transport needed for dealing with the problem of urban air pollution.

References

[1]. Voorhees, A., Ryckman, E. A guide for reducing air pollution through urban planning, Publication No. APTD-0937, Environmental protection agency, Office of air and water programs, Office of air quality planning and standards, North Carolina, 1973, USA, p.115.

[2]. Sinha, C. K. Air pollution considerations in traffic planning and engineering, pp. 159-172.

[3]. Gorham, R. Air pollution from ground transportation – an assessment of causes, strategies and tactics and proposed actions for the international community, The global initiative on transport emissions, United Nations, 2002, p. 194.

[4]. Greater Manchester combined authority. Greater Manchester low-emission strategy and air quality action plan - Public consultation, Transport for Greater Manchester, 2016, p. 116.

[5]. Institute for global environmental strategies. Air pollution control in the transportation sector, Third phase research report of the urban environmental management project, 2007, Japan, p. 392.

[6]. Angelevska, B., Markoski, A. Calculation of urban transport emissions: a case study for the town of Bitola, 31st Conference on transportation systems with international participation – Automation in transportation, KoREMA, Pula/Croatia-Milano/Italy, November 15-20, 2011, proceedings pp.7-12.

[7]. The World bank ESMAP Program. Urban air pollution, South Asia urban air quality management briefing note No. 6, 2002, p.4.

[8]. National institute for health and care excellence, Guideline scope, Air pollution: outdoor air quality and health, pp. 12. https://www.nice.org.uk/guidance/gid-phg92/resources/air-pollution-outdoor-air-quality-and-health-draft-scope-for-consultation2

SiC(p) REINFORCED ALUMINUM MATRIX COMPOSITES OBTAINED BY HOT PRESSING AND THEIR MECHANICAL PROPERTIES

Aynur Kazaz[1], H. Erdem Çamurlu[2], M. Ayşe Dere[2], K. Egemen Kuyucu[2]
Akdeniz University, Faculty of Engineering, Civil Engineering Department, 07058, Antalya, Turkey [1]
Akdeniz University, Faculty of Engineering, Mechanical Engineering Department, 07058 Antalya, Turkey [2]

erdemcamurlu@mail.com

Abstract: *Metal matrix composites, containing Al (4 wt. % Cu) as the matrix material and SiC particles as the reinforcement, were produced by hot pressing. SiC(p) content of the composites were in 10 – 50 vol. % range. Appropriate amounts of Al, Cu and SiC powder were dry mixed and pressed at 25 MPa at 525 and 550 °C. Obtained composites were subjected to density and hardness measurements, 3 point bending tests and optical microscope investigations. Hardness was seen to increase continuously with the increase in the amount of SiC(p) from 54 HB10 (unreinforced matrix) to 148 HB10 (50 vol. % SiC). On the other hand, bending strength values of the composites first showed an increase up to 20 vol. % SiC and then decreased. Strain values decreased considerably, with the addition of SiC into the unreinforced matrix and the composites containing 40 and 50 vol. % SiC did not show plastic deformation before fracture. Yield strength and elastic moduli of the composites increased with the increase in the SiC amount. It was seen that the properties of Al%4Cu-SiC(p) composites, such as strength and hardness, can be adjusted by varying their SiC contents.*

Keywords: SiC(p) reinforced Al composite, hot pressing

1. Introduction

Metal matrix composites (MMCs) are technologically important materials since they can be tailored for obtaining a desired property, in order to be utilized in a specific application. The change in the properties can be imparted through varying the reinforcement amount, size or shape or the properties of the matrix metal. Particulate reinforced metal matrix composites have the advantage of ease in production, as compared to continuously reinforced composites.

Light and low strength metals such as aluminum and magnesium have been widely used as the matrix material for particulate reinforced MMCs. Widely used reinforcement particles are Al_2O_3, TiC, SiC and B_4C [1]. The main advantage of utilizing these hard ceramic particles is to enhance hardness and wear resistance. Al MMCs reinforced with hard ceramic particles can be utilized in bushes, automotive, train and aircraft brake parts, pistons for internal combustion engines, etc [2].

Aluminum matrix composites reinforced with SiC particles can be produced by melting techniques, such as infiltration, stir and/or squeeze casting [3], and solid state techniques such as powder metallurgy (PM) methods. In PM, extrusion [4,5] and hot pressing are commonly utilized. PM presents crucial advantages over liquid state techniques such as eliminating the wettability issues and possibility of addition of high fraction of reinforcements [1]. In the study of Abarghouie et al. [4], Al 2024 alloy powder was mixed with SiC particles and cold pressed and then hot extruded at 495 °C. Solution heat treatment was also performed at 495 °C and aging at 191 °C. It was reported that presence of SiC particles accelerated aging kinetics, when properly solutionized. In the study of Chawla et al. [5], effects of SiC content and particle size were examined, specifically on the fatigue behavior of the MMCs containing Al 2080 matrix. It was reported that decreasing SiC particle size and increasing its amount resulted in an increase in fatigue strength. Şahin [3] prepared 2014 Al-SiCp composites through stir-squeeze casting and investigated their machining characteristics.

Due to their lightweight, high hardness and wear resistance, SiC reinforced Al MMCs are promising structural materials. In addition, powder metallurgy routes are seen to be advantageous in their production. Therefore, in the present study, SiC particulate reinforced Al matrix composites were produced via powder metallurgy, specifically by hot pressing. Obtained composites were characterized by microstructural examinations, hardness measurements and 3 point bending tests.

2. Experimental Procedure

Aluminum (Merck, average particle size <10 microns) and copper (Alfa Aesar, average particle size 1-3 microns) powders were mixed at 4 wt% Cu ratio. SiC powder (Alfa Aesar, average particle size <10 microns) was added at amounts corresponding to 10-50 vol. % of the composite. The powders were mixed with 2 mm zirconia balls in a ceramic vial for 15 minutes. Then the powders were screened and placed into a die, which was made of hot work tool steel (AISI H13). The die, with its contents was placed into a hot press (MSE Technologies) and 50 MPa pressure was applied in cold state. The furnace of the hot press was adjusted so that it presented a heating rate of 5 °C/min. A 30 min soaking period was applied to the die at 525 and 550 °C. During heating and soaking, 25 MPa pressure was maintained. The obtained hot pressed samples were 37 mm long, 12 mm wide and 6 mm thick.

3 point bending tests were conducted according to ISO 3325 standard (span length is 25 mm), with a 50 kN capacity Universal Shimadzu unit. Hardness measurements were conducted according to Brinell 10 (HB10) scale (Bulut Makina, Turkey). Densities of the samples were determined according to Archimedes' principle, after weighing the samples in air and in water. Samples were cut, lapped on emery paper and polished with diamond paste, prior to microstructural examinations. Microstructures of the composites were investigated by an optical microscope (Nicon Eclipse LV150).

3. Results and Discussion

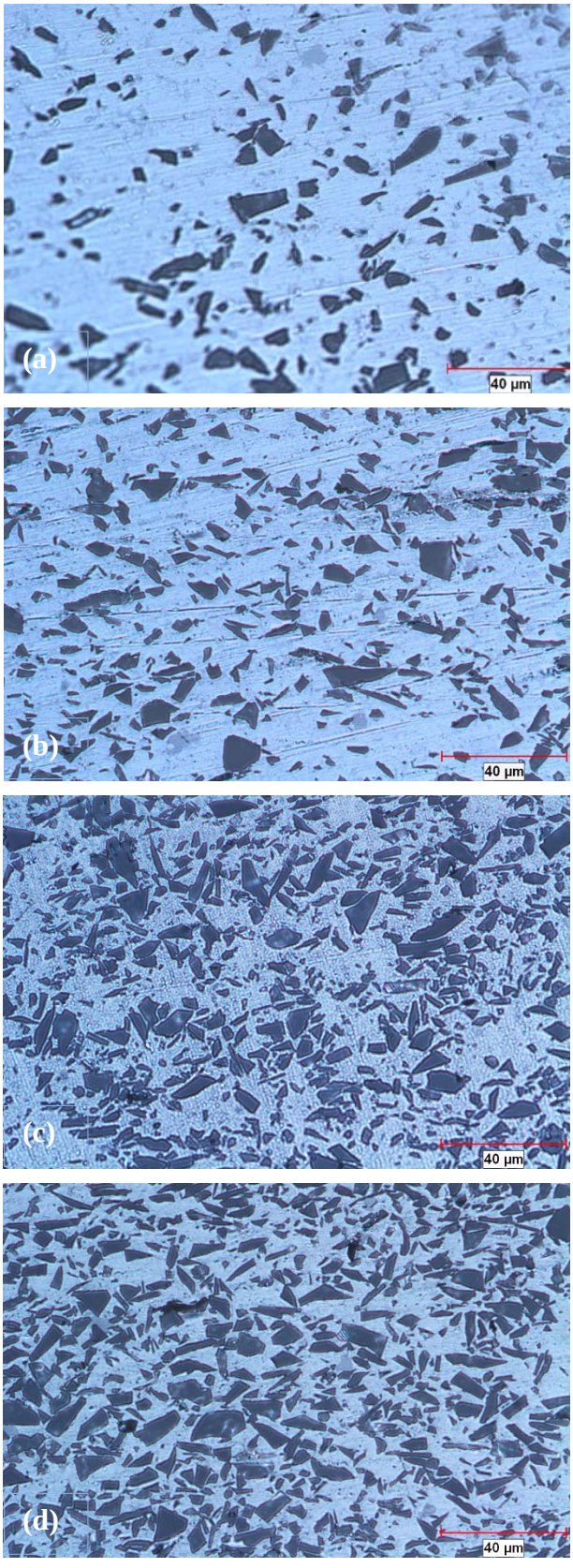
3.1. Microstructure of the Composites

Percent theoretical density values of the prepared composites were determined via dividing the measured density values by the theoretical density values of the composites and multiplying by 100. Percent theoretical densities of the composites hot pressed ad 525 °C were in 93.5 - 96.3 % range, whereas that of the composites hot pressed at 550 °C were in 94 - 99.6 % range.

The microstructure of the obtained SiC – Al(%4Cu) MMCs are presented in Fig.1 (optical microscopy, X500 magnification). In general, it was seen during the microscopical examinations that the composites obtained at 525 °C contained more amount of porosity than the composites obtained at 550 °C. This finding is in accord with the density measurements. The black angular particles in the given micrographs in Fig.1 are SiC. It can be seen in these micrographs that the area covered by the SiC particles increases with increasing SiC content of the composites. The SiC particles were seen to be homogenously distributed in the Al(%4Cu) matrix.

As can be seen in these figures, the particle size of SiC was generally smaller than 10 micrometers. However, there are some large particles of about 20 micrometers size.

In the optical micrographs, light gray particles were observed at some points, which are believed to be Al_2Cu intermetallic particles. These particles are believed to form with the reaction of Al and Cu during the liquid phase sintering of the Al-%4Cu system. At the sintering temperature, Cu has higher solubility in the formed liquid and upon solidification, formation of solid Al_2Cu particles takes place, since Cu has low solubility in solid Al at room temperature.



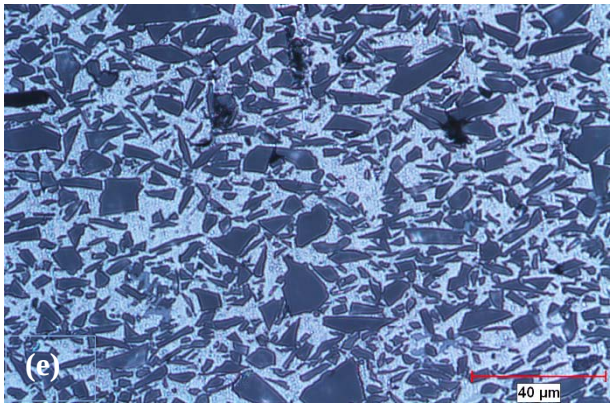


Fig. 1 *Microstructures of composites obtained by hot pressing at 550 °C of Al(%4Cu)-SiC mixtures containing (a) 10 vol. % SiC, (b) 20 vol. % SiC, (c) 30 vol. % SiC, (d) 40 vol. % SiC, (e) 50 vol. % SiC.*

3.2. Hardness of the Composites

Hardness of the unreinforced Al%4Cu matrix alloy was 54 HB10. Addition of SiC particles into the aluminum alloy matrix resulted in an increase in the hardness values. It can be seen in Fig. 2 that the hardness of the composites increased continuously with the increase in the amount of SiC(p) in the composites. Hardness of the composite which contained 50 vol. % SiC was 146 HB10.

Increase in the hardness of the composites with increasing SiC particle content may be attributed to restriction of the plastic deformation of the aluminum alloy matrix, due to the presence of the SiC particles.

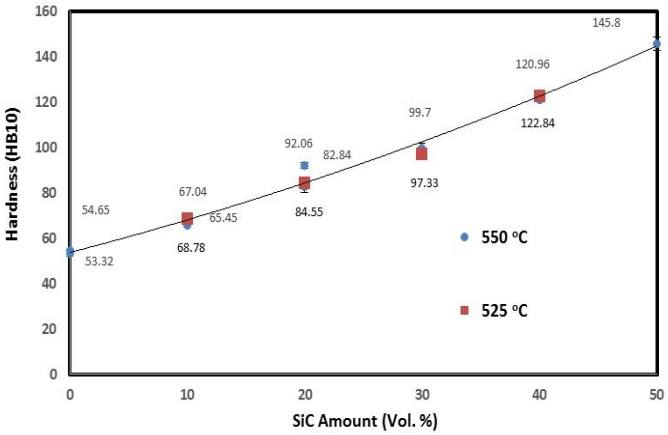


Fig. 2 *Hardness of the unreinforced Al%4Cu matrix alloy and of the composites containing 10, 20, 30 and 40 vol. % SiC(p).*

3.3. Bending Strength of the Composites

Unreinforced Al alloy sample and samples containing various amounts of SiC were subjected to 3 point bending tests. Bending strength of the unreinforced alloy which was sintered at 550 °C was 428 MPa. Addition of SiC particles to the aluminum matrix resulted in an increase in the bending strength up to 20 vol. % SiC content, with the highest strength of about 484 MPa (Fig. 3). Strength values were seen to decrease at higher SiC(p) contents. Bending strength of the composite which contained 50 vol. % SiC was 410 MPa. These results indicate that there is an optimum amount of SiC(p), which may be suggested as 20 vol. % in the present study. The increase in the strength of the composites may be attributed to the hindrance of plastic deformation of the Al alloy matrix, caused by the SiC particles. On the other hand, beyond a certain value of SiC content, strength of the composite decreases due to the decrease in the the amount of matrix phase.

It can be seen in Fig.3 that the samples hot pressed at 525 °C

presented lower bending strength values, as compared to samples which were sintered at 550 °C. This can be attributed to higher amount of porosity in the samples sintered at 525 °C, as revealed by the density measurements. It can be suggested that 550 °C is more suitable for hot pressing of the Al%4Cu-SiC(p) composites.

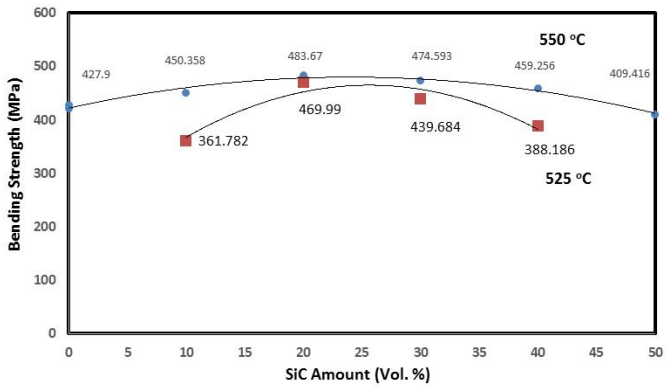


Fig. 3 *Thee point bending strength of the unreinforced Al%4Cu matrix alloy and of the composites containing 10, 20, 30 and 40 vol. % SiC(p), sintered at 525 and 550 °C.*

Bending strain values of the unreinforced sample and composite samples are presented in Fig. 4. Unreinforced sample presented strain values in 21-24 %, whereas addition of SiC resulted in an abrupt decrease in the strain values of the composites. 10 vol. % SiC containing composite had a strain value of 12.2 % and that of 50 vol. % SiC containing composite was 3.3 %. Composites sintered at 525 °C presented lower strain values as compared to composites sintered at 550 °C. This result may be attributed to lower % theoretical density or higher porosity of the composites sintered at 525 °C.

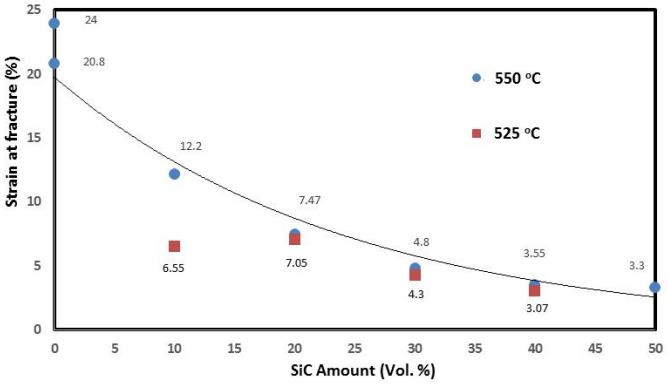


Fig. 4 *Thee point bending strain values of the unreinforced Al%4Cu matrix alloy and of the composites containing 10, 20, 30 and 40 vol. % SiC(p), sintered at 525 and 550 °C.*

In Fig. 5, three point bending stress vs. strain plots of the unreinforced Al%4Cu matrix alloy and of the obtained composites are presented. It can be seen in this figure that the bending strength values of the composites show a slight increase up to 20-30 vol. % SiC and then a decrease with the increase in the addition of SiC. The strain values, on the other hand show a continuous decrease and the strain values diminish down to about 3 %. The composites present a brittle fracture when they contain 40 and 50 vol. % SiC, with no plastic deformation before fracture. However, they present bending strength values as high as the unreinforced sample. The yield strength of the unreinforced Al%4Cu was about 180 MPa and yield strength, which can be determined as the point of departure from linearity of the stress-strain curves, appear to increase with the increase in the SiC content of the composites. In addition, elastic moduli of the composites, which can be stated as the slope of the linear portion of the stress-strain curves, are seen to increase with the SiC content of the composites.

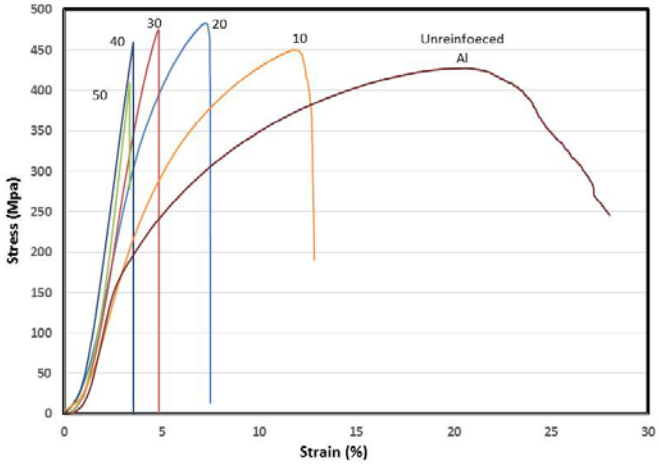


Fig. 5 *Three point bending stress – strain plots of the unreinforced Al%4Cu matrix alloy and of the composites containing 10, 20, 30 and 40 vol. % SiC(p), sintered 550 °C.*

SiC particulate reinforced Al%4Cu matrix composites were obtained by hot pressing. It was shown that the properties of the composites such as strength and hardness can be adjusted by varying the SiC content in the composites.

Acknowledgment

Authors are grateful to the Scientific Research Projects Coordination Unit of Akdeniz University for supporting this study (FAY-2015-304).

References

[1] S. Jayalakshmi, M. Gupta, Metallic Amorphous Alloy Reinforcements in Light Metal Matrices, Springer, 2015, Heidelberg.

[2] A.T. Alpas, J.D. Emburyx, Scripta Metallurgica, Vol. 24 (1990) 931-935.

[3] Y. Sahin, Materials and Design, 24 (2003) 671–679.

[4] S.M.R. Mousavi Abarghouie and S.M. Seyed Reihani, Materials and Design, 31 (2010) 2368–2374.

[5] N. Chawla, C. Andres, J.W. Jones and J.E. Allison, Metallurgical and Materials Transactions, 29A (1998) 2843-2854.

THE USE OF STRUCTURAL ENGINEERING FOR OBTAINING SUPERHARD COATINGS BASED OF NITRIDES TRANSITION METALS

ИСПОЛЬЗОВАНИЕ СТРУКТУРНОЙ ИНЖЕНЕРИИ ДЛЯ ПОЛУЧЕНИЯ СВЕРХТВЕРДЫХ ПОКРЫТИЙ НА ОСНОВЕ НИТРИДОВ ПЕРЕХОДНЫХ МЕТАЛЛОВ

Assoc. Prof. D. Sc. Bochulia T.V., Prof. D. Sc. Sobol O.V.
Kharkiv State University of Food Technology and Trade, 333, Klochkivska Str.,
Kharkiv, 61051, Ukraine
National Technical University «Kharkiv Polytechnic Institute», 21, Kyrpychov Str., Kharkiv, 61002, Ukraine
E-mail: bochulya@i.ua

Abstract: *System analysis of impact negative bias potential on structure, substructure and mechanical characteristics of single-layer ZrN and multilayer ZrN/TiN coatings that been obtained by vacuum arc evaporation done at article with the aim of development of direction «Structural Engineering of Nitride coatings».*

Obtained results have allowed to identify three levels of impact:

- macro- level (phase composition, macrostructure, macrostresses state);

- micro- level (preferred orientation of crystallites – texture);

- nano- level (size of areas of coherent scattering (crystallites), microdeformation).

Superhard state with the magnitude micro-hardness of 44.8 GPa been reached in ZrN/TiN coatings as a result of using Structural Engineering.

KEYWORDS: *NEW MATERIALS, COATINGS, VACUUM ARC, NITRIDES, STRUCTURAL ENGINEERING, MACROSTRUCTURE, MICRODEFORMATION, SUPERHARD COATINGS*

1. Introduction

In recent years is observed heightened interest in new class of materials with unique functional properties – nanostructured materials. For today one of most prospective are nanostructured materials that created in non-equilibrium conditions ion-plasma condensation. The non-equilibrium of conditions of obtaining (typical for these processes) leads to impossibility of accurate modeling of mechanisms of formation and materials properties. Use of structural approach to managing of properties (structural engineering) is proposed in the article to resolve this problem.

In recent years zirconium nitride (ZrN) attracts increased interest due to unique combination of good corrosion resistance, low electrical resistivity, high melting point (about 2990°C), sufficiently high mechanical properties and high chemical stability [1; 2]. Latest makes it demanded as coatings on blade tool that operating at high cutting speed.

Structure and properties of coatings is largely determined by negative potential of bias that supplied to substrate at deposition (U_b) with a high degree of ionization as in the case vacuum arc method of receiving [3].

The aim of article is explore possibilities of using U_b for structural engineering of single- and multi-layer coatings based on ZrN.

2. Material and methods

Vacuum arc with feeding of negative bias potential (in constant or impulse form) onto a substrate (CIB (condensation - ion bombardment) method) has been used as a main method of getting. Basic installation for deposition – modernized «Bulat-6». ZrN coatings were obtained at a pressure of nitrogen atmosphere $P_N = 4.7*10^{-3}$ Torr, the value of the negative DC bias potential of the substrate supplied to the U_b = (-27 ... -300)V. The duration of the deposition process is 1 to 2 hours. Stainless steel plate 12X18H10T 18x18x2 mm sizes and copper foil used as the substrates.

Multilayered two-phase nanostructured coatings TiN/ZrN were precipitated by evaporation of the two types of cathodes: titanium Tues 1-0; low-alloy zirconium; active gas – nitrogen (99,95 %). Procedure of deposition of multilayer coatings is included following operations. Vacuum chamber was evacuated to a pressure of 10^{-5} Torr. Then to swivel apparatus with substrate holder were fed negative potential of 1 kV, were included evaporator and were produced purification of surface of first of the two substrates by bombardment of ions of chromium during 3 ... 5 min. Thereafter substrate holder was rotated 180° and was carried out same purification of second substrate. Further concurrently were included are both evaporators, was fed nitrogen into the chamber and were precipitated first layer from one side ZrN, and from the opposite – TiN.

Process of deposition was performed at the following technological conditions. After deposition of first layer are both evaporators were turned off, were turning substrate holder for 180° and again concurrently have included both evaporators. Arc current during the deposition was 100 A, nitrogen pressure (P_N) in the chamber $4.8*10^{-3}$ Torr, distance from the evaporator to the substrate – 250 mm, substrate temperature (T_s) was in the interval 250 ... 350 °C. Were obtained coatings of thickness about 10 microns. At the time of deposition on a substrate was fed constant negative potential U_b = -70 ... -200V.

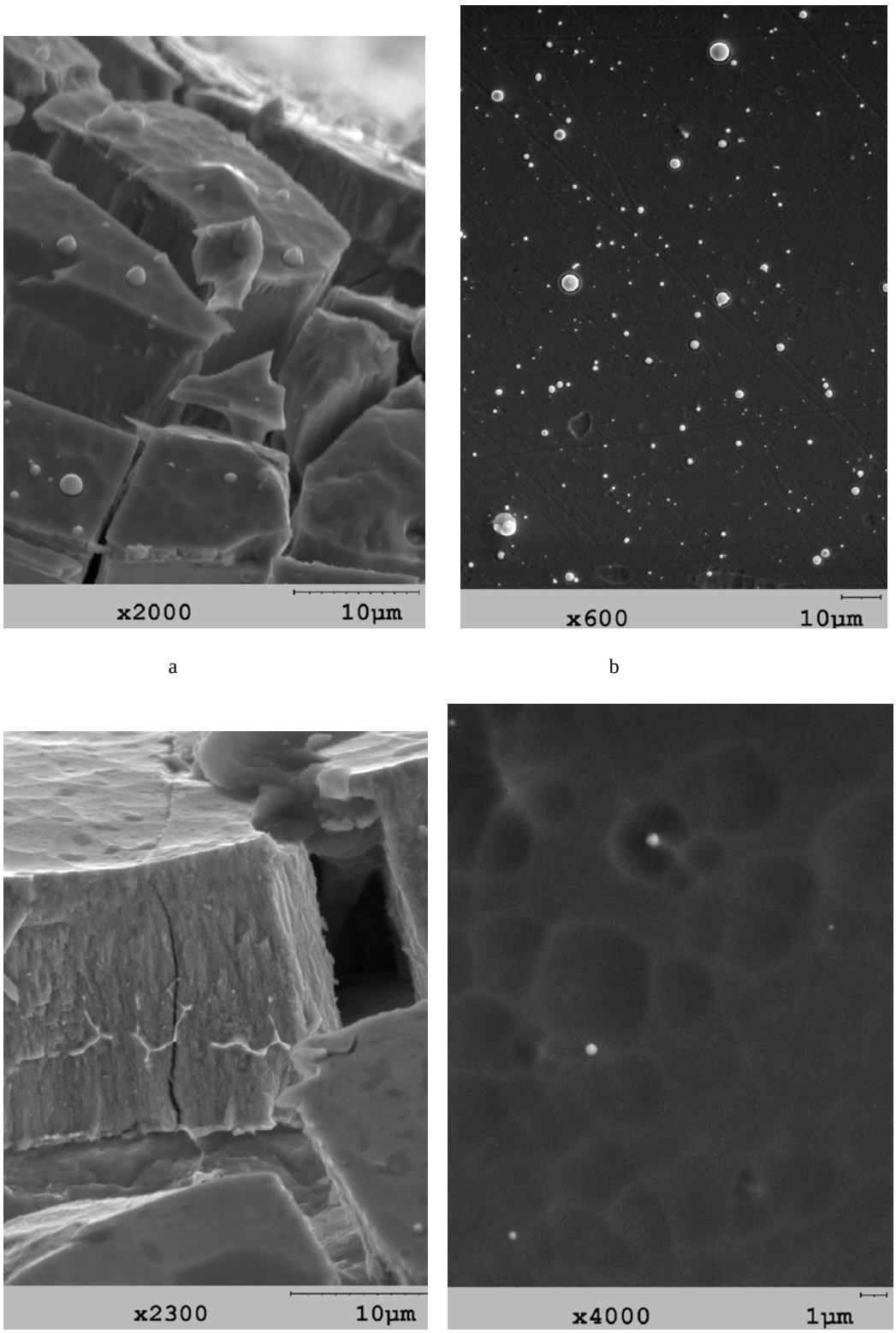
Micrographs of coatings obtained by raster electron microscope JEOL JSM 840. For the electron microscopy studies of the coating deposited on the copper substrate thickness of 0.2 mm.

Phase composition, structure and substructural characteristics have been studied by method X-ray diffractometry (DRONE-4) with use Cu-K_α-radiation. For monochromatisation of registered radiation was used graphite monochromator, which was installed in a secondary beam (ahead of the detector). Study of phase composition, structure (texture, substructure) were produced by means traditional methods of ray diffractometry through the analysis of position, intensities and forms of profiles of the diffraction reflexes. For decryption of diffractograms were used tables of International Centre for Diffraction Data Powder Diffraction File. Substructure characteristics were determined by method approximation.

The hardness of the samples was determined by using installing "Micron-gamma" equipped pyramid Berkovich at room temperature (up to a maximum load of 0.5H).

3. Results and Discussion

Research of morphology coatings surface ZrN been revealed that coatings, which obtained at relatively low constant potential of bias -40 V have as in volume, than also on surface sufficiently large number of droplet phase (Fig. 1a, b). Herewith the structure hasn't pronounced columnar structure of growth of crystallite. Increasing of the bias potential leads to a decrease droplet phase and to appearance of columnar structure. Surface morphology and fracture pattern of coatings that deposited at feed of bias potential with magnitude U_b=-220 V is shown on Fig. 1 c, d. It is seen that microparticles of droplet phase in volume and also on the surface practically absent in coatings and structure of coating growth has columnar appearance (Fig. 1 c). Such considerable decrease in the content of droplet phase can be explained by that droplet component, also as any other accumulation of atoms that placed in plasma acquires a negative (floating) potential and is repelled by surface, on which negative potential (in this case by substrate surface) is served [4].



a b

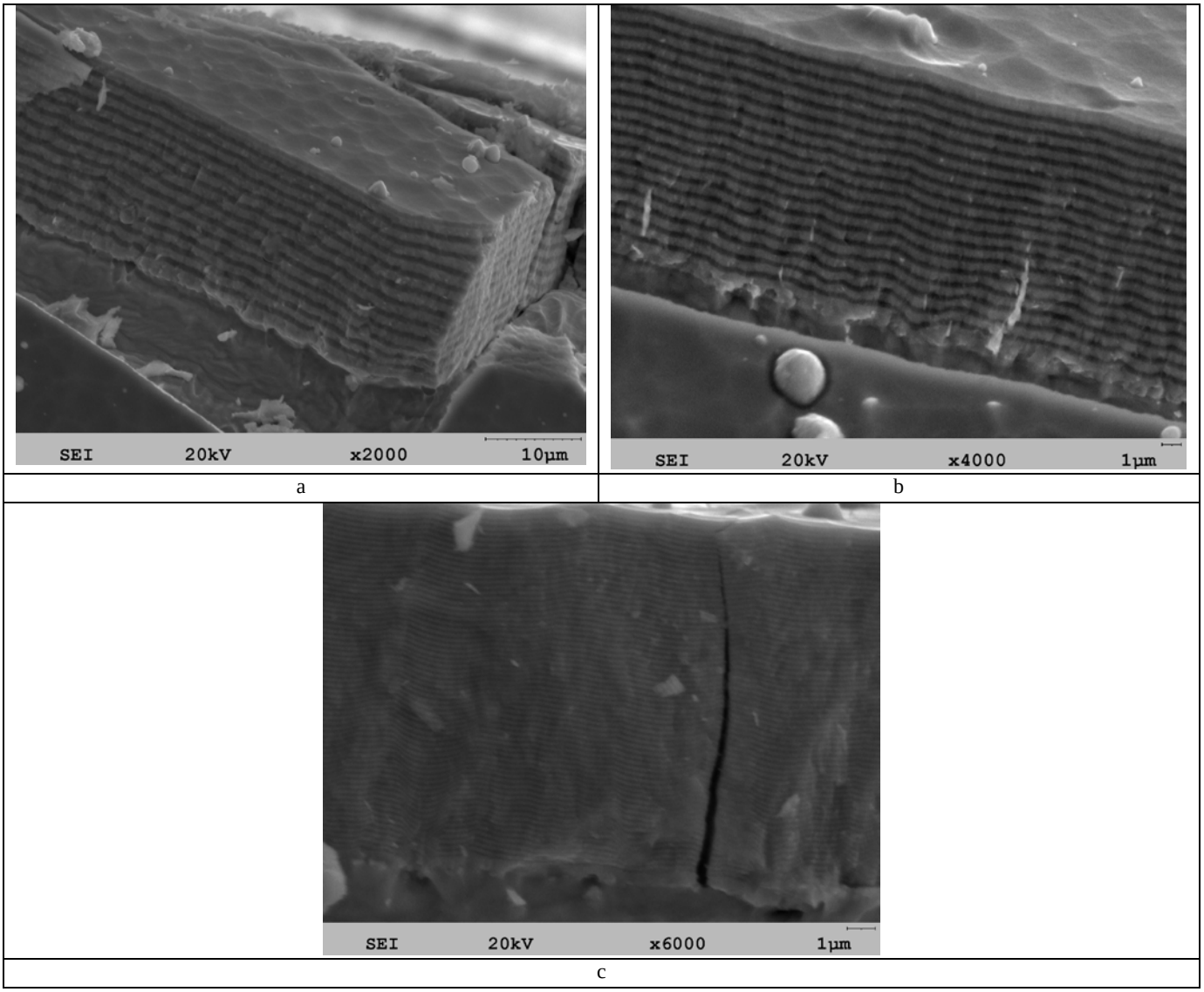
c d

***Fig. 1** – Surface morphology and fraktogramma of fracture coatings ZrN (P_N=4,7 * 10^{-3} Torr): a, b – U_b=-40 V; c, d – U_b=-220 V*

Impact of constant potentials of displacement with magnitude -200 V and -110 V is considered in article for multilayer coatings ZrN/TiN.

Images of fracture morphology of coatings with maximum thickness of layers with bilayer period about 1.5 microns (Fig. 1 a) and with lesser periods of 0.8 microns (Fig. 3 b) and 0.2 microns (Fig. 3 c).

It is seen that planarity and uniformity by thickness of layers is observed and appearance of drop phase inside layers is not observed irrespective of number of layers and magnitude period of multilayer systems at constant potential of displacement -200V.



a b c

Fig. 2 *– Fracture morphology of coatings with 26 layers (13 periods by two layers with average thickness of period 1.5 microns) (a), b – 36 layers (18 periods by two layers with average thickness of period 0.8 microns) and c – 134 layers (67 periods by two layers with average thickness of period 0.2 microns)*

Lighter layers – ZrN, which are obtained by 1.5 times thicker, than TiN. Ie evaporation rate TiN lower than zirconium nitride. At total coating thickness 734 about 17 microns (13 layers of titanium nitride and 13 layers of zirconium nitride) – layer thickness of zirconium nitride - about 900 nm and a titanium nitride – about 600 nm. Despite the fact that time of deposition of each layer were about 300 seconds – deposition rate of zirconium nitride 3 nm/s and the titanium nitride – 2 nm/s. Then obtain at minimum deposition time 10 s – will layer thickness of zirconium nitride about 30 nm and titanium nitride – about 20 nm.

Results of X-ray diffraction research were obtained in basis of structural engineering.

Diffraction spectrums of coatings that obtained at different meanings U_b are shown on Fig. 3. It is seen that forming single-phase structural state that typical for ZrN with face-centered cubic lattice (structural type NaCl) is happening throughout the range of submitted displacement potential (-27…-300 V). In this case attitude of intensities reflections from different planes is changed depending on magnitude of supplied negative potential of displacement that evidence of appearance texture (preferential orientation of crystallites). Large intensity of peak from the plane (200) at low bias potential (27 ... 40 V) indicates on texture with axis [100] that perpendicular to plane of growth.

Changing texture is happening with increasing U_b: at U_b = (-70 ... -150 V) – on bi textured with preferred orientation of crystallites with axes [311] and [111] that perpendicular to plane of growth and at U_b, which exceeding by meaningfully -150 V to almost uniaxial texture with axis [111] (Fig. 3, spectrums 6 and 7).

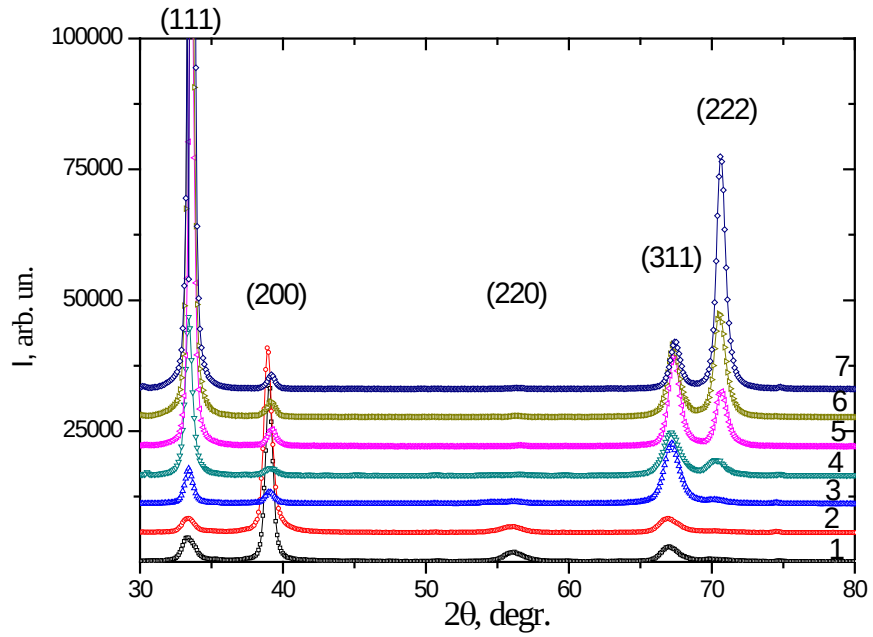


Fig. 3 *– Sectors of X-ray diffraction spectrums of coatings ZrN that were obtained at P=4,7 * 10^{-3} Torr, U_b: 1 – 27 V; 2 – 40 V; 3 – 70 V; 4 – 100 V; 5 – 150 V; 6 – 220 V; 7 – 300 V*

X-ray diffraction (XRD) spectrums of coatings of multiperiod system ZrN/TiN are shown on Fig. 4. Is seen that at smallest Λ = 10 nm (spectrum 1, Fig. 4) phase is formed based on ZrN of crystal lattice with reduced (as compared with tabulated values for ZrN) period of 0.4523 nm. This is determined by smaller atomic radius of titanium, due to which period of isostructural lattice TiN phase is small and amounts to 0.4241 nm (card PDF 38-1420).

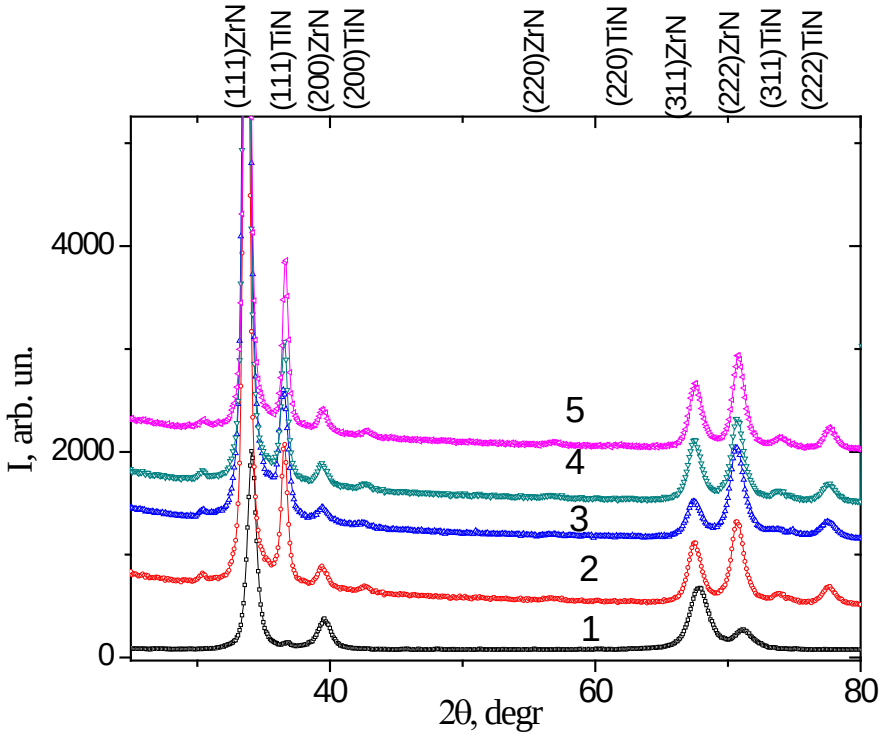


Fig. 4 *– Sectors of diffraction spectrums coatings ZrN/TiN that are obtained at U_n = -110 V, with different Λ: 1 – 10 nm; 2 – 20 nm; 3 – 80 nm; 4 – 150 nm; 5 –300 nm.*

Increasing thickness of Λ for this system leads to forming similar phases ZrN and TiN at crystal lattices with same type of preferential orientation (axis [111]) of crystallites in layers.

Supply of constant potential of displacement on substructural level leads to increasing crystallite size at meanings U_b is less -200 V (Fig. 5). Increasing degree of interaction between metal atoms and nitrogen atoms that were activated by increasing energy are one of main causes of this process. Decreasing crystallite size when submitting higher potential may be associated with process of polygonization under impact high compressive stresses that are reaching magnitude □ = -6,7 GPa (critical magnitude for displacement of dislocations in ZrN). Observed decreasing of microdeformation can associate with this process (Fig. 5 b).

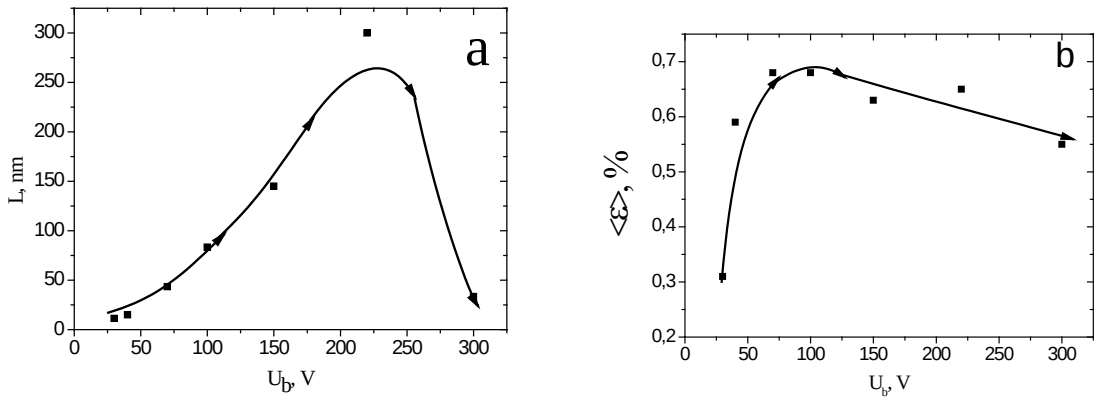


Fig. 5 *– Dependency of crystallite size (a) and microdeformation (b) from constant potential by* $P_N = 4.8*10^{-3}$ *Topp*

Increasing constant potential of displacement in multilayer systems ZrN/TiN on substructural level leads to decrease microdeformation and to decrease crystallite size in TiN component and to increasing sizes in ZrN component (Fig. 6).

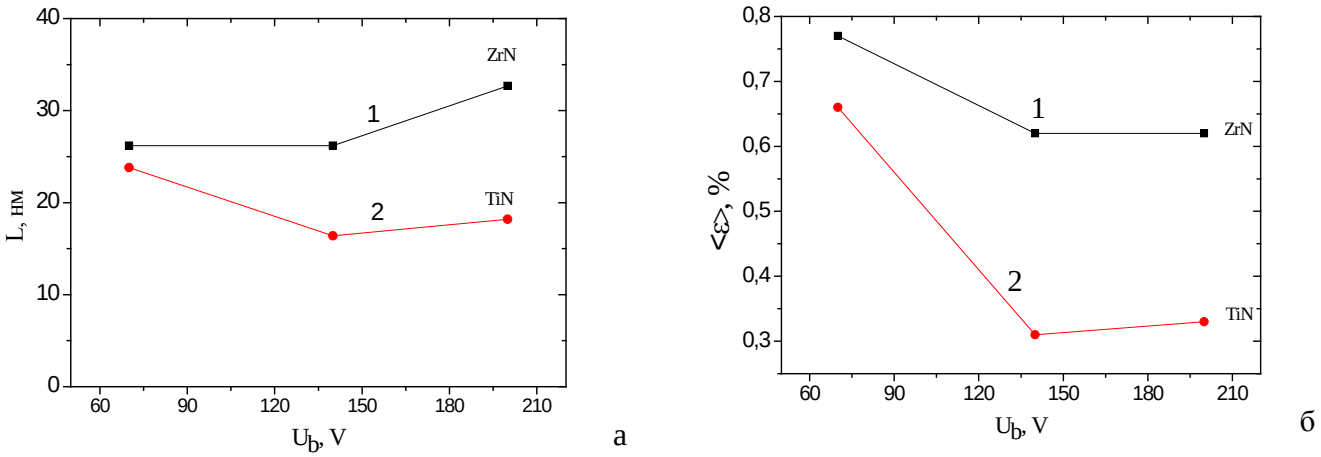


Fig. 6. *Changing substructural (crystallite size, L (a) and microdeformation, <ε> (b)) characteristics on the magnitude supplied bias potential* U_b*. 1 – relates to layers ZrN, a 2 – to layers TiN*

Reason of observed non-uniform changes can be associated with more strong radiation damageability ZrN layers due to large mass Zr atoms that bombarding surface during the growth of these layers. Decreasing microdeformation and increase of medium crystallite size at maximum U_b = -200V can be associated with larger average energy of deposited particles and with temperature of heating the surface. First and second – allows increasing surface diffusion and correspondingly more uniform filling surface plane by atoms. This defines larger average crystallite size. Herewith period grating decreases as a result of compaction coating as ZrN, than also in TiN layers that is shown on Fig. 7.

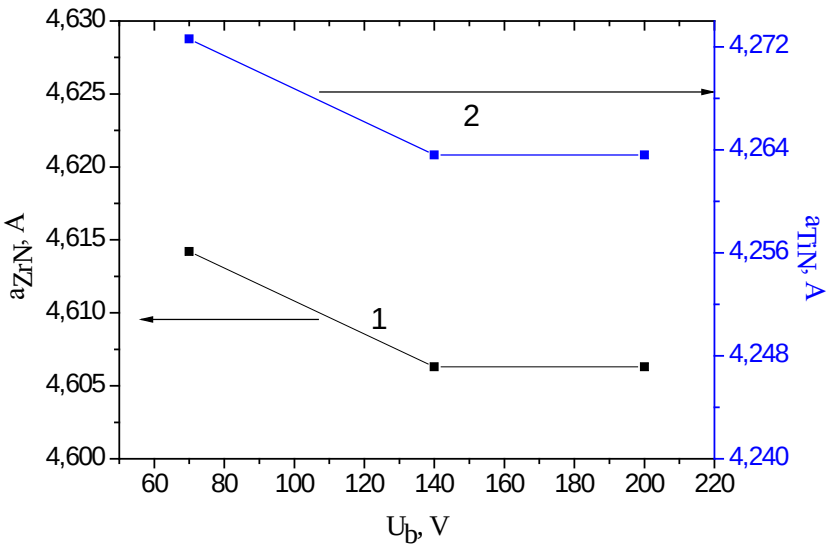


Fig. 7 *– Dependencies of changing periods grating on the magnitude supplied bias potential U_b. 1 – relates to layers ZrN, and 2 – to layers TiN*

Macrostresses state changed by not monotonically: increases with decreasing Λ to 25 nm with subsequent fall at lower period (Fig. 8).

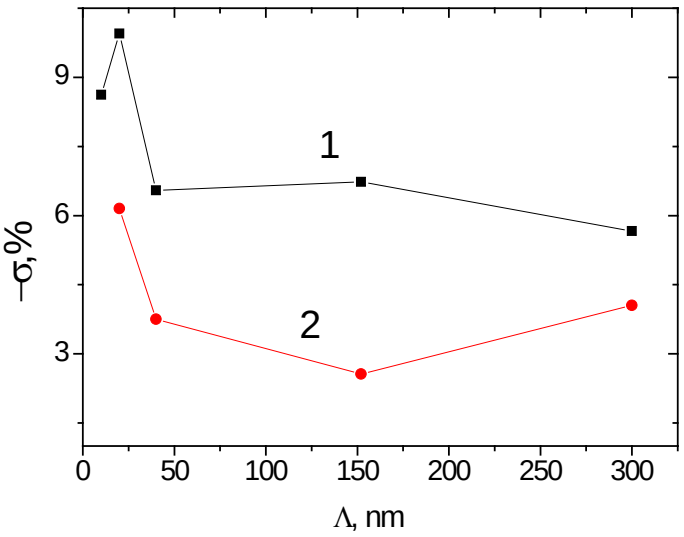


Fig. 8 *– Dependence of magnitude compression stress (-σ) from period of multilayer coatings Λ system ZrN/TiN for components: 1 ZrN, 2 –TiN (U_b = -110 V)*

This reason is because in system ZrN/TiN the depth of maximum penetration of ions Ti→ZrN about 0.8 nm and total depth of impact (where penetrating ions are identified) are ≈2,1 nm. The total depth of impact ions Zr→TiN about 2 nm.

Thus layer with thickness about 2 nm, in which radiation stimulated stirring affects by decisively is formed during deposition of coating on borders. Total depth of impact at period is about 4 nm, because in period Λ are two such boundaries.

Hardness at indentation is most universal express characteristic to determining the mechanical properties. The obtained results are show that largest hardness in single ZrN coatings is 40.5 GPa and achieved at $U_b \approx$ -100 V. Hardness is approximately 33 GPa at a large $U_b \approx$ -200 V. Hardness is lower and its magnitude is determined by Λ for multilayer system ZrN/TiN at $U_b \approx$ -200 V. Hardness decreases from 31 to 25 GPa at decreasing Λ from 50 to 10 nm. Considerably higher hardness of coatings that obtained at a lower $U_b \approx$ -110 V. Hardness reaches 44.8 GPa at Λ≈ 20 nm. But hardness of multilayer coatings ZrN/TiN decreases to 40 GPa also in this case, at reduction of Λ≤ 20 nm.

4. Conclusion

Impact negative potential U_b on surface morphology at deposition affects to decrease of droplet phase. This is determined by the acquisition of drops with negative charge and by repulsion it from negatively charged surface of substrate at deposition.

Supply U_b leads to forming preferential orientation of crystallites at structural level. Supply of small in magnitude U_b (to -50 V) in single-layer ZrN coatings leads to preferred orientation of crystallite growth with axis [100]. Forming texture [311] that passes into texture with axis [111] at U_b = (-150 ... -300 V) is happening at higher U_b = (-50 ... -100 V).

Supply U_b in the interval of (-100 ... -250 V) on substructural level in single layer ZrN coatings leads to decrease average crystallite size and relaxation of microdeformation. Supply U_b in multilayer systems ZrN/TiN leads to decrease microdeformation and decrease of crystallite size in TiN layers and increasing of sizes in ZrN layers.

Highest magnitude of hardness in single layer ZrN coatings is 40.5 GPa and achieved at $U_b \approx$ -100 V. Using higher in magnitude U_b leads to increased density of defects and to decrease of hardness. Changing of hardness has nonmonotonic character depending on U_b in multilayer coatings ZrN/TiN (with $\Lambda \approx$ 50-100 nm). Maximum hardness 44.8 GPa is achieved at lower U_b = -110 V. Decrease of hardness is happening at low Λ as a result of mixing. Herewith ratio H/E (hardness/modulus of elasticity) reaches 0.14 in hardest coatings that complies to high relaxation characteristics of material.

Correlation between increased magnitude of compressive stresses that are developing in coating and increasing hardness is revealed. Compressive stresses are stimulated by higher specific atomic density and contribute to increasing strength of relations and hardness.

5. References

1. Huang J. H., Yang H. C., Guo X. J., Yu G. P., Surf. Coat. Technol. 195(2005) 204
2. Tung H. M., Huang J. H., Tsai D. G., Ai C. F., Yu G. P., Mater. Sci. Eng. A 500 (2009) 104.
3. Azarenkov N.A, Sobol O.V., Beresnev V.M., Pogrebnyak A.D., Litovchenko S.N., Ivanov O.N. Material non-equilibrium state of the modified surface, Sumy: Sumy State University, 2012. -683 p.
4. Khoroshix V.M., Leonov S.A., Belous V.A., Vasilenko R.L., Kolodiy I.V., Kuprin A.C., Tikhon M.A., Tolmachev G.N., Physical Surface Engineering, 12(1), (2014), 45.

RECEIVING ELECTROLYTIC NICKEL-CONTAINING POWDERS OF THE PREDICTED STRUCTURE AT ANODE DISSOLUTION OF SECONDARY HEAT RESISTING ALLOYS

Baikonurov E.G.[1], MS, doctoral candidate of PhD, erden_baikonurov@mail.ru
Chernyshova O.V.[2], Candidate of Technical Sciences, oxcher@mitht.ru
Ussoltseva G.A.[1], Candidate of Technical Sciences, nota-vesna@yandex.kz
Akpanbayev R.S.[1], PhD, rinat2401@mail.ru

1 Kazakh national research technical university named K.I. Satpayev, Kazakhstan, Almaty
2 Moscow technological university, Russia, Moscow

KEYWORDS: NICKEL-CONTAINING POWDER, ANODE DISSOLUTION, ELECTROLYSIS, HEAT RESISTING ALLOY, THE POLARIZING AGENT, A CATHODIC DEPOSIT.

Introduction

The secondary heat resisting nickel alloys containing rare metals and, in particular, rhenium processed by pyro-, hydro-and electrometallurgical ways now. Among the pyrometallurgical the methods connected with oxidation and chlorination, hydrometallurgical – with acid leaching and the subsequent sorption of rare metals are most known, electrometallurgical are based on anode dissolution, electrolysis and electrodialysis. But most often use after all combined methods when for complex processing carry out all above-stated methods. Processing of heat resisting alloys is complicated by the high content of a number of non-ferrous metals and mutual influence of components of alloys on technological processes [1-6]. At the same time in literature problems of receiving powders of non-ferrous metals which is possible when processing such alloys are a little consecrated. Therefore the purpose of the work is to show a possibility of receiving electrolytic nickel-containing powders of the predicted structure at anode dissolution of secondary heat resisting alloys.

Experimental

As an object of researches heat resisting alloy of the following structure has been chosen (masses. %): Re - 4,0; Co - 9,3; W - 8,6; Y - 0,005; La - 0,005; Al - 6,0; Cr - 5,0; Ta - 4,0; Nb - 1,6; Mo - 1,1; With - 0,16; B - 0,15; Ce - 0,025, Ni-60,05. Alloy represents difficult system at which along with non-ferrous metals there are rare and rare-earth elements.

For processing of the specified secondary nickel-containing alloy with receiving powders of non-ferrous metals used a method of anode dissolution with the subsequent sedimentation of nickel and the accompanying metals on the titanic cathode.

Anode dissolution of secondary heat resisting nickel-containing alloy was performed in the galvanostatic mode using acid electrolytes – muriatic, sulfate and nitrate. Preliminary experiments showed that most effectively dissolution proceeds with use of electrolytes with concentration of acids of 100 g/l.

Content of non-ferrous and rare metals as a part of electrolyte was controlled by a photometric method, besides, made the element analysis with use of ICP of a mass spectrometer for the isotope and element analysis of ELAN DRC-e (Perkin Elmer, Canada).

The phase composition of the received powders was carried out with use of the Shimadzu XDR 6000 diffractometer (radiation CuKα, rotation of a sample, continuous (1 hail/min.), step-by-step (a step 0,02 °, an exposition 10s) by the modes in the range of corners 2Θ 5-80 °).

Determination of the sizes of particles by method of measurement of dynamic light scattering is executed on the analyzer of the size of submicronic particles and dzeta-potential of Delsa™ Nano, PN A54412AA.

The polarization phenomena in the course of anode dissolution is studied on the electrochemical technological complex (development of LLC IP Tetran, the Russian Federation) using not compensation way of measurement of potential.

It is known that the polarizing agent promotes formation of a set of the centers of crystallization and by that to increase in dispersion of the received electrolytic powders of metals.

In the real work the polarizing effect of the following organic acids is considered: sulfosalicylic, sulfamic and malic.

Results

At anode dissolution of heat resisting alloy in nitrate electrolyte influence of current on a bathtub which was varied within I = 0,5-2,5A, on compositions of the received electrolyte (within 3 hours) (table 1) and anode slime (table 2) was estimated.

Table 1. Influence of current on composition of nitrate electrolyte at anode dissolution of nickel-containing heat resisting alloy

I, A	Content of metals in electrolyte, g/l					Dissolution rate, g/h*cm^2	Current efficiency for nickel, %
	Ni	Re	Co	Al	Cr		
0,5	10,9	1,06	0,46	0,08	0,05	0,030	58,5
1,0	10,43	1,08	0,35	0,10	0,05	0,045	59,1
1,5	12,1	1,13	0,39	0,18	0,11	0,055	58,9
2,0	15,65	1,37	0,56	0,21	0,18	0,056	49,9
2,5	17,03	1,86	0,61	0,29	0,20	0,055	41,3

Table 2. Chemical composition of anode slimes

I, A	Content of metals, %								
	Al	Cr	Co	Ni	Re	Nb	Mo	Ta	W
0,5	7,63	3,88	6,23	41,09	2,83	3,18	3,89	11,43	19,84
1,0	6,98	3,95	5,23	25,98	1,93	5,58	6,22	15,35	28,78
2,5	5,23	1,88	4,23	27,49	1,83	6,18	7,89	15,43	29,84

The structure of a cathodic deposit was influenced not so much by the electrolysis mode, how many the nature of the used acid electrolyte. Results of researches are shown in table 3.

Table 3. Influence of the nature of electrolyte on structure of cathodic deposites

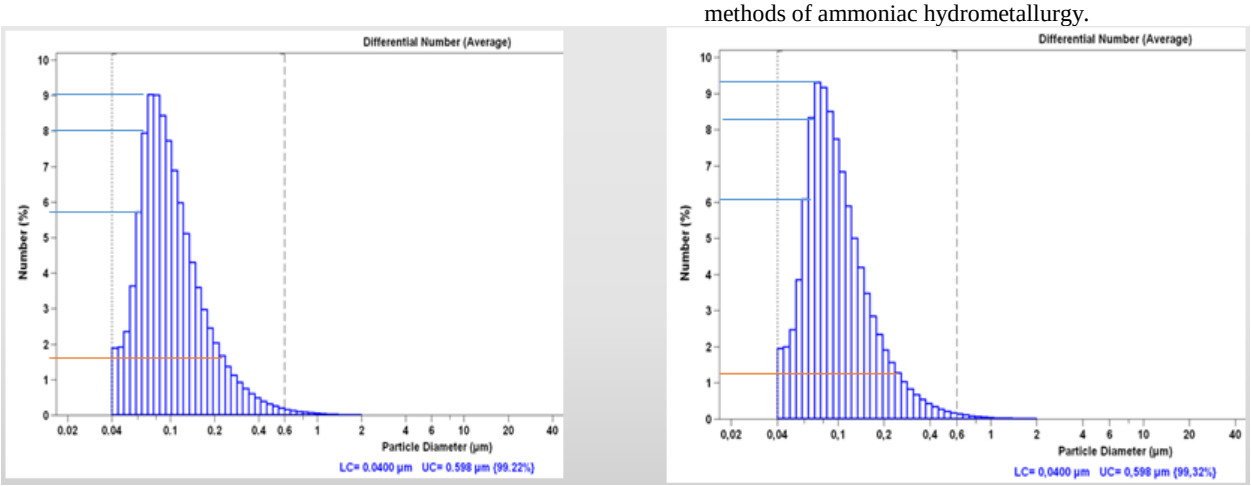
Electrolyte	Duration, h	Content of metals, %			
		Ni	Co	Re	Al
100 g/l H_2SO_4	1	94	5	-	trace
	2	95	4	-	trace
	3	95	4	-	trace
	4	96	3	-	trace
100 g/l HNO_3	1	54	17	16	13
	2	52	18	16	14
	3	54	16	16	14
	4	55	14	15	16
100 g/l HCl	1	68	16	-	16
	2	66	18	-	16
	3	66	18	-	16
	4	64	19	-	17

The data on studying of influence of the polarizing agents obtained during the researches – sulfosalicylic, sulfamic and malic acids have shown that their presence doesn't affect structure of a cathodic deposit, but exerts impact on particle size distribution of the received powder. Results of researches of particle size distribution of the received powders have shown that the greatest impact is exerted by introduction of sulfosalicylic acid thanks to which the share of small fraction (less than 0,1 microns) increased to 99,5-99,7% (the figure 1 – on the example of nitrate electrolyte).

Discussion

Apparently from table 1, the maximum exit of nickel on current is observed at current 1,0 A. The nature of transition of rhenium, cobalt, aluminum and chrome to composition of electrolyte at electrolysis is similar to behavior of nickel.

On the basis of the data presented in table 2 follows that at increase in current at anode dissolution, anode slime is impoverished by nickel, cobalt, chrome and rhenium, but it is considerably enriched with rare metals – niobium, tantalum, molybdenum and tungsten and actually represents their concentrate that can be processe by methods of ammoniac hydrometallurgy.



a *b*

Figure 1. Particle size distribution of the cathodic deposit received at anode dissolution of heat resisting nickel alloy from nitrate electrolyte (a) and nitrate electrolyte with additive of 10 g/l of sulfosalicylic acid (b)

The chemical composition of the received cathodic deposite is established and the link of structure with the used electrolyte is revealed. It is shown (table 3) that depending on the nature of electrolyte and conditions of carrying out electrochemical process – parameters of process and the current program – cathodic deposits of various quality can be received:

a) from sulfate electrolyte – nickel-containing powder with the content of nickel about 95%;

b) from nitrate electrolyte – nickel-containing powder of structures: Ni:Re:Co:Al = 3:1:1:1 and Ni:Re:Co:Al = 10:1:1:1;

c) from muriatic electrolyte – nickel-containing powder of structure Ni:Co:Al = 4:1:1.

On the basis of the results presented in the figure 1 follows that among the organic acids used as the polarizing agents on dispersion of the received powder the greatest impact is exerted by sulfosalicylic acid.

Thus, the possibility of receiving nickel-containing powder of the predicted structure and dispersion at electrochemical processing of secondary heat resisting alloy with use of acid electrolytes is considered. It is shown that the structure and dispersion of the received powder are influenced by the choice of the nature of acid, the mode of anode dissolution and addition to electrolyte of the polarizing agent.

References

[1] Palant A.A., Bryukvin V. A. Electrochemical processing of metal junks of the tungsten and molybdenum in ammoniac electrolytes under the influence of an alternating current // Metals. - 2004, No. 2. – P. 79-82.

[2] Kasikov A. G., Petrova A.M., Bagrova E. G. Extraction of rhenium from shlifotkhod of hot strength alloys using liquid extraction // Nonferrous metallurgy. – 2009, No. 1. – P. 15-19.

[3] Palant A.A., Bryukvin V.A., Levchuk O.M. Complex electrochemical processing of metal junks of rhenium-containing hot nickel alloy in sulfate electrolytes // Electrometallurgy. – 2010, No. 7. – P. 29-33.

[4] Shipachev V. A. Some processing methods of separation and cleaning of rhenium from hot strength alloys // Chemistry for the benefit of sustainable development. – 2012, No. 20. – P. 365-368.

[5] Lyapin S.B., Shtyrlov P.Yu., Haytmitov A.A., etc. Receiving ammonium of rhenium from Fe-Ni-Re alloy waste // the Mine bulletin of Uzbekistan. – 2005, No. 2(21). – P. 105-106.

[6] Dikusara A.I., Ivanenkov I.A., Saushkin B.P., Silkin S.A. and Yushchenko S.P.

High-Speed Anode Dissolution of Heat-Resistant Chrome–Nickel Alloys Containing Tungsten and Rhenium: I. Chloride Solutions // Surface Engineering and Applied Electrochemistry, 2007, Vol. 43, No. 1, pp. 1–10

TRIBOLOGICAL STUDY OF COPPER ALLOY-BASED COMPOSITES REINFORCED WITH WC-W POWDERS PREPARED BY THE SPONTANEOUS INFILTRATION PROCESS OF THE LOOSE POWDER.

DAOUD I[1]. Prof. MIROUD D[1]. Ph. D. YAMANOGLU R[2].
[1] Laboratory of Science and Materials Engineering, University of Sciences and Technology HOUARI BOUMEDIENE, Algeria.
[2] Department of Metallurgical and Materials Engineering, Kocaeli University, Turkey.
daoud_ism@hotmail.com, jamelart@yahoo.fr, ryamanoglu@gmail.com.

Abstract: *Copper alloy-based metal matrix composite (MMCs) reinforced with different combination of WC-W powders were prepared using the spontaneous infiltration process of the loose powders. The density, microstructure, and hardness of the produced composites were characterized. Friction coefficient and wear rate of the samples under different conditions were carried out in order to determine the tribological properties of the copper based composites as a function of different combination of reinforcement mixtures (WC/WC-W). Wear surfaces of the composites were analysed by scanning electron microscopy (SEM). Results show that WC-W powders improve wear resistance of composites significantly. Wear mechanisms were characterized by delamination, micro cracking and abrasive wear.*

Keywords: INFILTRATION, METAL MATRIX COMPOSITES, REINFORCEMENT, WEAR BEHAVIOR, WC-W.

1. Introduction

Metal matrix composites (MMCs) are the combination of different materials in properties with a metal as matrix phase and particulates or fiber as reinforcement phase, the composites can exhibit news properties which each phase does not have. For The required properties and performance from matrix/reinforcement combinations, the objective might be to combine different combination as like as the ductility /stiffness combination, or high thermal conductivity/ low thermal expansion combination. [1-2] However, a great interesting for the MMCs combination of a good ductility and good wear resistance, where there is a widely use of these composites as highly wear-resistant materials. [2-5]

Copper or copper based-alloy composite reinforced with Tungsten or its carbide are one such type of these MMCs. The copper/copper alloy provide the a good ductility and high toughness, while the tungsten carbide used as reinforcement planned to be candidates due to their desirable properties of good wear resistance, high refractory , and excellent mechanical properties, however, their poor toughness limited there utilization into many applications [6]. The demand to produce a new materials with reductions in cost and improvements in performance, for these reasons, effort has been devoted to producing news copper metal matrix composites. In recent years, Several studies concerning the use of Tungsten or Tungsten carbide as reinforcement for copper or copper alloy-based composites for electrical contact applications [7], Thermal management, [8] and wear application [4-5]. Copper or cooper alloy reinforced with WC/W powders are also characterized by the good wettability and the lowest interfacial interaction between matrix / reinforcement led to provide a good compatibility between these combination [9].

The common MMCs fabrication methods including melt stirring, pressureless infiltration, pressure infiltration, and powder metallurgy. [10-12]. the spontaneous infiltration of loose powders is a promising method for manufacturing MMCs. The advantage of this process over conventional method is the process's ability of complex near net shape Components fabrication with lower cost. Spontaneous infiltration processing starts with a ceramic preform of the desired shape, when this preform subjected to elevated temperatures, the molten metal infiltrates spontaneously into the preform, the infiltration continues until the preform fills with molten metal [2-3]. This work presents a tribological study of a copper alloy-based composites reinforced with WC/WC-W powders manufactured by the spontaneous infiltration of loose powders, the effect of W as reinforcement with WC on microstructure and wear resistance of the Cu alloy-based composite was investigated.

2. Experimental

WC (99.7% purity, average particle size of 110 μm), and W powders (99.5% purity, average particle size of 90 μm) were used for the elaboration of Cu-alloy based composites reinforced with a mixture of WC-xW (x=0, 10, 20 and 30 wt.%). Copper-based alloy with the composition of 30 wt.% Mn and 1 wt.% P was used as binder. To obtain homogeneous distribution of the powders a Turbula mixer was used. The mixing time was kept constant as 30 min. After mixing, the loose powders were filled into à graphite mold with an internal diameter of 14 mm. To improve the wettability among powders and molten binder, a BORAX flux (sodium tetraborate decahydrate) was also added on the solid surface of the powders. The infiltration process was carried out in H_2 atmosphere protection at 1050° C with a heating rate of 5 °C/min and 30 min as holding time using a brand of NEW Borel furnace. After the infiltration, the sintered composites were cooled into furnace at 5°C/min to room temperature under H_2 atmosphere. Infiltrated composites were metallographically prepared using silicon carbide paper from 180 to 1200 grit then polished with 9, 3 and 1μm diamond solution.

The microstructural characterization of the MMCs was investigated by a JEOL JSM 6060 scanning electron microscope (SEM), equipped with an Energy Dispersive Spectroscopy (EDS). Vicker's hardness (HV30) of each composites was meseared with indentation loads of 30 kg for 10s (Model FV-700, Future-Tech Corp., Tokyo, Japan), 5 five hardness measurements were performed and the results were given with standard deviations. The densities of composites were measured by the Archimedes method.

Tribological tests were performed using a Nanovea MT/60/NI-type pin-on-disc Tribometer, using an Al_2O_3 ball (6 mm in diameter). The linear speed was set to 0.135 cm/s with a sliding distance of 500 m at room temperature. The normal loads of 20 N and 40 N were applied, respectively. Friction coefficient was continually measured and recorded. Weight loss the samples before and after wear tests using an AND GR200-type microbalance with an accuracy of 10^{-4} g. The following equation was used to obtain the specific wear rate of the composites:

$$W = \frac{M}{\rho.D.L} \quad (1)$$

Where W is the wear rate (mm^3/m.N), M is the weight loss (g), ρ (g/mm^3) is the density of MMC, D (m) and L (N) are and sliding distance and applied load respectively. Worn surfaces characterization of composites after wear test was examined by a scanning electron microscope (SEM) equipped with (EDS).

3. Results and discussion

3.1. Microstructure characterizations

Fig. 1 shows the representative SEM images of the infiltrated composites reinforced with WC-xW powders. It can be clearly seen from the SEM images that all composites have a uniform distribution of the reinforcement powders. The composites showed enhanced densification without any visible porosity indicating that the success of the infiltration process. Fig .1 (E) present a height magnification micrograph of MMC reinforced with WC-30W, it can be seen that there is a good bending at the interface between the reinforced phase and the matrix phase. No change on the initial shape and surface morphology of the reinforced particles was observed, which implies the lowest dissolution of WC and W particles into matrix phase.

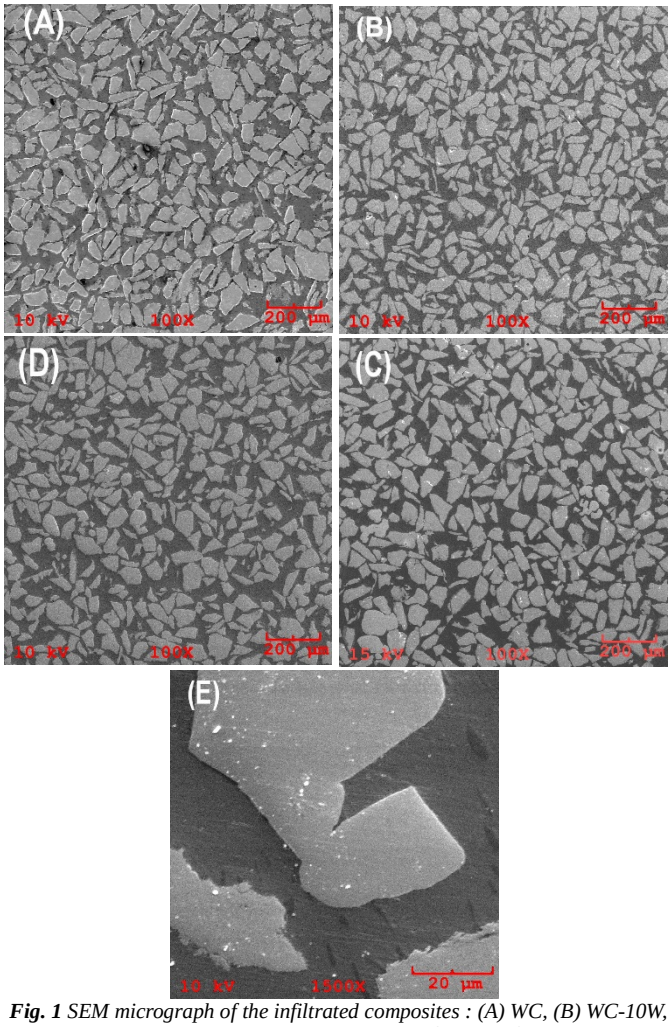


Fig. 1 *SEM micrograph of the infiltrated composites : (A) WC, (B) WC-10W, (C) WC-20W, (D) WC-30W and (E) height magnification of WC-30W.*

3.2. Density and hardness

The density and hardness of the infiltrated composites reinforced with WC/WC-W powders is represented in Fig. 2. It can be seen that the density of the composites increased with increasing W content. The highest values of density was observed for the composite reinforced with of WC-30W, while MMC reinforced with WC particles present the lowest one. At the same infiltrated condition, also, since the wettability behavior of WC and W powders is almost the same, the density change can be explained by the highest W powders density (19.25 g/cm^3), which can significantly influenced the final density of the infiltrated composites.

The hardness of the MMC has been measured using Vicker's method. Compared to the hardness of the binder (copper alloy) with an average hardness value of 154 HV, the hardness of the copper alloy was improved with addition of WC/WC-W reinforcements. Composites reinforced with WC powders present the highest value of hardness compared to other composites with both WC and W powders, with increasing W content, the hardness of MMCs decreased with a highest fluctuation on hardness values as represented by standard deviation. This is probably due to the difference between the hardness of WC (1954 HV) and W (504 HV) powders [13], the higher W content the lowest WC hard particles fraction for the same matrix fraction, therefore, the hardness of the composites decreased.

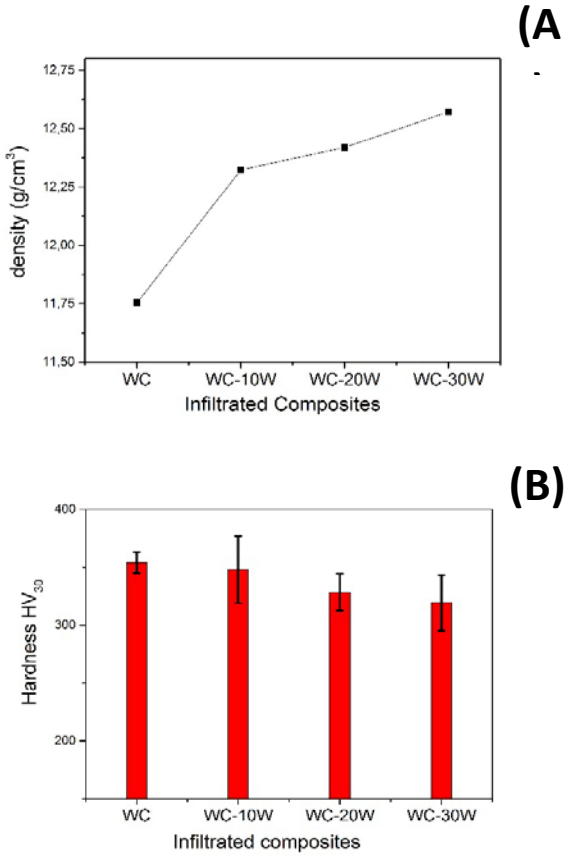
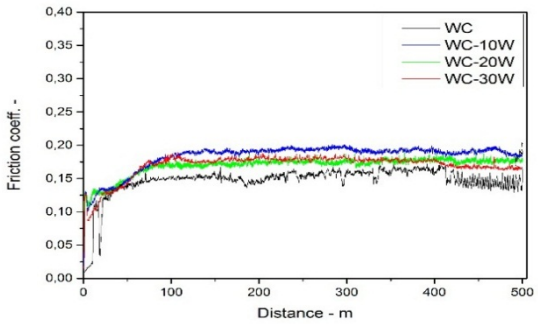


Fig. 2 *Density and hardness of the infiltrated composites reinforced with WC/WC-W powders: (A) density and (B) hardness.*

3.3. Wear behavior

3.3.1. Friction coefficient and wear rate

Fig. 3 shows the friction coefficient curves of composites against Al_2O_3 ball at the normal load of 20 N, after 500 m as sliding distance and sliding speed of 0.135 m/s. All the composites can reaches steady state when sliding distances exceeded ~100 m, during this state the average friction coefficient value was lower for the composites reinforced with WC powders than for the composites reinforced with WC-W. The friction coefficients of composites were in the range of 0.15–0.19. The composite reinforced with WC-10W presented the highest friction coefficient



despite its hardness was not the highest.

Fig. 3 *Friction coefficient of composites reinforced with WC/WC-W powders.*

The wear rate of composites reinforced with WC/WC-W powders at loads of 20 and 40N after a sliding distance of 500m and sliding speed of 0.135 m/s is presented in Fig. 4. The wear rate of composites at loads of 20 and 40N decreased linearly with increasing W content from 0 to 30 wt.%. The wear rate of the WC–30W composite was up to five times lower than that of composite reinforced with just WC powders. All composites present a lower wear rate above $10^{-5}mm^3.N^{-1}.m^{-1}$ and decreased with increase in W wt.% in the reinforcement phase. Fig. 4 shows also that the wear rate of all composites appears to increase with increasing applied loads for the same sliding distance. The reduction in wear rate with increasing the amount of W powders appears to be due to wear debris and plastic deformation of the matrix phase, which help to reduce wear rate. Similar results were reported by Fuzeng Ren et al [14] between Cu-Ag and Cu-W composites, they founded that the wear rate of Cu-Ag is much lower than that of Cu-W due to the plastic deformation during wear. In other hand, the W particle size used in this composite (90µm) compared to WC particle size (110µm) despite the low hardness of W powders (504 HV) influenced the wear rate, decreasing in particles size led to increase the surface area between the reinforcement particles and the matrix phase which can make the particles–matrix interface more strength for the composites reinforced with WC-W particles. However, as describe by Archard's law [15], there is an inverse relationship between the hardness (H) and the wear volume loss, which is in contradiction with the composites presents in this work, the harder composites exhibiting a much higher wear rate. P.K. Deshpande et al had studied the wear behavior of Cu/W and Cu/WC composites. They found that the Cu reinforced with WC particles display a good wear resistance than those of Cu reinforced with W particles, in addition the wear rate of this kind of composites can be influenced by several parameters such as the reinforcements phase ratio and its mechanical properties, the porosity, the reinforcement particle size and the reinforcements-matrix interface bonding strength [7].

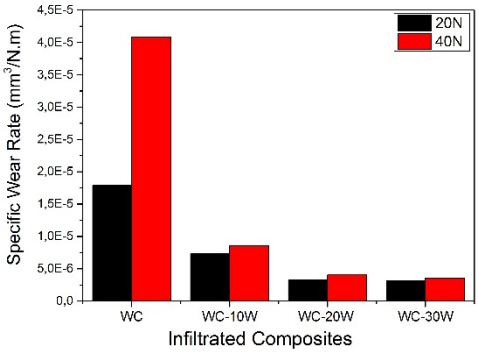
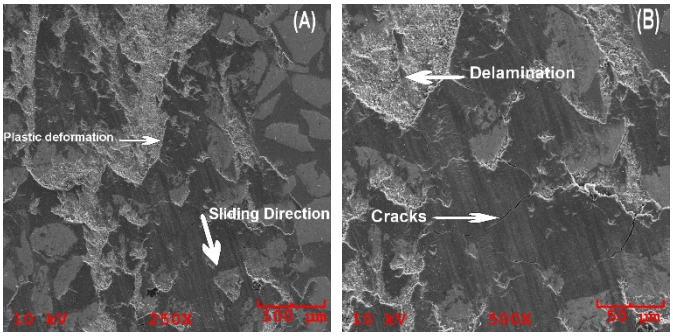


Fig. 4 *wear rate of composites reinforced with WC/WC-W powders.*

3.3.2. Worn surfaces

Fig. 5 shows the worn surface of the composites reinforced with WC-30W at a load of 20 N after a sliding distance of 500m. As revealed from the worn surface, the global mechanism dominant for all the composites was a combination of a plastic deformation of the matrix phase and reinforced particles delamination as shown in Fig. 5. The copper alloy were ploughing between the reinforced particles and can form a thin layer on the sliding direction, also some cracks were observed on matrix surface. On the other hand, reinforced phase were characterized by the delamination mechanism, where, the brittle reinforced particles can cracked, fragmentized, and removed partially or totally from the matrix phase under wear conditions. Generally, wear mechanisms for the metal matrix composites reinforced with ceramic particles can



varied from the abrasive wear, delamination and plastic deformation [4-5, 16-18].

Fig .5 *SEM micrographs of worn surfaces of composites reinforced with WC-W powders at 20N after 500m sliding distance: (a) WC-20W, (b) height magnification of WC-20W.*

4. Conclusion

Copper alloy-based metal matrix composites reinforced with WC/WC-W with different content of W were fabricated using the spontaneous infiltration. The following conclusions can be drawn from this work:

- All the composites present a uniform distribution of the reinforced phase through the matrix phase with a good densification of the final composites.
- The addition of W powders led to an increase in the density of the composites, however, hardness results showed that the

addition of W to WC particle reinforcement reduced the hardness of the infiltrated composites.

- The results of dry sliding tests showed that the addition of W improve the wear resistance of the composites, further the wear rate decrease as the W content increased.
- Composite reinforced with WC-30W showed the bests wear resistance among all the infiltrated composites.
- Wear mechanism varied between abrasive wear, delamination and plastic deformation.

Acknowledgment

The financial and technical supports of the Laboratory of Science and Materials Engineering (LSGM) University of Algeria, The Scientific Research Project Unit of Kocaeli University and the production tools division of (ENSP) company Algeria are greatly acknowledged.

5. References

[1] CLYNE, T. W. An introductory overview of MMC systems, types, and developments. Comprehensive composite materials, 2000, vol. 3, p. 1-26.

[2] NISHIDA, Yoshinori. Introduction. In : Introduction to Metal Matrix Composites. Springer Japan, 2013. p. 1-26.

[3] MIRACLE, D. B. Metal matrix composites–from science to technological significance. Composites science and technology, 2005, vol. 65, no 15, p. 2526-2540.

[4] HONG, Eunji, KAPLIN, Bradley, YOU, Taehoon, et al. Tribological properties of copper alloy-based composites reinforced with tungsten carbide particles. Wear, 2011, vol. 270, no 9, p. 591-597.

[5] DESHPANDE, P. K. et LIN, R. Y. Wear resistance of WC particle reinforced copper matrix composites and the effect of porosity. Materials Science and Engineering: A, 2006, vol. 418, no 1, p. 137-145.

[6] NAWA, Masahiro et NIIHARA, Koichi. Ceramic based nanocomposites. Metal and Ceramic Composites edited by B Cantor, FPE Dunne and IC Stone, published by Institute of Physics Publishing Bristol and Philadelphia, 2004, p. 383-406.

[7] DESHPANDE, P. K., LI, J. H., et LIN, R. Y. Infrared processed Cu composites reinforced with WC particles. Materials Science and Engineering: A, 2006, vol. 429, no 1, p. 58-65.

[8] Miracle DB, Donaldson SL. Introduction to composites. In: ASM handbook. In: Miracle DB, Donaldson SL, editors. Composites, vol. 21. Materials Park: ASM International; 2001. p. 3–17.

[9] KENNEDY, A. R., WOOD, J. D., et WEAGER, B. M. The wetting and spontaneous infiltration of ceramics by molten copper. Journal of materials science, 2000, vol. 35, no 12, p. 2909-2912.

[10] NARULA, Chaitanya Kumar, NAKOUZI-PHILLIPS, Sabine R., et CROSBIE, Gary Mark. Metal-matrix composites. U.S. Patent No 6,051,045, 18 avr. 2000.

[11] ZAMZAM, M. A., ROSS, D., et GROSCH, J. Fabrication of P/M In-Situ Fiber Composite Materials Part 1: Formation of Fibrous Structure. In : Key Engineering Materials. Trans Tech Publications, 1993. p. 235-246.

[12] ASSAR, Abd-Elwahed M. Fabrication of metal matrix composite by infiltration process—part 2: experimental study. Journal of Materials Processing Technology, 1999, vol. 86, no 1, p. 152-158.

[13] TATA, M., MIROUD, D., LEBAILI, S., et al. The Study of Properties of WC-Based and W-Based Composites Fabricated by Infiltration with Liquid Cu-Mn Binder. Asian Journal of Scientific Research, 2009, vol. 2, no 2, p. 76-86.

[14] REN, Fuzeng, ZHU, Weiwei, CHU, Kangjie, et al. Tribological and corrosion behaviors of bulk Cu W nanocomposites fabricated by mechanical alloying and warm pressing. Journal of Alloys and Compounds, 2016, vol. 676, p. 164-172.

[15] ARCHARD, JeFoa. Contact and rubbing of flat surfaces. Journal of applied physics, 1953, vol. 24, no 8, p. 981-988.

[16] ONAT, Adem. Mechanical and dry sliding wear properties of silicon carbide particulate reinforced aluminium–copper alloy matrix composites produced by direct squeeze casting method. Journal of Alloys and Compounds, 2010, vol. 489, no 1, p. 119-124.

[17] SANNINO, A. P. et RACK, H. J. Dry sliding wear of discontinuously reinforced aluminum composites: review and discussion. Wear, 1995, vol. 189, no 1-2, p. 1-19.

[18] ZHANG, Z. F., ZHANG, L. C., et MAI, Y. W. Wear of ceramic particle-reinforced metal-matrix composites. Journal of materials science, 1995, vol. 30, no 8, p. 1967-1971.

WEAR RESISTANT COATINGS ON BASED BORIDE PHASES FORMED IN THE MAGNETIC FIELD ON ALLOYS

ИЗНОСОСТОЙКИЕ ПОКРЫТИЯ НА ОСНОВЕ БОРИДНЫХ ФАЗ СФОРМИРОВАННЫХ В МАГНИТНОМ ПОЛЕ НА СПЛАВАХ

Prof. Dr. Chernega S.[1], Poliakov I.[1], Krasovsky M.[2]
[1]National Technical University of Ukraine "Igor Sikorsky Kiev Polytechnic Institute", Department of metal science and heat treatment,Ukraine, Kiev, st. Polytechnic, Bldg. 9, tel.: +38 (066) 990 - 90 - 35
[2]V. Bakul Institute for Superhard Materialsof the National Academy of Sciences of Ukraine
e-mail: smchernega@mail.ru; polykov_igor@mail.ru

Abstract
In this paper we study the structure, phase composition, microhardness, wear resistance boride coatings obtained on metals and alloys at complex saturation with boron and copper in various physical and chemical conditions, namely carrying satiation without application of an external magnetic field (EMF) and in its simultaneous imposition . Studies have shown that the use of EMF when applying boride coatings allows in 1.5 - 2 times reduce the duration of saturation detail and get coatings with high hardness and wear resistance.
Established that the application EMF on carbon steels formed a continuous, homogeneous boride layer, thickness is 2 times higher than the boriding without EMF. On the diffraction patterns of the surface layers of boride coatings obtained after boriding at application EMF fixed presence phases FeB and Fe_2B, the redistribution of the proportion of boride phases, the change of the crystal lattices and the decrease in the volume of the unit lattice phase FeB. When the complex is saturated steel 45 with boron and copper diffusion layer is composed of the phases FeB, Fe_2B and Cu. Chemical heat treatment with the simultaneous action of EMF leads to the formation of phases in the diffusion zone FeB and Cu, crack resistance layers obtained after saturation with boron and copper increases to 2.23 MPa · $m^{0,5}$ compared to 1.12 MPa · $m^{0,5}$ for boride coatings obtained without action EMF .
Formation diffuse boride layers under the action EMF improves tribological characteristics and leads to an increase in wear resistance of 2.2 – 2.6 times.
KEYWORDS: BORIDING, BORIDE LAYER, MAGNETIC FIELD, COPPER, DIFFUSION, MICROSTRUCTURE, MICRO HARDNESS, WEAR RESISTANCE, CRACK RESISTANCE, STRESS SPALLING

1. Introduction

Analysis of work, aimed at increasing productivity processes chemical and heat treatment, indicates that, along with traditional research in this field is the search in the direction of intensification of diffusion processes [1].

It is known that the resulting diffusion methods boride layers on steel with high hardness and wear resistance in various conditions wear as in couple of friction in dry friction-slip, and at hydroabrasive action. The main disadvantages of forming boride layers is a low growth rate boride needles and predisposition to cracking while increasing layer thickness. High operational characteristics obtained only when a layer of borides sufficiently solid foundation.

Boriding in an external magnetic field (EMF) – one of the new trends in physical materials. The external magnetic field is used to intensify the diffusion saturation working surfaces of metal products chemical elements (boron, carbon, silicon, etc.). At boriding in EMF significantly intensified diffusion processes, which in turn leads to a decrease the time necessary for saturation. Because considerable interest is the study of the effect of external magnetic field on the processes boriding.

The aim of this work was to study the structure and characteristics of complex diffuse boride coatings on iron-carbon steels obtained in powder boriding mixtures with the addition of copper containing compounds Cu_2O or Cu_3P in various physical and chemical conditions, as well as the establishment impact of the saturating powder environment on the characteristics of the coating thickness, micro-hardness, crack resistance, stress spalling, wear resistance.

2. Materials and methods research

Complex boriding powder method performed in a special container under reduced pressure at a temperature of 975 °C for 4 hours using fusible shutters. The research was conducted on samples of carbon steel (steel 20 45, U8).

Saturation alloys boron and copper performed in mixtures containing technical boron carbide B_4C and powders Cu_2O, Cu_3P. As the activator used ftoroplast.

Heating the crucible and the subsequent isothermal holding was carried out in a laboratory oven type HSOL - 1.6,3 / 11. Electric furnace at a temperature of saturation placed in the solenoid, which served as the source of the magnetic field.

After the isothermal exposure container with details removed from the furnace and cooled to room temperature in air, disclose and took out details with clean surfaces that do not require further purification.

This method has the following advantages: simplicity of the process, allows the processing of products of different configurations can be obtained diffusion layers of different thickness.

Polishing was performed on samples of diamond polishing circles paste grit from 28 to 1 micron, that provided to obtain high surface quality research. As a reagent for chemical etching using 3...5% – solution was nitric acid in ethanol; exposure – 30 - 90 sec.

Also, carried out the thermal etching by heating the polished microsection in a box furnace to a temperature of 400 °C and held at this temperature during 30 minutes and cooling on air. Thermal etching, which is known, is based on the chemical activity of the phases depending on their composition, allowing the cells to determine the place of appearance of the phases and their distribution in the structure. It should be noted that the sensitivity of cells to thermal etching phase nucleation is significantly higher than that of ordinary chemical etching. This is due to the advent of color painting phases.

Visual study, measuring the thickness of diffusion layers and microstructure coatings investigate performed on metallographic microscope Axio Observer A1m, Zeiss, in the range the increase 100...1000.

Microhardness measurements were carried out on the instrument PMT – 3 no less than 15 – 20 fields of view at a load of 0.49 – 0.98 N. Measuring accuracy microhardness was – 500 MPa.

The phase composition, quantitative analysis phase, the crystal lattice period, the volume of the elementary gratings phase, region of coherent scattering of boride coatings were analyzed on X-rays diffractometer Ultima-IV, of Rigaku, Japan, in copper $K\alpha_1$, $K\alpha_2$ monochromatic radiation and chemical composition was determined by scanning electron microscope SEM – 106I.

For measurement fracture toughness monocrystals of solid crystalline material used method Evans – Charles. In this case K_{1c} determined by the length of the radial cracks that formed around imprint of Vickers indenter, with semi-empirical relationship:

$$K_{1c}=0{,}015\cdot(E/H)^{1/2}\cdot P/C^{3/2} \quad (1)$$

or graphical dependence between (K_{1c}-F/H) - (H/E-F) and c/a, where F – the constant Marsha; H – Vickers hardness; a – semi diagonal imprint; c – the length of the radial cracks; E – Young's modulus [2 – 4].

Test coatings for wear resistance was carried out on the friction machine M-22M as described in [5] and GOST 26614-85 (the method of determining the tribological properties). The method consists in determining the dependence of the frictional force and wear of the mating surfaces of the sample material and the counterface (45 steel after quenching and low temperature tempering of 180 °C with a hardness 50 HRC) sliding velocity, power and computation load intensity and the coefficient of friction. To test used samples of steel 45 with boride coatings.

3. *Results and discussion*

The mechanism of diffusion boriding powder technical boron carbide is described in [6]. According to this operation, boron carbide at the saturation temperature recovers to the lower boride anhydride boron oxide B_2O_2 by reaction:

$$B_4C + B_2O_3 \rightarrow B_2O_2 + B_mC_n \quad (2)$$

Vapor formed B_2O_2 carried transport of boron to the surface that is saturated. In this way, boron transporter is oxygen. Vapor B_2O_2 disproportionate on the surface that is saturated with formation of atomic boron and B_2O_3 by the reaction:

$$3B_2O_2 \rightarrow 2B + 2B_2O_3 \quad (3)$$

Atomic boron formed diffuses into the material to form the corresponding metal borides.

The surface that is saturated, covered with a film B_2O_3 in the molten state. The role of boron carbide is also that the point of contact with the surface of the particles is saturated, there is a restoration B_2O_3, thanks to the surface is cleaned by melting film. At this formed additional portions of B_2O_2 and is facilitated access to a vapor of B_2O_2 to the metal.

Steels St3 boriding in technical powder of boron carbide (2.13% B_2O_3) powder and boron carbide, boron anhydride purified by the same conditions (T = 1000 °C, and τ = 2 h). The thickness of the boride layer in the first case was 160 – 180 microns. At boriding in powder of boron carbide, of purified from anhydride, it fixed extremely low rate of saturation [7]. The results of this experiment show boride anhydride participate in the formation of active boron atoms.

On the basis of the data obtained, we can conclude that the carrier is B_2O_3 with boron carbide, formed suboxides boron and carbon

$$5B_2O_3 + B_4C \rightarrow 7B_2O_2 + CO \quad [4]$$

Since the temperature boriding high enough, evaporation takes place of boron oxide B_2O_3 and B_2O_3. Condensing on the products, the evaporation of oxides of boron formed melt system B_2O_3 – B_2O_3, containing ions of bivalent and trivalent boron.

A necessary requirement diffusion layer formation is the presence of near surface saturable active atomic boron addition, temperature and duration of exposure should ensure the flow of atomic diffusion of boron in steel.

In the system Fe – B mass transfer elements is carried out mainly by diffusion of boron through the boride layer to the main reaction front, located at interfaces iron – Fe_2B borides and boride Fe_2B – borides FeB [8]. In forming a diffusion layer on the metal surface reaches saturation limit of the solid solution boron (γ) the germ arises first, and then the needle borides tetragonal Fe_2B (*a* = 5,109 Å, *c* = 4,249 Å and *c**a* = 0,832), containing 8,84 % B, a density of 7.336 g\cm^3. These needles grow gradually becoming isolated in continuous layer of borides Fe_2B. Then, on the surface of boride layer having individual needle and then the second layer formed rhombic borides FeB, which has a density of 6.706 g\cm^3 (*a* = 5,506Å, *b* = 4,061Å and *c* = 2,952Å), containing 16.25% B. Application of a magnetic field leads to an intensification of the diffusive penetration of the atoms in the crystalline lattice of γ-Fe.

To establish a relationship between the phase and structure, diffusion layers obtained after saturation with boron and copper, samples were subjected to X-ray analysis. Characteristic areas diffraction pattern shown on Fig. 1 – Fig. 4.

Diffraction patterns taken from the surface of boride coatings on steel 45 after boriding without EMF showed that in the surface layer up to 15 – 20 microns formed phase FeB (Fig.1), and at the complex saturated with boron and copper without action EMF – phase FeB, Fe_2B, Fe and Cu (Fig .2).

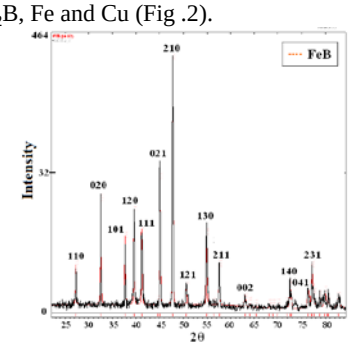


Fig. 1. *Diffraction pattern taken from the surface steel 45 with boride coatings obtained after boriding*

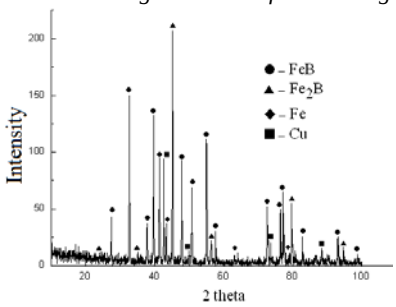


Fig. 2. *Diffraction pattern taken from the surface steel 20 with boride coatings obtained after boriding with adding powder Cu_2O, diffraction peaks of copper lines (111) (200) (220)*

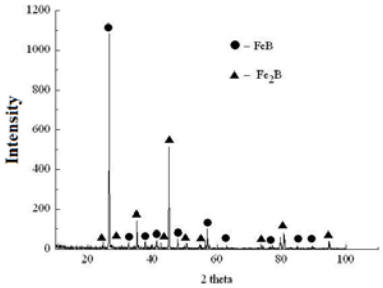


Fig. 3. *Diffraction pattern taken from the surface steel 45 with boride coatings obtained after boriding at using EMF*

In the application of an external magnetic field observed redistribution boride phase. At using EMF in boride layers observed decrease volume phase FeB and on the diffraction patterns surface layers of boride coatings fixed presence phases FeB and Fe_2B (Fig. 3), and after the complex saturation boron and copper under conditions of external magnetic fields fixed phases FeB and Cu (Fig. 4).

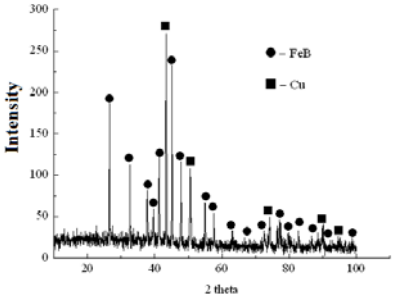


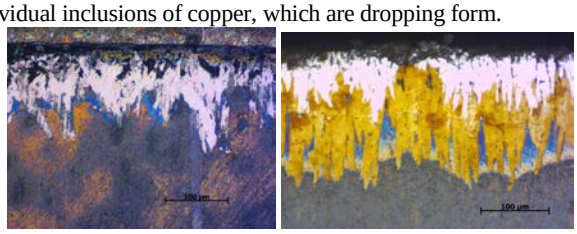
Fig. 4. *Diffraction pattern taken from the surface steel 45 with boride coatings obtained after boriding at using EMF and introduction to the saturating environment copper-containing powder Cu_2O, diffraction peaks of copper lines (111) (200) (220)*

When applying EMF in boride layers observed the redistribution of the proportion of boride phases, changes in the crystal lattice period and a decrease volume of the unit lattice phase FeB (Table. 1). When the complex saturated with boron and copper steel 45 diffusion layer composed of the phases FeB, Fe_2B, Fe and Cu. Chemical heat treatment (CHT) with the simultaneous action of EMF leads to the formation of the diffusion zone phases FeB and Cu. When the complex saturated with boron and copper volume ratio of copper in the surface layer, the results of X-ray diffraction, volume was 4%, and at the CHT with the simultaneous action of EMF quantity of copper component in the surface phase FeB increased to 18.9% (Table. 2). Areas of coherent scattering in phase FeB, obtained by complex saturation with boron and copper with the simultaneous action of EMF, decreased to 38.3 nm as compared to 66.1 nm in the phase FeB, obtained without action EMF.

Table 1. *Parameters crystal lattice phase after boriding and complex saturation with boron and copper in different physical - chemical conditions*

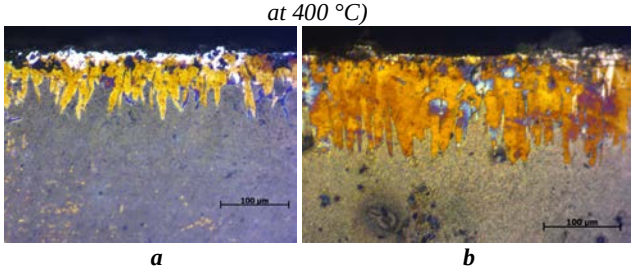
The process of saturation	Name of the phase	Parameters of crystal lattice, Å			Volume (A^3)
		a	b	c	
Boriding without EMF	FeB	4,056248	5,497254	2,944663	65,66
Boriding + EMF	FeB	4,048051	5,497390	2,943259	64,50
	Fe_2B	5,104722	5,104722	4,242536	110,55
Complex saturation with boron and copper without EMF	FeB	4,052739	5,494320	2,942284	65,52
	Fe_2B	5,095910	5,095910	4,247051	110,29
	Fe	2,948823	2,948823	2,948823	25,64
	Cu	3,669155	3,669155	3,669155	49,40
Complex saturation with boron and copper + EMF	FeB	4,054046	5,492628	2,942097	65,51
	Cu	3,606553	3,606553	3,606553	46,91

Metallographic analysis established that obtained the powder technology coating after saturation with boron and copper have a structure with a clear boundary between the coating – base (Fig. 5 and Fig. 6). Diffusion layers are needle of iron borides, which are oriented perpendicularly to the sample surface and are wedged in the ferritic grains. In the near-surface zone boride phase FeB concentrate individual inclusions of copper, which are dropping form.



a ***b***

Fig. 5. *Microstructures complex boride coatings on steel 45 obtained in different physical – chemical conditions: a – boriding, duration saturation – 4 hours, x200; b – boriding + EMF, saturation duration – 2 hours, x200 (color high temperature etching at 400 °C)*



a ***b***

Fig. 6. *Microstructures coatings on steel 45 obtained after complex saturation with boron and copper in different physical – chemical conditions: a – complex saturation with boron and copper without EMF, duration saturation – 4 hours, x200; b – complex saturation with boron and copper + EMF, saturation duration – 2 hours, x200 (color high temperature etching at 400 °C)*

Table 2. *Quantitative phase analysis of boride layers and layers obtained after complex saturation with boron and copper in different physical - chemical conditions*

The process of saturation	Name of the phase	Contents (%)
Boriding without EMF	FeB	100
Boriding + EMF	FeB	15,8
	Fe_2B	84,2
Complex saturation with boron and copper without EMF	FeB	62
	Fe_2B	30,5
	Fe	3,5
	Cu	4
Complex saturation with boron and copper + EMF	FeB	81,1
	Cu	18,9

Obtaining boron coating at simultaneous applying allows in 1.5 – 2 times to reduce the period saturation detail and get coatings with high hardness, wear resistance, crack resistance. At applying the EMF changing morphology boron layers, needles grains decreases sharply, disappear individually disappear sprouted grain borides in the matrix. Needles boron phases closely adjoin to each other and formed a continuous, homogeneous boron layer thickness is in 1.5 times higher than the boriding without EMF.

Investigation of the kinetics of growth of boride layers in a variety of physical - chemical conditions. It was established that after the diffusion saturation in boriding mixture for 4 hours without EMF obtain coating thickness of 125 – 150 microns, whereas when applied EMF formed coating thickness of 160 – 195 microns in 2 hours; at complex saturation with boron and copper at 4 hours without EMF formed coating thickness of 160 – 185 microns, whereas at after saturation with boron and copper the conditions in action EMF at 2 hours diffusion saturation obtained boride phase thickness to 200 – 230 microns.

Conducted research showed that microhardness boride phase after boriding was respectively – phase FeB – 19 – 20 GPa, and phase Fe_2B – 16,5 – 17,5 GPa (Fig. 7). In the complex saturation with boron and copper using EMF get boride layers of microhardness – for phase (Fe, Cu)B – 17 – 18 GPa, and for phase $(Fe, Cu)_2B$ – 15 – 16 GPa. Thus, the complex saturation with boron and copper, observe a decrease of microhardness boride layers and increasing plasticity (Fig. 8).

The calculated data crack resistance and stress spalling, which may occur in the boride phases, depending on physical - chemical conditions on the steel 45 is presented in Table 3.

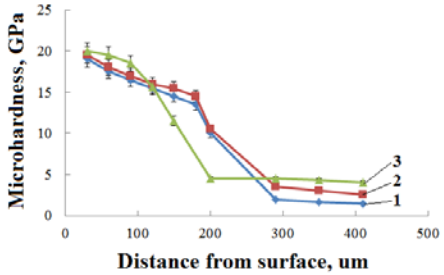


Fig. 7. Microhardness boride phase after boriding at using EMF, on the steels: 1 – steel 20; 2 – steel 45, 3 – U10

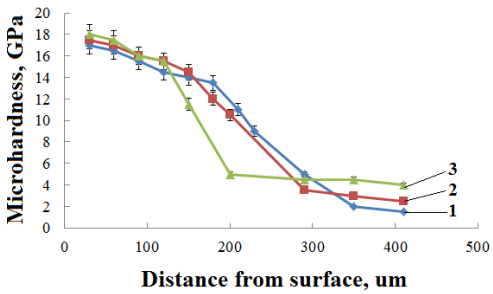


Fig. 8. *Microhardness boride phases obtained after complex saturation with boron and copper at using EMF, on the steels: 1 – steel 20; 2 – steel 45, 3 – U10*

The highest level of of crack resistance is achieved in the boride phases produced in powdered environments with copper powder when applying EMF, and accordingly is 2.23 MPa · $m^{0,5}$, wherein the spalling stress is 420 MPa. Then as at boriding without action EMF crack resistance – 1.12 MPa · $m^{0,5}$ and stress spalling – 160 MPa. Increase the value of spalling stress in layers obtained after complex saturation with boron and copper is caused the formation of higher viscosity phase, for which crack resistance K_{1C} 1.2 – 1.5 times higher than the output phase boride (FeB, Fe_2B).

Table 3. *Crack resistance and spalling stress coating obtained in different physical – chemical conditions (phase Fe_2B)*

Physical-chemical conditions of saturation	**K_{1c}, MPa · $m^{0,5}$**	**$\sigma_{spalling}$, MPa**
Boriding without EMF	1,12	160
After complex saturation with boron and copper without EMF	1,52	225
Boriding at applying EMF	1,79	345
After complex saturation with boron and copper at applying EMF	2,23	420

A study wear resistance of coatings of boride obtained in different physical - chemical conditions (Table 4). As counterbody used steel 45 after hardening and low tempering with hardness 50 HRC. It was established that the diffusion boride coating obtained by application of external magnetic fields have a higher tribological characteristics. Thus, the average linear wear boride coatings obtained in EMF is reduced by 2.4 times, and the friction coefficient is 0.63 compared to 0.66.

Table 4. *Tribotechnical characteristics boride coatings obtained in different physical – chemical conditions: 1 – boriding without EMF; 2 – after complex saturation with boron and copper without EMF; 3 – boriding at applying EMF; 4 – after complex saturation with boron and copper at applying EMF*

Coating	Coef. of friction	Linear wear of the friction pair , I, um,			Mass wear, I (mg/km)		Average linear wear of the friction pair, $I_{average}$, um/km (3 km traversed)	Spot of contact area on the sample, S (cm^2)
		The road friction (km)			sample	counter-body		
		1	2	3				
1	0,66	7	19,5	26	0,94	1,6	8,7	0,26
2	0,65	6,4	14,7	17,7	0,51	1,2	5,9	0,23
3	0,63	6,0	8,4	16,4	0,45	0,95	5,5	0,22
4	0,6	5,2	7,2	10,1	0,25	0,45	3,4	0,18

Complex saturation of carbon steels, boron and copper at using EMF improves the wear resistance of boride layers in 2.2 – 2.6 times compared with 1.4 – 1.5 times without the use of EMF, this is due to the formation of more perfect structure with a smaller quantity pores and higher crack resistance and spalling stress which grow up to 420 MPa as compared with 160 MPa for diffusion boride layers.

4. Conclusion

Application EMF with simultaneous deposition boride coating allows 1.5 – 2 times to decrease the duration of the saturation detail, and obtain a coating of high hardness, wear resistance.

When applying EMF in boride layers observed the redistribution of the proportion of boride phases, changes in the crystal lattice period and a decrease volume of the unit lattice phase FeB and change the morphology of boride layers. Observed a decrease needle-like grains, disappear individually disappear sprouted grain borides in the matrix. Needles boron phases closely adjoin to each other and formed a continuous, homogeneous boron layer thickness is in 1.5 times higher than the boriding without EMF.

Investigation of the kinetics of growth of boride layers in a variety of physical - chemical conditions. It was established that after the diffusion saturation in boriding mixture of carbon steels at simultaneous action EMF coating thickness increases, and the duration of the saturation decreases to 1.5 – 2 times.

Established that ehe highest level of of crack resistance is achieved in the boride phases produced in powdered environments with copper powder when applying EMF, and accordingly is 2.23 MPa · $m^{0,5}$, wherein the spalling stress is 420 MPa. Then as at boriding without action EMF crack resistance – 1.12 MPa · $m^{0,5}$ and stress spalling – 160 MPa. Increase the value of spalling stress in layers obtained after complex saturation with boron and copper is caused the formation of higher viscosity phase, for which crack resistance K_{1C} 1.2 – 1.5 times higher than the output phase boride (FeB, Fe_2B).

Formation diffuse boride layers under the action EMF improves tribological characteristics and leads to an increase in wear resistance of 2.2 – 2.6 times.

REFERENCE

[1] Демченко Л.Д. Влияние предварительной пластической деформации на структуру и свойства азотированных слоев в Fe / Л.Д.Демченко, В.М. Надутов, Ю.С. Черепова//ОТТОМ-4.–К.–2003.–С.205–209.

[2] Evans A. G. Fracture toughness determination by indentation / A. G. Evans, E. A. Charles // J. Amer. Ceram. Soc., 1976. – V. 59. – N 7 – 8. – P. 371 – 372.

[3] Дуб. С.Н. методика испытания на трещиностойкость монокристаллов синтетического алмаза / С.Н. Дуб // В сб.: Производство и применение сверхтвердых материалов. – Киев: ИСМ АН УССР. – 1983. – С. 75 – 78.

[4] Дуб С.М. Определение вязкости алмаза при локальном нагружении / Дуб С.М // Получение, исследование, свойства и применение сверхтвердых материалов. – Киев: ИСМ АН УССР. – 1984.– С. 97 – 100.

[5] Адамовский А.А. Методика исследования триботехнических характеристик сверхтвердых материалов на основе плотных модификаций нитрида бора / А.А. Адамовский // Адгезия расплавов и пайка материалов. – Вып. 42. – 2009. – С. 77 – 84.

[6] Chernega S. Structure and properties of surface layers metals on the basis of high solid boride obtained in conditions of an external magnetic field / S. Chernega, I. Poliakov, M. Krasovskiy. // Machines. Technologies. Materials. – Sofia, Bulgaria. – 2015. – No.12. – P. 52 – 55. – ISSN 1313 – 0226.

[7] Voroshnin L.G. Boronization steel / Voroshnin L.G. Lyahovich L.S. – M.: Metallurgy, 1978. – 240 p.

[8] Диаграммы состояния двойных металлических систем [Справочник]: В 3т.:/ Под общ. ред. Н. П. Лякишева. – М.: Машиностроение. – Т.1. – 1996. – 992 с.